ABSTRACT

Title of Dissertation:	MODELING OF ADVANCED HEAT PUMP CYCLES AND AERODYNAMIC DESIGN OF A SMALL-SCALE CENTRIFUGAL COMPRESSOR FOR ELECTRIC VEHICLES
	Zhenyuan Mei, Doctor of Philosophy, 2023
Dissertation Directed by:	Professor Reinhard Radermacher Department of Mechanical Engineering

Unlike conventional vehicles powered by internal combustion engines, electric vehicles do not have enough waste heat to provide sufficient heating to the cabin. Thus, an additional heating system, such as a heat pump, is needed. However, its performance decreases significantly when the ambient temperature is low. The new kangaroo heat pump cycle (KC) is proposed to increase the heating capacity in low-temperature climates. It is an enhanced flash tank-based vapor injection heat pump cycle (FT-VIC). A sub-cycle is added to the system to increase the refrigerant inlet quality entering the flash tank, which leads to a higher refrigerant mass flow rate and heating capacity. Because KC has a higher heating capacity, the heating needed from the electric heater can be reduced, thus reducing energy consumption and increasing the driving distance. In this study, thermodynamic models were developed for the basic heat pump cycle (BC), FT-VIC, and KC. And a new method evaluating the life cycle climate performance (LCCP) of electric vehicle heat pumps based on the SAE J2766 standard was proposed. Results

show that KC is effective at low ambient temperatures. At -15°C, KC can save 13.8% energy compared to BC, and save 2.7% energy compared to FT-VIC. However, due to the additional weight, KC has a higher LCCP than other cycles. If the pressure ratio limit is removed and the compressor efficiencies are constant, KC can have a lower LCCP than other cycles in cold climates. Transient models were also developed to assess their performance in urban driving conditions. Results show that at the end of the simulation, the cabin room temperature of KC is 3.6°C and 7.0°C higher than that of FT-VIC and BC, respectively. However, due to the high pressure ratio and refrigerant mass flow rate, the accumulated power consumption of KC is 32.4% higher than FT-VIC and 64.4% higher than BC. Despite its high energy consumption, it is more efficient than adding heat from an electric heater. In addition, a small-scale centrifugal compressor was designed for an electric vehicle to reduce the compressor’s size and weight. Results show that its COP is 6.6% higher than that of the scroll compressor at the design point. However, its efficiency at the off-design point quickly drops. Future studies are needed to improve its off-design point performance.

MODELING OF ADVANCED HEAT PUMP CYCLES AND AERODYNAMIC DESIGN OF A SMALL-SCALE CENTRIFUGAL COMPRESSOR FOR ELECTRIC VEHICLES

by

Zhenyuan Mei

Dissertation submitted to the Faculty of the Graduate School of the
University of Maryland, College Park, in partial fulfillment
of the requirements for the degree of
Doctor of Philosophy
2023

Advisory Committee:
Professor Reinhard Radermacher, Chair
Research Professor Yunho Hwang, Co-Chair
Professor Peter B. Sunderland, Dean's Representative
Associate Professor Amir Riaz
Professor Bao Yang
Professor Jelena Srebric

Dedication

To my parents and grandparents.

Acknowledgements

First, I would like to express my heartfelt gratitude to my advisors, Dr. Reinhard Radermacher and Dr. Yunho Hwang, for their unwavering support and insightful guidance. Learning from them helps me shape my research and I would not be able to finish my thesis without their advising. I would also like to thank my thesis committee, Dr. Amir Riaz, Dr. Jelena Srebric, Dr. Peter Sunderland, and Dr. Bao Yang. Their advice helps me polish my work and make it better. In addition, great thanks to Dr. Jiazhen Ling, who opened the door of transient simulation to me.

I sincerely thank Hyundai Motor Company for its financial and technical support. Special thanks to Mr. Jaeyeon Kim and Mr. Hochan An, who taught me many life experiences and knowledge about vehicle thermal management, which could pave the way for my future career.

I am also grateful for the support from Dr. Lei Gao, Dr. Zhenning Li, Dr. Xiaojie Lin, Dr. Tao Cao, Dr. Hanlong Wan, and many other CEEE colleagues. Finally, I would like to thank my parents and grandmother for their understanding and support.

Table of Contents

List of Tables

List of Figures

List of Abbreviations

BC	Basic heat pump cycle
C	Rate of convective heat loss (from skin), *W/m²*
CEEE	Center for Environmental Energy Engineering
COP	Coefficient of Performance, -
C_1	Conversion factor, $kg\ CO_{2\ equiv}$ / *kWh*
C_{CH_4}	Emission factor of CH_4, $kg\ CH_4/kWh$
C_{CO_2}	Emission factor of CO_2, $kg\ CO_2/kWh$
C_{N_2O}	Emission factor of N_2O, $kg\ N_2O/kWh$
$C_{p,dry}$	Specific heat per unit dry air, *kJ/(kg·K)*
C_{res}	Rate of convective heat loss from respiration, W/m^2
cc	Cubic centimeter, cm^3
d	Diameter, *m*
D_{annu}	Annual driving distance, *km*
D_s	Specific diameter, -
E_{diff}	Rate of heat loss from the evaporation of moisture diffused through the skin, W/m^2
E_{res}	Rate of evaporative heat loss from respiration, W/m^2
E_{rsw}	Rate of heat loss from sweat evaporation, W/m^2
eq	equivalent
EV	Electric vehicle
f_{cl}	Clothing area factor, -

FT	Flash tank
FT-VIC	Flash tank-based vapor injection heat pump cycle
GWP	Global warming potential, *kg* $CO_{2\text{-}eq}$
h	Specific enthalpy, *kJ/kg*
H	Height, *m*
HT	Heat transfer
HX	Heat exchanger
h_c	Convective heat transfer coefficient, $W/(m^2 \cdot K)$
h_{fg}	The heat of vaporization, *kJ/kg*
KC	Kangaroo heat pump cycle
LCCP	Life cycle climate performance, *kg* $CO_{2\text{-}eq}$
M	Rate of metabolic heat production, W/m^2
M_r	The total mass of cabin room air, *kg*
$\dot{m}$	Mass flow rate, *kg/s* (*kg/min* for cabin heat exchanger air mass flow rate)
MACs	Mobile Air Conditioning (system)
N	Compressor speed, *RPM*
N_s	Sub-cycle speed, *RPM*
	Specific speed, -
n_{DC}	Total number of the driving cycle, -
I_{cl}	Cloth insulation value, *clo*. 1 *clo*=0.155 $m^2 \cdot K/W$
ICE	Internal combustion engine
IEC	Incremental energy consumption, $kWh/(kg \cdot km)$

P	Pressure, *kPa*
PTC	Positive Temperature Coefficient heater
p_a	Partial vapor pressure, *kPa*
p_s	Saturation vapor pressure, *kPa*
PMV	Predict Mean Vote, -
PPD	percent predicted dissatisfied, -
PR	pressure ratio, -
PR_{tot}	total (overall) pressure ratio = P_{dis}/P_{suc}, -
pct_A	Percentage of auto-controlled, *%*
pct_{tb}	Percentage of each temperature bin, *%*
pct_M	Percentage of manually controlled, *%*
OT	Percentage of the system on-time, *%*
$\dot{Q}$	Capacity, *kW*
$\dot{Q}_{solar}$	Solar radiation, $\int_0^t \dot{Q}_{solar}$ is the accumulated solar radiation and its unit in equation (38) is Wh/m^2
R	Rate of radiation heat loss from the skin, W/m^2
RH	Relative humidity, - (from 0 to 1)
RPM	Revolution Per Minute
SHR	Sensible Heat Ratio
T	Temperature, °*C*
Temp.	Temperature, °*C*
TMY3	Typical Meteorological Year data 3rd edition, from 1991 to 2005

U.S. EIA	The United States Energy Information Administration
V	Velocity, *m/s*
V_{disp}	Compressor displacement volume, m^3
VIC	Vapor injection heat pump cycle
$\dot{W}$	Work, *kW*
x_r	Mass fraction of water vapor mass over total air mass, -
η_{charge}	Battery charging efficiency, *%*
η_{comp}	Compressor efficiency, *%*
η_{isne}	Isentropic efficiency, *%*
η_{tc}	Electricity transmission and distribution efficiency, *%*
η_{vol}	Volumetric efficiency, *%*
ρ_{suc}	Refrigerant suction density, kg/m^3

Subscript

1	main-cycle low-pressure (evaporator) side
2	main-cycle high-pressure (condenser) side
a	air
amb	ambient
app	approach
atmo	the atmospheric reaction product of refrigerant
c (cond)	condenser
cl	cloth outer surface
dis	compressor discharge

DC	driving cycle
e (evap)	evaporator
iHX	indoor heat exchanger
infil	infiltration
lat	latent
m	main cycle
manu&eol	manufacture and end-of-life
mrt	mean radiant temperature
op	operation
oHX	outdoor heat exchanger
plt	passenger latent load
pst	passenger sensible load
s	sub-cycle
	state after isentropic compression
sen	sensible
sub	subcooling
suc	compressor suction
sup	superheating
trans	transportation
ts	total-to-total
tt	total-to-static

1 Introduction

1.1 Background

Over the past decades, the demand for electric vehicles (EVs) has increased dramatically. EV sales recently registered a 40% year-on-year increase [1]. This considerable demand drives the research on EVs. One crucial design factor of EVs is their thermal management. In hot weather, EV cooling can be realized using an air conditioner, which is the same as the conventional vehicle with an internal combustion engine (ICE). However, when heating is needed, the waste heat from the electric motor is usually insufficient to provide target heating capacity [2]. As a result, an additional heating device is needed. The simplest way to fill the gap in heating demand is to use a positive temperature coefficient (PTC) heater, which can provide a large amount of heat at low ambient temperature. However, it also consumes a significant amount of energy due to low efficiency. One example is i-MiEV [3], which uses a PTC heater to provide a heating capacity of up to 5 kW. Its experiment shows that the heating operation reduced the driving distance by up to 45%. A more efficient heating method uses a heat pump, whose efficiency is much higher than a PTC heater. However, the heat pump's performance drops significantly when the ambient temperature is extremely low due to low suction density and low approach temperature [4]. To improve its performance, one can utilize the waste heat from other components to provide supplemental heating [4,5] or uses an alternative refrigerant with better performance [6]. In addition, the vapor injection heat pump cycle (VIC) can also be used to increase the heating capacity [7]. Because additional refrigerant is injected into the compressor chamber, the discharge mass flow rate increases, leading to higher heating capacity. In conclusion, there is a demand for an advanced EV heating system that can provide more heating capacity under extremely cold conditions.

1.2 Literature review

1.2.1 Heating methods for electric vehicles

Zhang et al. [8] summarized the advantages and disadvantages of several air conditioning systems for EVs. A heat pump system is preferred for EVs as it has higher efficiency than electric heaters. And other non-vapor compression solutions are like supplementary methods for future EVs. One significant limitation of the heat pump system is that its performance drops significantly in extremely cold conditions. Qi et al. [9] conducted an experimental study on an air-source heat pump for EVs. They first experimented with the fresh air mode and found its heating capacity at maximum compressor speed and T_{amb} = -20°C is roughly 25% lower than that at maximum compressor speed and T_{amb} = -10°C, which is caused by low refrigerant mass flow rate at low suction temperature. They also experimented with various return air modes, where the air inlet temperature of the indoor heat exchanger changes to mimic the return air. The result shows that the return mode has little to no effect on the refrigerant mass flow rate and heating capacity.

Several methods can be applied to increase heating capacity. One is to utilize the waste heat from other components. Li et al. [4] experimentally compared an R134a secondary loop system with a direct expansion system. Because the waste heat increases the coolant loop temperature, the evaporating temperature of the secondary loop system is higher than that of the direct expansion system, which leads to a higher refrigerant mass flow rate and heating capacity. The high coolant temperature also helps prevent frost formation on the radiator.

Ahn et al. [5] tested an R134a dual heat sources heat pump for an EV. The dual heat sources heat pump was operated in three modes: air-source only, waste heat only, and dual sources. When the heat pump is in the air-source only mode, the heating capacity drops quickly as the ambient temperature reduces. It could only provide 36% of the target heating capacity when the ambient temperature was at -10°C. The system performed well in the waste heat only mode when the ambient temperature was low. However, its performance was dominated by the amount of waste heat available. And on the dual sources mode, since it could absorb heat from two heat sources, the system had a higher heating capacity than the other modes when the ambient temperature was moderate. If the ambient temperature was low, the heat from the air was negligible, and the waste heat only mode was preferred.

Another method to increase heating capacity under low ambient temperature is to use economized vapor injection heat pump cycle (VIC), which increases the compressor discharge mass flow rate by injecting part of the condensed refrigerant back into the compressor at an intermediate pressure. In general, there are two types of VIC: flash tank (FT) based and intermediate heat exchanger (IHX) based. Wang et al. [10] compared two types of VIC through experiments and modeling, and found that FT-VIC performs better than IHX-VIC. IHX-VIC can also be classified as an upstream type or a downstream type. In upstream IHX-VIC, refrigerant flow splits first and then goes through IHX, while in downstream IHX-VIC, the refrigerant flow goes through IHX first and then splits. Because the downstream type system has more subcooling than the upstream type system, its performance is better than the upstream design [7]. Qin et al. [11] tested two vapor injection compressors with different injection port designs in an R134a upstream IHX-VIC. The result shows that VIC can increase heating capacity by up to 27% compared to BC. And single-porthole vapor injection compressor performs better than a three-porthole vapor injection compressor when the ambient temperature is above -10°C. Okuma et al. [12] tested and simulated a novel FT-VIC, where a thermoelectric model was added before the flash tank to increase the vapor quality entering the flash tank. The experimental results show that the proposed system on average increased heating capacity by 19.8% and decreased COP by 8.6% at -17.8°C. And increasing the size of the condenser can help improve its COP due to reduced condensing pressure.

Another method to improve heat pump heating capacity is to use an alternate refrigerant with better performance. Ghodbane [13] evaluated the performance of R152a and hydrocarbon refrigerants as alternatives to R134a in MACs. Results show that in direct expansion MACs, R152a in road condition and idle condition can improve the Coefficient of Performance (COP) by 11% and 15%, respectively. And R290 can improve COP by 4% in road conditions. Liu et al. [6] tested an R290 heat pump and showed that its heating capacity at -10°C is 55% higher than that of the R134a or R1234yf heat pump. However, R290 is flammable, which limits its application.

In a nutshell, the performance of the heat pump system drops dramatically when the ambient temperature is low. Many attempts have been made to increase heating capacity and efficiency in low ambient conditions. Those attempts include recovering waste heat, using economized vapor injection heat pump cycle, and using an alternative refrigerant with better heat transfer performance. And there is a need for more heating capacity at extremely low temperatures with good efficiency.

1.2.2 Mobile air conditioner LCCP evaluation

Life Cycle Climate Performance (LCCP) is CO_2 equivalent emission from the cradle to the grave, which is widely used in the HVAC industry to evaluate the global warming effect of the system. Much LCCP calculation has been done on typical residential air conditioners and heat pumps [14,15]. LCCP consists of two parts: direct emission and indirect emission. The direct emission is linked to the atmospheric reaction product of refrigerant and the refrigerant leakage & leftover caused by the assembly, operation, and scrap. In contrast, indirect emission includes the CO_2 emission caused by manufacturing, operation, service, and end-of-life treatment. For MACs, carrying MACs with the vehicle causes additional CO_2 emission, which also needs to be included in the indirect emission.

Many researchers have done LCCP calculations for MACs. SAE published standard J2766 [16] to guide the LCCP calculation for MACs. Together with the standard, Pappasavva et al. [17,18] developed an excel tool named Green-MAC-LCCP to evaluate the LCCP of conventional ICE vehicles. The temperature bin method is used to group the weather data based on the standard. Before calculating the annual energy consumption, MACs should be tested or simulated following the SAE standard J2765 [19]. The results can then be used to generate a regression model. The power consumption of MACs was then evaluated second by second under a driving cycle that combines FTP75 and HWFET [20]. And manually controlled MACs' on-time in every temperature bin is calculated by the cabin thermal comfort model. Their calculation of global CO_2 equivalent emission by region shows that Asia has the highest emission, followed by Western Europe and North America. And their parametric study results show that using an internal heat exchanger (IHX) reduces the CO_2 equivalent emission by 7%. Also, increasing compressor efficiency by 10% can reduce emissions by up to 5%. One limitation of the Green-MAC-LCCP tool is that it was developed for cooling mode only. And its conversion factor was developed for conventional fossil fuels. Rhoads and Hill [21] later developed an LCCP calculation tool based on the Green-MAC-LCCP tool. The new tool added support for electric compressors and water-based systems.

Zhang et al. [22] used the Green-MAC-LCCP tool to evaluate the annual energy consumption of MAC for EVs in several Chinese cities. The MAC was tested experimentally following a modified SAE standard J2765 [19] simulation matrix. In their experiment, the volume flow rate was varied according to the vehicle speed to account for the effect of air leakage at different vehicle speeds instead of fixing the indoor heat exchanger inlet air mass flow rate. And their experiment involved two operating modes: outdoor fresh air mode and recirculation mode. The results show that as compared to using fresh outdoor air, using recirculation air can save energy consumption from 7 to 48%. It should be noted that in their study, only the cooling mode was evaluated, and LCCP was not calculated.

Yang et al. [2] evaluated the LCCP of the fuel cell, electric, and ICE vehicle. Since their calculation calculated the LCCP of the entire vehicle, the heat pump model was greatly simplified. During the analysis, the cooling and heating capacities and COP were fixed for all three types of vehicles. And the tank-to-compressor efficiencies were also set during the calculation. Three driving modes were analyzed, which covered driving in urban areas, highways, and hybrid conditions. And the system's on-time is a quarter of the total driving time. The results show that the overall EV has the highest energy consumption and greenhouse gas emission, mainly because of the high energy consumption while manufacturing the battery. Also, due to the low efficiency of the combination of heat pump and PTC heater, the EV does not have satisfactory results when the system on-time increases.

Although many LCCP calculations have been done for MACs in conventional vehicles, little effort has been put into the LCCP calculation for EVs with a heat pump. The existing analyses either only considered cooling mode or used a significantly simplified heat pump model. Therefore, there is a need for an LCCP evaluation method for EVs with a heat pump.

1.2.3 Small-scale centrifugal compressor for air conditioner or heat pump application

The small-scale centrifugal compressor has been developed for applications requiring low-volume flow rates, such as portable coolers, mobile gas turbines, or fuel cells. Some existing small-scale centrifugal compressor works with a similar approach used by Arpagaus et al. [23] are summarized in Table 1. In the operating condition column, “A” stands for air, “B” stands for brine, and “W” stands for water. Due to the small impeller diameter, their rotational speed was up to 270,000 RPM. The details of those compressors are introduced below. Casey et al. [24] from PCA Engineers Ltd studied the scaling of the centrifugal compressor. To obtain high efficiency for a specific head rise, the pressure coefficient of the compressor should be in the 0.45 – 0.55 range, which requires constant tip speed. And since the flow coefficient of the compressor for a given volume flow is proportional to the inverse of the square of the impeller diameter, the impeller diameter should be small to acquire higher efficiency. And the high tip speed can only be obtained when the speed of revolution increases, in which case the shaft and bearing design can be challenging.

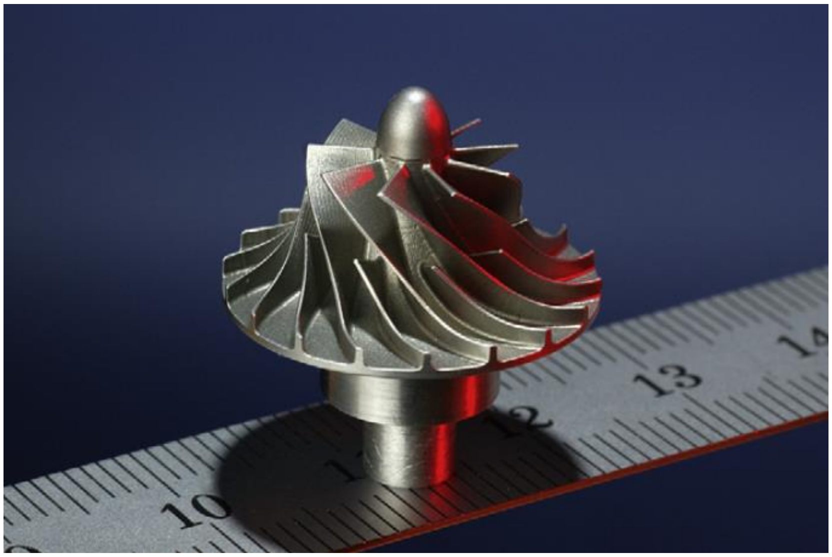

Figure 1: Impeller of a 1.8 kW centrifugal compressor [25]

Brondum et al. [26] designed an ultra-high-speed centrifugal compressor for an 88 kW capacity rooftop unit. The designed ambient temperature was 35°C. The suction and discharge temperatures were 7°C and 54°C, respectively. The target pressure ratio was 4. The ultra-high-speed centrifugal compressor was a two-stage compression device with an economizer installed between two stages. The impeller blade was a backswept blade, which increased the impeller throat area and reduced loading in the exducer. And the diffuser is a pipe diffuser. Since the bearing load was small, an oil-free refrigerant-lubricated ball bearing was selected. And the motor was cooled by the superheated refrigerant at low pressure. According to the author, an ultra-high-speed centrifugal compressor could increase efficiency by 15-20%, reduce compressor weight by 30-50%, and lower part counts by 30-50%. And the peak stage efficiency for the designed efficiency was 84%.

Mechanical Solution Inc. and Lennox International Inc. developed a small-scale centrifugal compressor for a 17.6 kW air conditioning system using a low GWP refrigerant. The details of the compressor have not been published yet.

Schiffmann et al. [25,27,28,34] designed a small-scale centrifugal compressor for a two-stage domestic heat pump system. This air-water heat pump system has two throttling processes, and an economizer was intended to be installed between two compressors.

Only the first-stage compressor was produced. The 20 mm diameter impeller was equipped with a backswept blade. To improve the performance of the compressor, a splitter blade was added between each pair of full blades. Schiffmann compared different bearing technologies and found that aerodynamic bearing has the most desirable merits. It is an oil-free solution and has a long lifetime. The designed compressor was tested in a compressor test rig. The results show that the maximum rotational speed is 210,000 RPM, and the peak efficiency is

79%. To improve the compressor performance under the different operating conditions, optimization of the impeller blade shape was performed by using multi-objective optimization methods.

Table 1: Summary of small-scale centrifugal Compressors

Group	Application	Pressure Ratio	Speed (krpm)	Bearing Type	Operating Condition	COP	Diffuser
		Efficiency (%)	Diameter (mm)	Refrigerant	Capacity (kW)		
Schiffmann et al.[25,27–29]	Two-stage heat pump	1.5-3.3	150-210	Gas bearing	A-12/W60	2.5-5	Vaneless
		79	20	R134a	7-16		
Carré et al.[30]	Two-stage heat pump	2.3-2.7	180	Gas bearing	A7/W35	2.7	Vaneless
		82-88	20/20	R134a	10		
Javed et al.[31]	Two-stage heat pump	1.5-3.5	160-270	Gas bearing	B5/W30/W55	4.3	Vaneless
		77	15/15	R134a	6.5		
Gasser et al.[23]	Single-stage heat pump	2.5	142-200	Ball bearing	B9/W28	9.7	-
		-	21	R600	4-20		
Van Gerner et al.[32]	Three-stage heat pump	4.7	180-195	Ball bearing	W45/W100	2.3	-
		68	21/23/23	R601	7.5		
Casey et al. [24]	Single-stage heat pump	2.5	250	-	-	-	Vaneless
		65	21	R600	-		
Laveau et al. [33]	A mesoscale refrigerator	1.31	100	-	-	-	Vaned
		-	20	R134a	0.35		
Brondum et al. [26]	Two-stage air conditioner	4.5	-	Ball bearing	A35/-	-	Pipe
		84	-	R134a	96.85		

The optimized geometry has a 2% increase in terms of yearly efficiency.

Based on Schiffmann's works, Carré et al. [30] developed a twin-stage centrifugal compressor for a similar cycle. The impeller diameter remains the same, and this compressor uses an aerodynamic bearing. Three auxiliary refrigerant circuits were used: one for aerodynamic bearing, one for magnetic motor cooling, and one for bypass. The bypass circuit is mandatory for the centrifugal compressor system to avoid surge flows during the compressor starting or stopping process.

Javed et al. [31] from the same group developed a design procedure for the small-scale centrifugal compressor used in a two-stage heat pump with two heat sources. The process starts with the heat pump model, and the design point data from the heat pump model is used to make a preliminary design in the 1D compressor model. This model can then generate a more detailed compressor map for the heat pump model to verify the design point and run the simulation for off-design operating conditions. According to the 1D compressor model, the designed centrifugal compressor reaches 77% isentropic efficiency at the design point. The 3D impeller model was built in ANSYS for blade passage design and optimization. Optimization was performed by reducing blade curvature and tip-leakage flow. After optimization, the compressor ratio was increased from 2.13 to 2.48, and the isentropic efficiency was increased from 76% to 79.5%.

In conclusion, many small-scale centrifugal compressors have been developed. Their small weight makes them attractive to be used in MACs. Yet there is little research on applying small-scale centrifugal compressors in MACs.

1.3 Research objectives

The objective of this study is as follows:

- Thermodynamic analysis and LCCP evaluation of advanced heat pump cycles for EV:

    - Build thermodynamic models of BC/FT-VIC/KC for quick cycle performance analysis.
    - Calculate and compare their performance under various conditions.
    - Calculate and compare their LCCP across the U.S.
- Transient modeling of advanced heat pump cycles for EV:
    - Build detailed transient models of BC/FT-VIC/KC, to have a more realistic comparison between cycles.
    - Compare the performance of BC/FT-VIC/KC under various driving conditions while considering the impact of frost formation.
- Centrifugal compressor design and performance evaluation for future MACs with high cooling demand:
    - Design and evaluate a centrifugal compressor for future MACs with high cooling demand.

2 Heat pump cycles

This chapter explains the three heat pump cycles involved in chapters 3 and 4, emphasizing the heating performance in cold climates. Chapter 5 describes a centrifugal compressor for EV with different cycles involving battery thermal management. More details are provided in chapter 5 and are not discussed in this chapter to avoid confusion.

2.1 Base heat pump cycle (BC)

Figure 2 shows the basic heat pump cycle (BC) schematic, which consists of four major components: compressor, condenser, expansion device, and evaporator. Because it is the most straightforward cycle, it serves as the baseline in this study. Supplement components include a receiver, an accumulator, two four-way valves, and two check valves. The receiver stores liquid refrigerant and manages refrigerant charge in the system. An accumulator is used to prevent the compressor from liquid or two-phase suction. And two four-way valves are added to the cycle to switch between cooling and heating modes. The four-way valve installed right after the compressor discharge point directs refrigerant to the indoor heat exchanger (iHX) or outdoor heat exchanger (oHX). In contrast, the second four-way valve guarantees that refrigerant always flows into the receiver from its inlet. In addition, two expansion valves (EXV) are used in BC, one for cooling mode and the other for heating mode. When the EXV is closed, the refrigerant can bypass it through the check valve. Its P-h diagram can be found in Figure 5 (a).

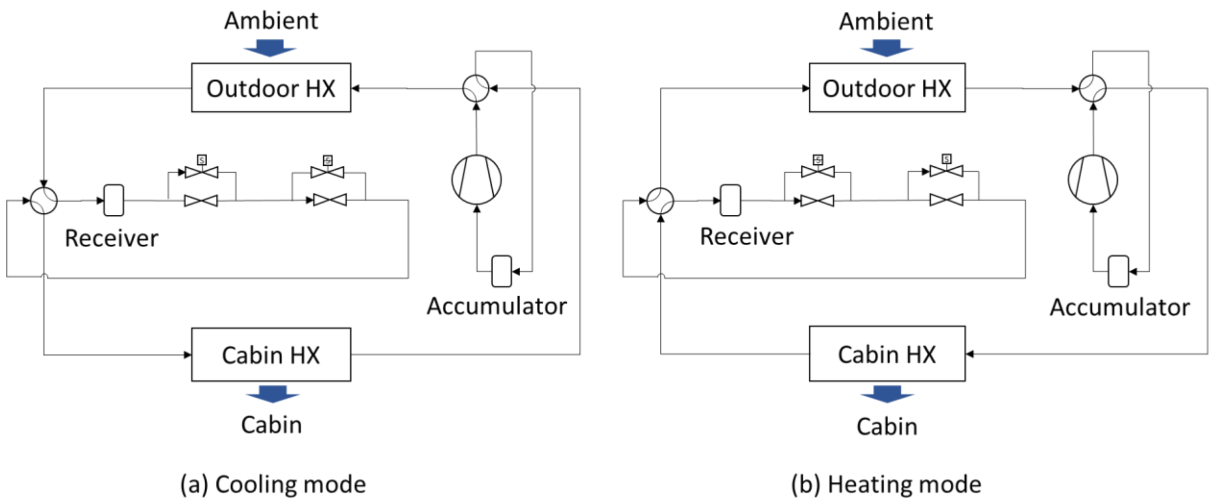

Figure 2: Schematic of the basic heat pump cycle (BC)

2.2 Flash tank-based vapor injection heat pump cycle (FT-VIC)

Vapor injection heat pump cycle (VIC) is a two-stage cycle that injects refrigerant vapor into the compressor chamber at an intermedia pressure. This brings two benefits: first, because additional refrigerant is injected into the compressor chamber, its discharge mass flow rate increases. Second, the mixing process at the injection point reduces the suction enthalpy of the second compression stage, which lowers the compressor discharge temperature. Generally, there are two types of VICs: flash tank-based vapor injection heat pump cycle (FT-VIC) and intermediate heat exchanger-based vapor injection heat pump cycle (IHX-VIC). In this study, FT-VIC is considered as it has better potential than the other cycle. Its P-h diagram can be found in Figure 5 (b).

For VIC, its injection pressure plays an important role. To better illustrate the relationship between injection pressure and the compressor's suction and discharge pressure, one can use the below equation:

$$P_{inj} = k\sqrt{P_{suc}P_{dis}} \quad (1)$$

Where k is the factor of injection pressure [35] or relative intermediate pressure [36]. For ideal VIC with isentropic compression, the best COP is obtained when the injection pressure is the geometric mean of suction and discharge pressure [37]. However, the compressor's isentropic efficiency in the actual system is smaller than one and varies with different operating conditions. Therefore, the optimum factor of injection pressure varies according to the operating mode and system design. Xu et al. [35] experimented with an R1234yf heat pump system and found that optimum COP was obtained when k was between 1.15 and 1.35 under low ambient temperature (-10°C-0°C). Ma and Li [36] suggested the optimum range of k between 1.1 and 1.3 for an R22 heat pump VIC with an economizer.

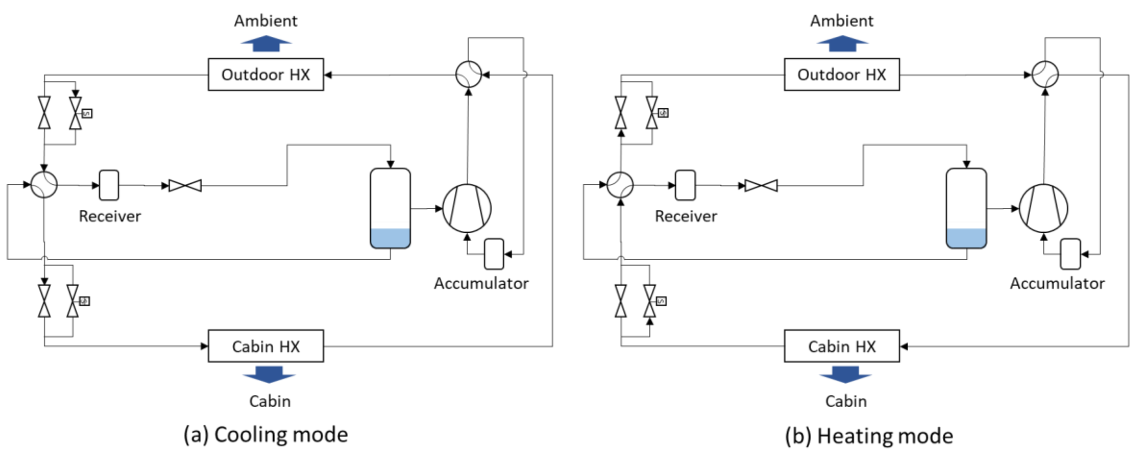

Figure 3: Schematic of the flash tank-based vapor injection heat pump cycle (FT-VIC)

2.3 Kangaroo heat pump cycle (KC)

The kangaroo heat pump cycle (KC) [38] is an improved FT-VIC. Its schematics are shown in Figure 4. And its P-h diagram can be found in Figure 5 (c). The main cycle is an FT-VIC, and a sub-cycle is introduced to improve heating and cooling capacity. The sub-cycle condenser is installed between the first expansion device and the flash tank, which increases the vapor quality of the refrigerant entering the flash tank, thus increasing the injection mass flow rate. As a result, the heating capacity can be increased. Also, the evaporator of the sub-cycle is installed between the flash tank liquid outlet and the second expansion valve, which lowers the evaporator inlet quality and potentially increases the cooling capacity. Because of the introduction of the sub-cycle compressor, the COP of KC may be lower than FT-VIC in most cases. However, it can provide more heating or cooling capacity, which is helpful in extreme conditions.

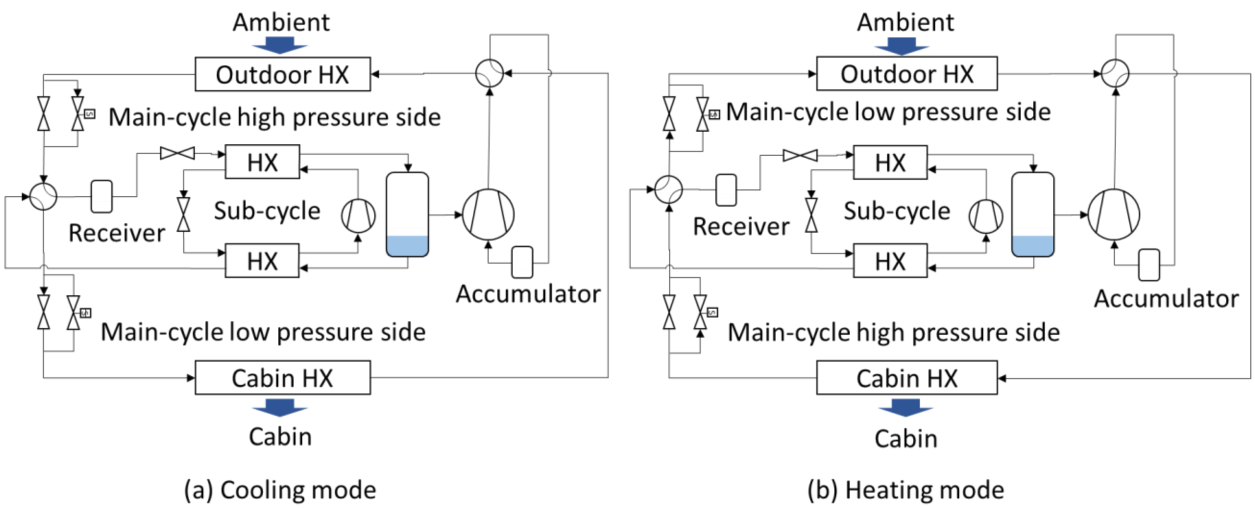

Figure 4: Schematic of kangaroo heat pump cycle (KC)

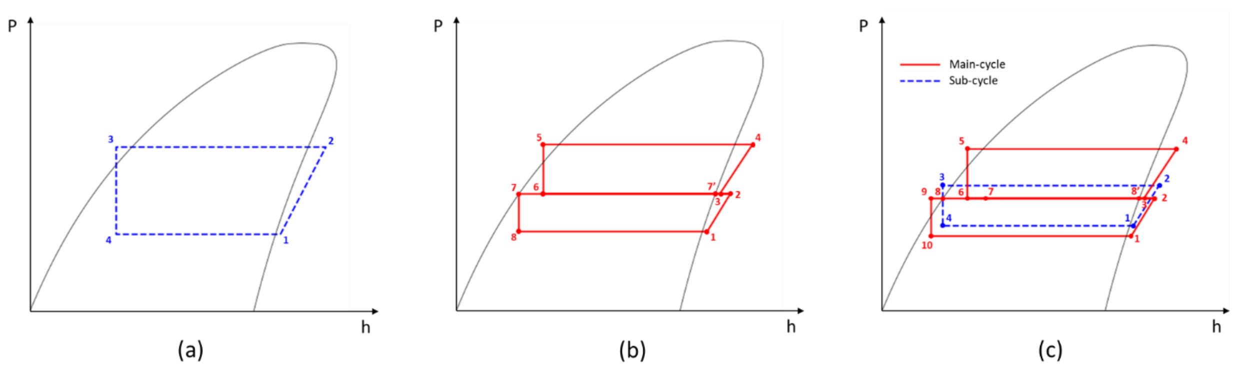

Figure 5: P-h diagram for three cycles: (a) BC, (b) FT-VIC, (c) KC

3 Thermodynamic model and LCCP evaluation

Three thermodynamic models were developed for fast-cycle performance evaluation. Only major components were modeled. Auxiliary components such as the receiver, accumulator, closed valve, and bypass valve were not included in the thermodynamic model.

To simplify the calculation, heat exchangers were modeled by using approach temperature, which is the difference between the air outlet temperature and the refrigerant saturation temperature.

$$T_e = T_{e,air,out} - T_{app,e} \tag{2}$$

$$T_c = T_{c,air,out} + T_{app,c} \tag{3}$$

Once the saturation temperature is known, the corresponding condensing and evaporating pressure can be calculated. Then the refrigerant-side capacity can be solved by using the equations below:

$$\dot{Q}_c = \dot{m}(h_{c,in} - h_{c,out}) \tag{4}$$

$$\dot{Q}_e = \dot{m}(h_{e,out} - h_{e,in}) \tag{5}$$

Where inlet and outlet enthalpies are determined by the cycle model.

As for the air-side model, there is only a sensible load in the heating mode. Therefore, a sensible load equation can solve the air outlet temperature.

$$\dot{Q}_c = \dot{m}_{air,dry} C_{p,dry} (T_{c,air,out} - T_{c,air,in}) \tag{6}$$

It is necessary to have a dehumidification model to obtain the air outlet temperature in the cooling mode. A detailed dehumidification model requires fin information to solve sensible heat ratio (SHR), which is not available in this simplified model. Therefore, a simplified method is used in this study, where it is assumed that air outlet relative humidity is 100% when there is a latent load. The model first calculates an air outlet temperature using the sensible load equation to determine whether there is a latent load. And latent load calculation will be involved if it is lower than the dew point temperature of the inlet state. The latent and sensible loads are then solved using the equations below through iteration.

$$\dot{Q}_{e,lat} = \dot{m}_{condensate} h_{fg} \tag{7}$$

$$\dot{m}_{condensate} = \dot{m}_{dry\ air}(\omega_{in} - \omega_{out}) \tag{8}$$

$$\dot{Q}_{e,sen} = \dot{m}_{dry\ air} C_{p,dry}(T_{e,air,out} - T_{e,air,in}) \tag{9}$$

This air-side model is compared with the results from CoilDesigner [39]. In this comparison, a random heat exchanger model is used. The output heat load serves as the input to the air-side model. And the comparison of SHR is shown in Figure 6. As you can see, the maximum deviation is less than 3%.

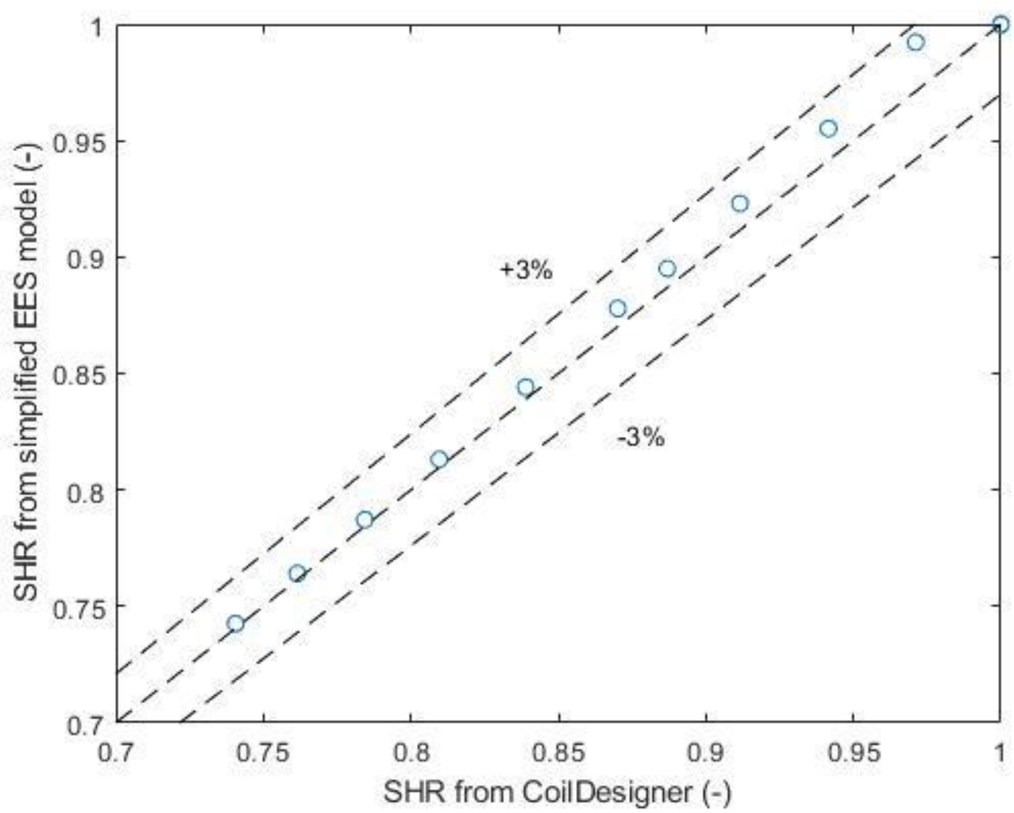

Figure 6: Air-side model validation

The below equations can solve the COPs for cooling and heating:

$$\mathrm{COP}_{\mathrm{cooling}} = \dot{Q}_e/\dot{W}_{\mathrm{input}} \tag{10}$$

$$\mathrm{COP}_{heating} = \dot{Q}_c/\dot{W}_{\mathrm{input}} \tag{11}$$

$$COP_{heating,overall} = (\dot{Q}_c + \dot{Q}_{PTC})/(\dot{W}_{\mathrm{input}} + \dot{W}_{PTC}) = (\dot{Q}_c + \dot{Q}_{PTC})/(\dot{W}_{\mathrm{input}} + \dot{Q}_{PTC}) \tag{12}$$

The model assumptions used are:

- No heat loss in pipes.
- Isentropic expansion process.
- No refrigerant pressure drops.
- No air pressure drops.
- Constant air specific heat capacity and density.
- The HX outlet relative humidity is 100% when there is a latent load.
- Vapor injection pressure is the same as the discharge pressure of the lower-stage compression.
- Perfect phase separation in the flash tank.
- Constant approach temperatures.

These models were developed in Engineering Equation Solver (EES) [40]. Details of cycle models are explained below. Because EES uses declarative programming, it does not require control flow. As a result, the actual solving process may not be the same as that shown in the flow chart.

3.1 Efficiency-based compressor model

In this study, single-stage compressors are used in BC and the sub-cycle of KC. Its governing equations are shown below by using three compressor efficiencies.

$$\dot{m} = \rho_{suc} V_{disp} \frac{N}{60} \eta_{vol} \tag{13}$$

$$\eta_{isen} = \frac{h_{dis,s} - h_{suc}}{h_{dis} - h_{suc}} \tag{14}$$

$$\dot{W}_{\text{input}} = \frac{h_{dis} - h_{suc}}{\eta_{comp}} \tag{15}$$

Where ρ_{suc} is suction density, V_{disp} is displacement volume, η_{vol} is volumetric efficiency, $h_{dis,ideal}$ is ideal discharge enthalpy when there is no increase in entropy, h_{suc} is suction enthalpy, h_{dis} is actual discharge enthalpy, η_{isen} is isentropic efficiency, η_{comp} is compressor efficiency (includes motor and mechanical losses), and $\dot{W}_{\text{input}}$ is the compressor power input.

In this study, all efficiencies are modeled as a second-order polynomial equation.

$$\eta = b_1 + b_2 PR + b_3 RPM + b_4 PR \times RPM + b_5 PR^2 + b_6 RPM^2 \tag{16}$$

Where PR is the pressure ratio.

The validation results of the BC compressor are shown in Figure 7 and Figure 8. For compressor power, its deviation is less than 6%. And for refrigerant mass flow rate, when compressor speed is equal to or lower than 8,600 RPM, the maximum deviation is less than 5%. For higher compressor speeds, the maximum deviation is up to 10%. Therefore, this study capped the maximum compressor speed at 8,600 RPM. And the minimum compressor speed was set at 3,000 RPM.

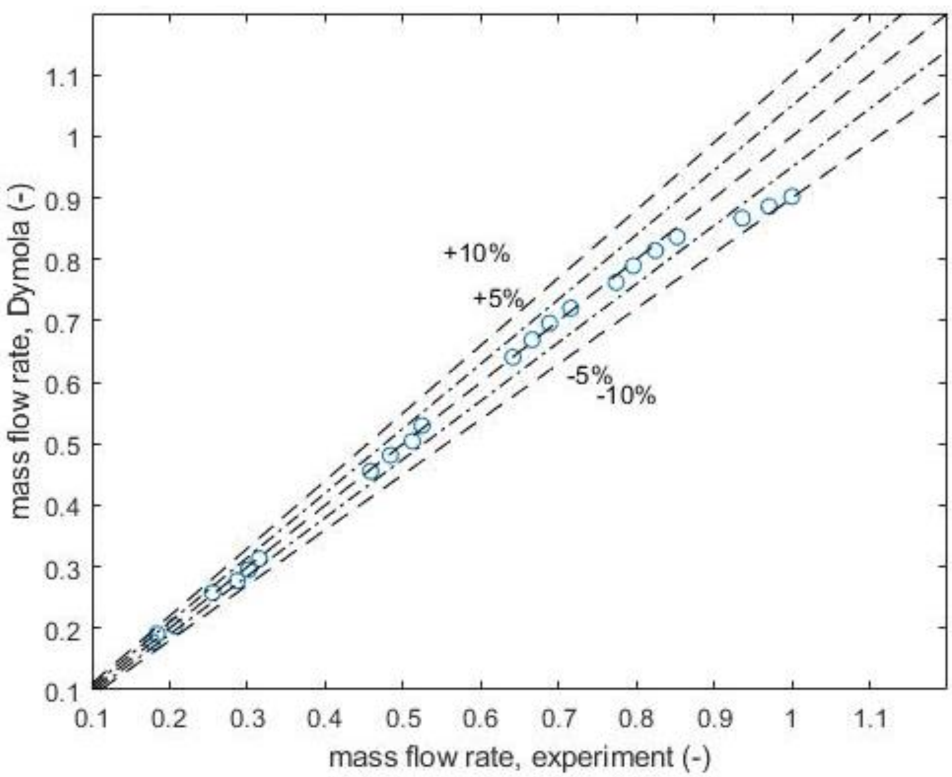

Figure 7: Validation results of the mass flow rate predictions

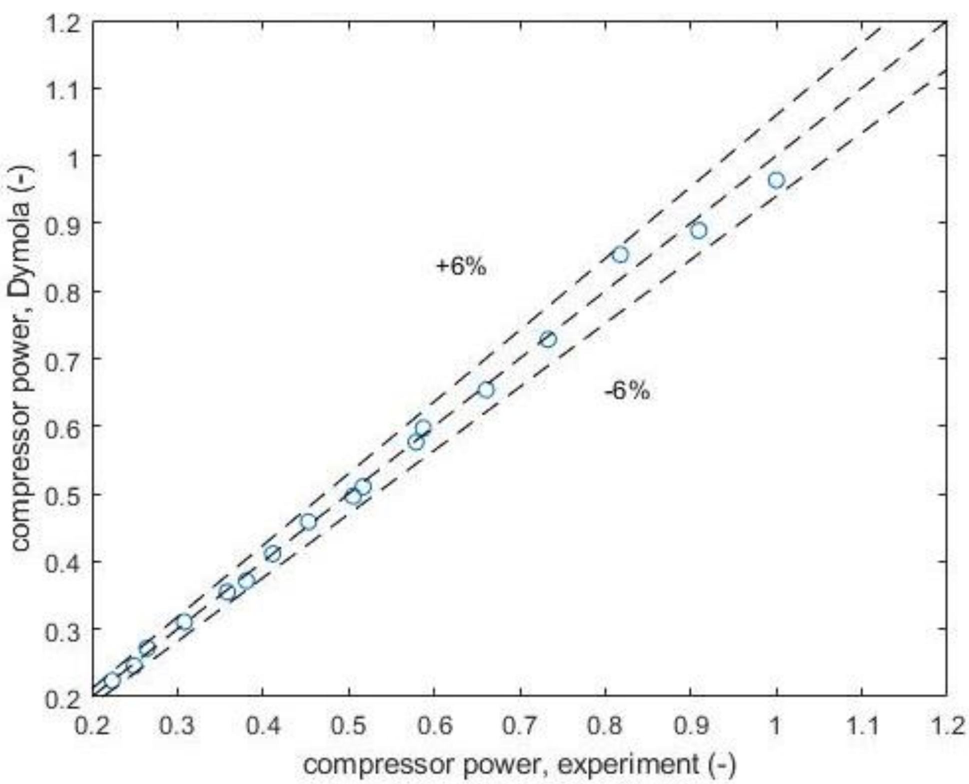

Figure 8: Validation results of the compressor power predictions

The validation results of the sub-cycle compressor are shown in Figure 9 and Figure 10. The maximum deviations of refrigerant mass flow rate and compressor power are less than 3%. And it shares the same speed range as the BC compressor.

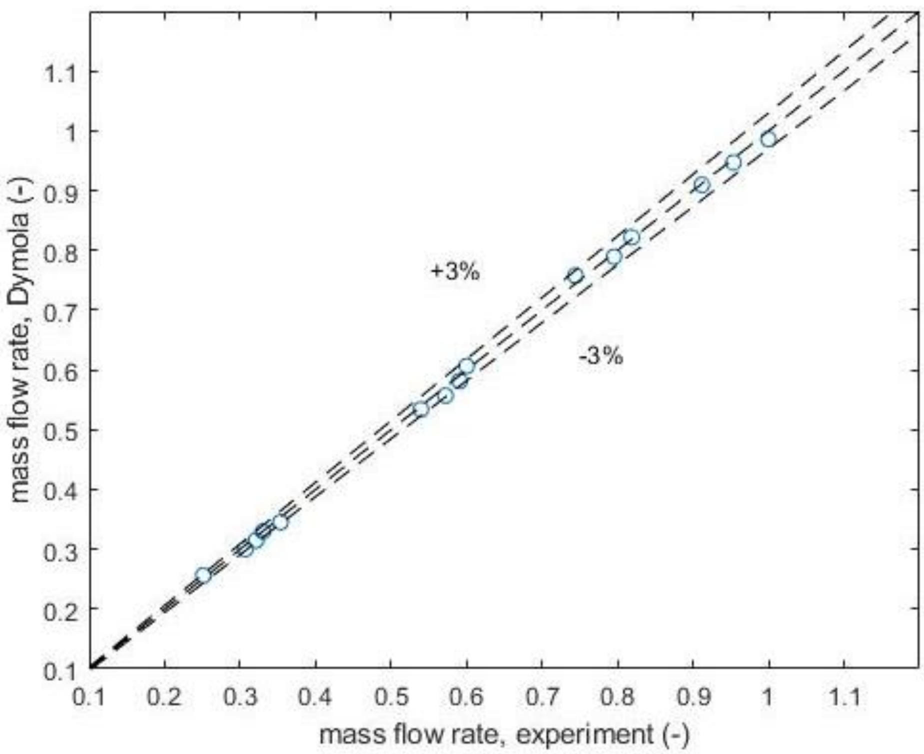

Figure 9: Validation results of the mass flow rate predictions, sub-cycle compressor

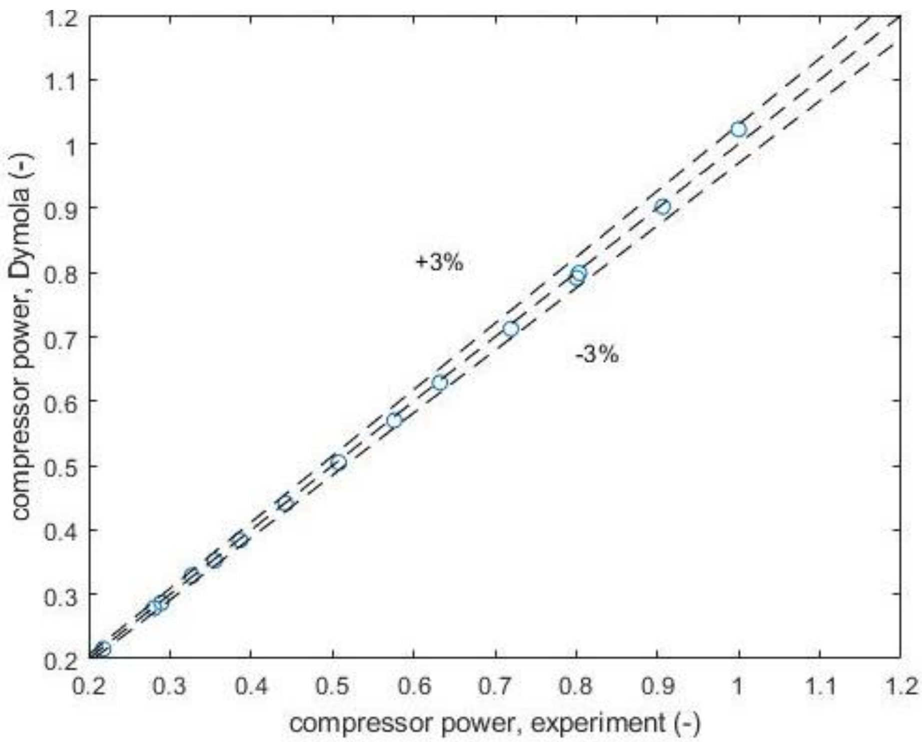

Figure 10: Validation results of the compressor power predictions, sub-cycle compressor

3.2 Vapor injection compressor model

Similar to the single-stage compressor model, vapor injection compressor models can be classified into three categories: empirical models, semi-empirical models, and comprehensive time-dependent models [41].

The empirical model simulates the compressor's performance by using empirical correlations. The ten-coefficient model from AHRI standard 540 [42] for positive displacement compressors is the most used. It has good accuracy in the tested range and does not require any detailed geometry information about the compressor. However, a correction is needed to accommodate the change in suction density because the map was generated at a given suction superheating [43]. Tello-Oquendo et al. [44] built a map-based mode for a vapor injection compressor using a modified AHRI polynomial. When calculating compressor power, an additional term consisting of saturation injection temperature was added to the AHRI polynomial. And in this model, the injection ratio is a function of the pressure ratio of the first compression stage. Other modified AHRI polynomial model for vapor injection compressors includes a 12-coefficient model from Erickson [45] and a 23-coefficient model from Cambio [46] (observed by Lars Sjoholm [47]). In addition, Lumpkin et al. [48] used the Buckingham-PI theorem to develop a new equation for vapor injection compressor's efficiencies, which shows a better R-square value than the ten-coefficient model for most fitted terms.

The semi-empirical model simulates the compression process by using thermodynamic models. Winandy and Lebrun [49] developed a semi-empirical compressor model for a fixed-speed compressor which divides the compression process into four steps: isobaric heating up, isentropic compression, adiabatic, irreversible and constant volume process, and isobaric cooling down. Dardenne et al. [50] improved this model to be suitable for variable speed compressors to solve the compressor's macroscopic performance. Qiao [51] developed a transient vapor injection compressor model that considers the compression process polytropic. And the injection mass flow rate was calculated by a fixed orifice model. Heat losses in major compression modules were also considered to improve accuracy. Wang [52] developed a semi-empirical compressor model as if two compressors connected in serial and have the refrigerant injection in between. The efficiencies of each compression stage have the same form as the ten-coefficient model. Xu [53] developed a similar model and added consideration to heat transfer between compressor parts and ambient. In both models, the first stage efficiencies are functions of evaporating temperature and condensing temperature. And the second stage efficiencies are the function of saturation injection temperature and condensing temperature. Dardenne et al. [50] developed a transient vapor injection compressor model assuming two compressors connected in parallel without consideration of refrigerant mixing. And the injection ratio was used to calculate the injection mass flow rate.

Comprehensive time-dependent models simulate the actual compression process with great geometry details. For example, Jung et al. [10] developed a dynamic model for a vapor injection scroll compressor to evaluate the effects of injection port size and angle. This model type requires many geometry details, such as scroll shape, to build. And is typically used to optimize vapor injection compressor design rather than system-level simulation. Therefore, it is not considered in this study.

3.2.1 Comparison of vapor injection compressor models

For this study, a 30+ cc variable speed vapor injection compressor was modeled. Because the available dataset is minimal (16 test data points from the manufacturer with four different speeds), the conventional ten-coefficient model cannot be used. Instead, two other vapor injection compressor models have been tested: two serial compressors and two parallel compressors.

3.2.1.1 Model 1: Semi-empirical model: Two compressors connected in serial.

In this model, the compression process is separated into two compression stages. The refrigerant vapor is first compressed into the injection pressure in the first compression stage and then mixed with the injection refrigerant. After mixing, the refrigerant is compressed into the discharge pressure in the second compression stage. Each compressor stage is modeled as an efficiency-based compressor model.

Therefore, this model can be quickly developed based on the previous model. The efficiencies required are isentropic efficiency and volumetric efficiency of both compression stages and another compressor efficiency is used to calculate compressor power. The definition of each efficiency is shown as follows:

$$\dot{m} = \rho_{suc} V_{disp} \frac{N}{60} \eta_{vol} \tag{17}$$

$$\eta_{isen} = \frac{h_{dis,s} - h_{suc}}{h_{dis} - h_{suc}} \tag{18}$$

The efficiencies shown above are required for both compression stages. And the definition of compressor efficiency differs slightly from the conventional compressor model. Its deriving process is shown below:

The work done on the refrigerant in the first compression stage is:

$$\dot{W}_1 = \dot{m}_1 (h_{dis,1} - h_{suc,1}) \tag{19}$$

The work done on the refrigerant in the second compression stage is:

$$\dot{W}_2 = \dot{m}_2 (h_{dis,2} - h_{suc,2}) \tag{20}$$

The energy conservation equation for the refrigerant mixing after injection is:

$$\dot{m}_i h_i + \dot{m}_1 h_{dis,1} = \dot{m}_2 h_{suc,2} \tag{21}$$

And the definition of compressor efficiency is:

$$\eta_{comp} = \frac{\dot{m}_1 \left(h_{dis,1} - h_{suc,1}\right) + \dot{m}_2 (h_{dis,2} - h_{suc,2})}{\dot{W}_{input}} \tag{22}$$

Combine above four equations, the below equation is derived:

$$\eta_{comp} = \frac{\dot{m}_2 h_{dis,2} - \dot{m}_i h_i - \dot{m}_1 h_{dis,1}}{\dot{W}_{input}} \tag{23}$$

Therefore, knowing the suction, injection, and discharge states is enough to calculate compressor efficiency. However, information on the discharge state of the first compression stage is still needed to calculate the isentropic efficiency of the first compression stage, which is unknown. As a result, obtaining the isentropic efficiency first and then creating a fitting with it is impossible.

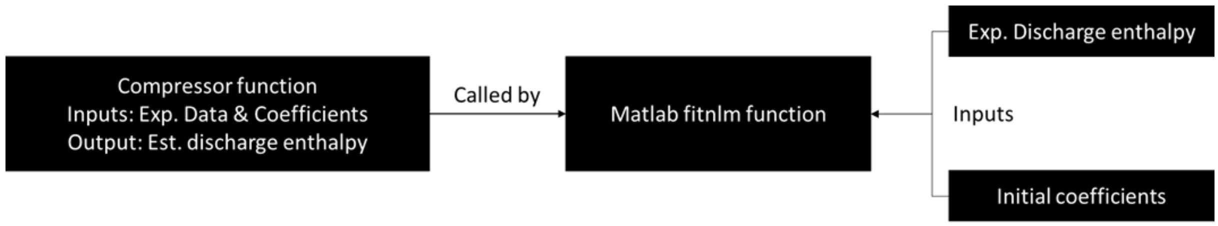

Figure 11: Model 1 fitting process to get isentropic efficiency curve

To solve this issue, I fit the entire process (match the discharge specific enthalpy) instead of the isentropic efficiency. In MATLAB, I created a function of the vapor injection compressor model. The inputs to the compressor model are the parameters measured in the experiment, such as RPM, suction and discharge temperature and pressure, suction/injection/discharge mass flow rates, and fitting variables. And the output of the function is the specific enthalpy at the discharge point. Using the built-in nonlinear fitting function “fitnlm”, I could obtain a series of coefficients that best match the experimental discharge specific enthalpy with the experiment data.

Typically, these efficiencies are fitted using a ten-coefficient polynomial equation [52,53] from AHRI standard 540. However, the accuracy of the ten-coefficient polynomial equation out of the operating envelope is questionable. And compressor speed is not included in the model. As a result, efficiencies were assumed to be functions of pressure ratio and compressor speed. There are a few advantages. First, it requires a smaller number of variables. Second, using the pressure ratio as a variable makes keeping the model within the operating envelope easier.

In literature, the first stage isentropic efficiency is usually a function of evaporating and condensing temperatures [52,53]. Therefore, in this study, the first stage isentropic efficiency was set to be a function of total pressure ratio and compressor speed. The equation is as follows.

$$\eta_{isen,1} = b_1 + b_2 \times PR_{tot} + b_3 \times RPM + b_4 \times PR_{tot} \times RPM + b_5 \times RPM^2 \tag{24}$$

$$PR_{tot} = P_{dis}/P_{suc} \tag{25}$$

The equation of the second compression stage has the same form as the first compression stage while replacing the total pressure ratio with the second stage pressure ratio.

$$\eta_{isen,2} = b_1 + b_2 \times PR_2 \ + \ b_3 \times RPM \ + \ b_4 \times PR_2 \times RPM \ + \ b_5 \times RPM^2 \tag{26}$$

$$PR_2 = P_{dis}/P_{inj} \tag{27}$$

The first stage volumetric efficiency is solved by using the same equation that solves the first stage isentropic efficiency.

$$\eta_{vol,1} = b_1 + b_2 \times PR_{tot} \ + \ b_3 \times RPM \ + \ b_4 \times PR_{tot} \times RPM \ + \ b_5 \times RPM^2 \tag{28}$$

For the second stage volumetric efficiency, the same equation leads to an extremely low adjusted R-square value. Therefore, an additional term was added to the equation. The final form of the equation is shown below.

$$\eta_{vol,2} = b_1 + b_2 \times PR_{tot} \ + \ b_3 \times PR_2 \ + \ b_4 \times RPM \tag{29}$$

The compressor efficiency is expressed as follows:

$$\eta_{comp} = b_1 + b_2 \times PR_{tot} \ + \ b_3 \times RPM \ + \ b_4 \times PR_{tot} \times RPM \ + \ b_5 \times RPM^2 \tag{30}$$

Fittings were created by using a nonlinear fitting function. Results are shown in Table 2.

Table 2: Model 1 fitting results

Parameter	η_{isen}	$\eta_{vol,1}$	$\eta_{vol,2}$	η_{comp}
R square	0.98	0.76	0.6	0.76
Adjusted R square	0.95	0.67	0.5	0.65

Validation of this model is presented in the following chapter, where two models are compared.

3.2.1.2 Model 2: Semi-empirical model: Two compressors in parallel

The second compressor model is considered a parallel model [54]. It also models two compressor chambers: one compresses from the suction point to the discharge point and the other compresses from the injection point to the discharge point. Both chambers discharge at the discharge pressure. Only one isentropic efficiency and volumetric efficiency are needed in this model. In this model, the injection ratio is introduced. The below equation calculates it.

$$X_{inj} = \frac{\dot{m}_i}{\dot{m}_1} \tag{31}$$

And the definition of isentropic efficiency is changed to:

$$\eta_{isen} = \frac{\dot{m}_1\left(h_{dis,s,1} - h_{suc,1}\right) + \dot{m}_i(h_{dis,s,\mathrm{i}} - h_i)}{\dot{W}} \tag{32}$$

And the discharge enthalpy can be calculated by:

$$h_{dis,2} = \frac{\dot{W} + \dot{m}_1 h_{suc,1} + \dot{m}_i h_i - \dot{Q}_{loss}}{\dot{m}_2} \tag{33}$$

Where Q_{loss} is the heat loss to the ambient, since the ambient temperature is unknown in this study, Q_{loss} is set to 0.

And the compressor efficiency (driver efficiency in the paper) is calculated by:

$$\eta_{comp} = \dot{W}/\dot{W}_{input} \tag{34}$$

A more detailed explanation of the model and fitting equations can be found in Dechesne et al. [54]. The same fitting equations were used as the paper used. Similar to the previous compressor model, the nonlinear fitting function in MATLAB was used to generate fitting. The detailed results are discussed later in the comparison chapter.

Table 3: Model 2 fitting results

Parameter	η_{isen}	η_{vol}	X_{inj}	η_{comp}
R square	0.89	0.67	0.92	0.98

Adjusted R square	0.89	0.55	0.89	0.95

3.2.1.3 Comparison of vapor injection compressor models

After implementing the aforementioned compressor models in MATLAB, they were validated against experimental data. All presented results are non-dimensionalized by the maximum values measured in the experiment, as shown below.

$$P_{scaled} = \frac{P}{P_{max,exp}} \tag{35}$$

Where *P* standards for variables that are displayed in the following figure, such as discharge mass flow rate.

Figure 12 shows the validation results of the compressor discharge mass flow rate. The maximum deviation of Model 1 and Model 2 is 8% and 11%, respectively. Figure 13 shows the validation results of the compressor injection mass flow rate. The maximum deviation of Model 1 and Model 2 is 24% and 37%, respectively. This large deviation is due to the injection ratio of Model 2. Figure 14 shows the validation results of the compressor power. And the maximum deviation of the two models is similar. The maximum deviation of Model 1 and Model 2 is 14% and 16%, respectively. In conclusion, even though the fitted variables of Model 2 have better R-square and adjusted R-square than that of Model 1, its final model shows poor performance in all aspects. Therefore, Model 1 was selected.

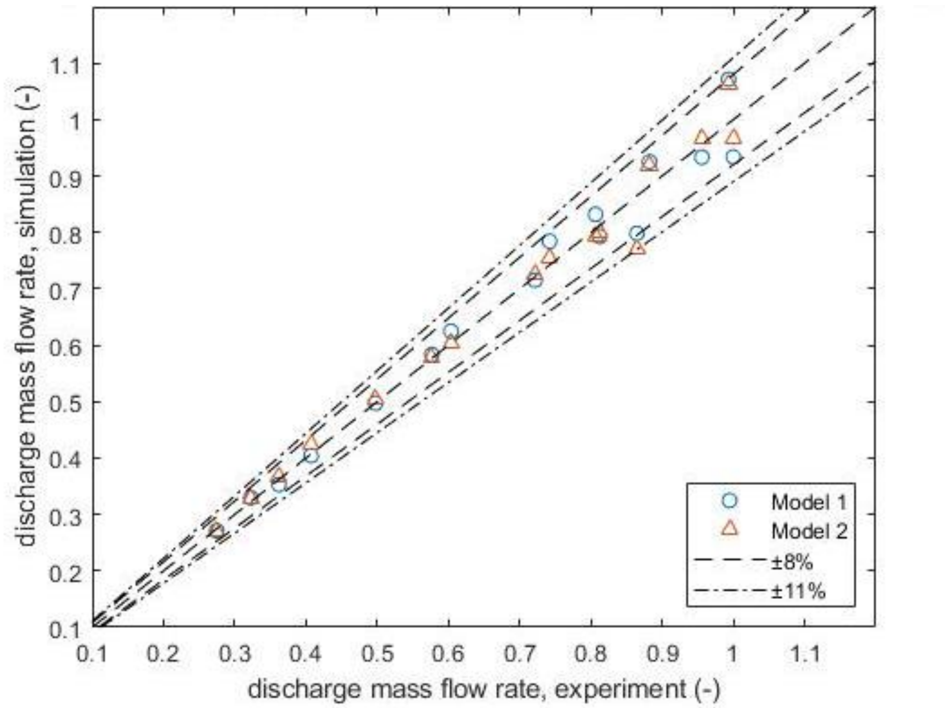

Figure 12: Compressor discharge mass flow rate validation (non-dimensionalized, original unit: kg/s)

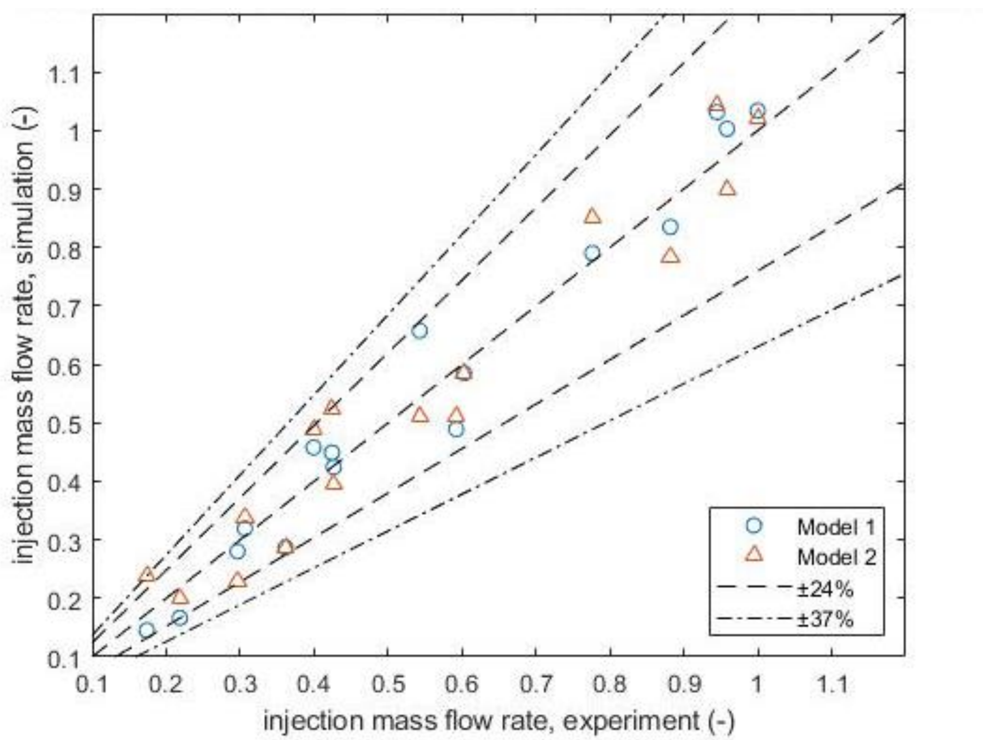

Figure 13: Compressor injection mass flow rate validation (non-dimensionalized, original unit: kg/s)

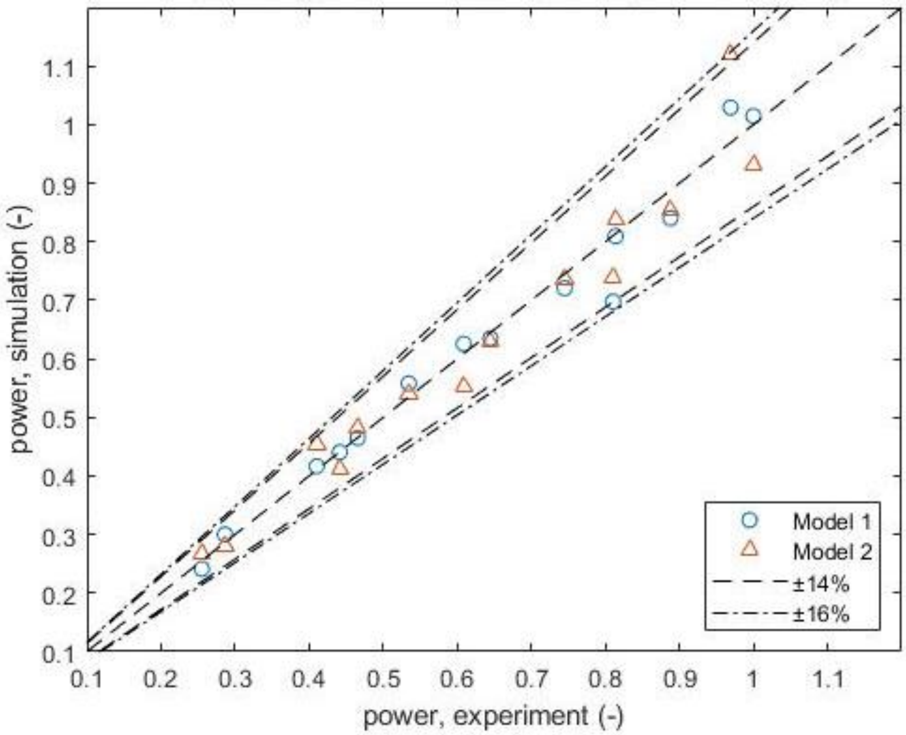

Figure 14: Compressor power validation (non-dimensionalized, original unit: W)

However, both models show significant deviations. The possible reasons for the large deviations in the vapor injection compressor model are summarized as follows:

- The heat loss during the compression was ignored in the model.
- Because flow is driven by the pressure difference, the actual intermediate pressure inside the compressor should be lower than the injection pressure. However, in the model, I assumed that they were the same.
- The isentropic efficiency of the first compression stage in this model was fitted based on the given polynomial equations. Different isentropic efficiency polynomial equations give different results. And this isentropic efficiency affects the calculated discharge enthalpy of the first compression stage as well, which in turn leads to different volumetric efficiencies.

3.3 Base heat pump cycle model

Input boundary conditions include air inlet state and compressor speed. To fix the cycle, suction superheating and condenser outlet subcooling are required. During calculation, the model first guesses the evaporating pressure, condensing pressure, and suction enthalpy. The compressor model then solves for refrigerant mass flow rate and discharge enthalpy. And the condenser outlet enthalpy can be determined by the given condenser subcooling. Then the refrigerant-side capacity of both the condenser and evaporator can be determined. Since heat exchangers are modeled by using approaching temperature, the air outlet temperature can also be calculated based on the given approach temperature and guessed saturation temperature. The calculation goes through an iterative process until the suction superheating matches the given value and the heat exchangers' air-side capacity matches the refrigerant-side capacity.

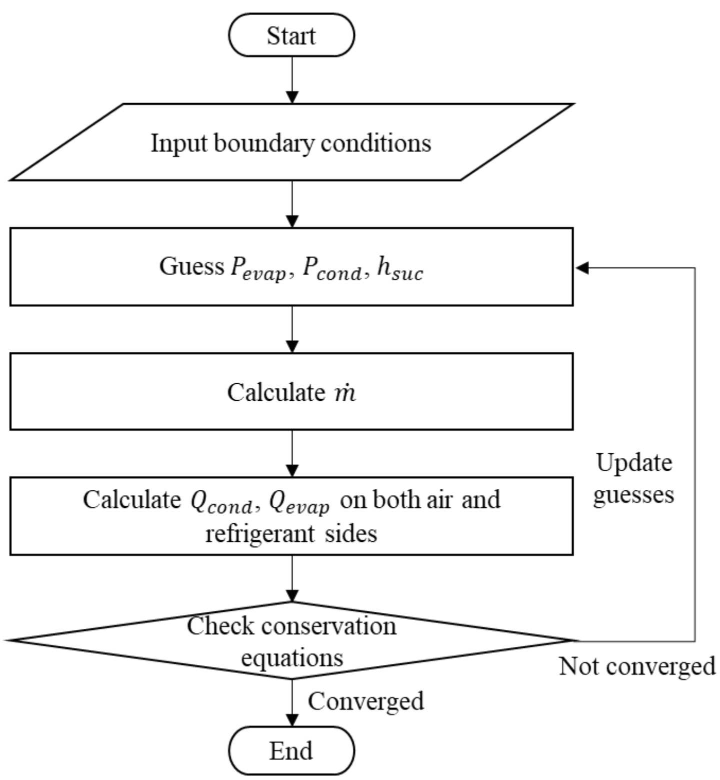

Figure 15: Calculation flowchart of BC thermodynamic model

3.4 Flash tank-based vapor injection heat pump cycle model

FT-VIC model is developed based on the BC model. Because a flash tank is added to the model, its inputs and guess values differ slightly. The flash tank was modeled as a perfect phase separator. Its mass and energy conservation equations are shown below.

$$\dot{m}_{inj} + \dot{m}_{suc} = \dot{m}_{tot} \tag{36}$$

$$\dot{m}_{inj} h_{dew} + \dot{m}_{suc} h_{bubble} = \dot{m}_{tot} h_{cond,out} \tag{37}$$

In the above equations, dew point enthalpy and bubble point enthalpy are functions of injection pressure. Since the compressor model can calculate the refrigerant mass flow rate, there is one equation for two unknowns. Solving these equations requires either injection pressure or condenser outlet enthalpy. However, they cannot be provided simultaneously, which will over-specify the problem. In the current model, the condenser outlet subcooling (equivalent to the condenser outlet enthalpy when condensing pressure is known) is an input, and the injection pressure is guessed. In addition, the vapor injection compressor model cannot solve the second compression stage without knowing the injected refrigerant state and mass flow rate. Therefore, it is necessary to guess either the total refrigerant mass flow rate or the injection mass flow rate. In summary, in the FT-VIC model, in addition to the guess variables mentioned in the BC model, two more guess variables are needed, which are total refrigerant mass flow rate (or injection mass flow rate) and injection pressure (if the inputs include injection pressure, the model does not need to guess condenser outlet enthalpy, as it can be calculated by the model). The calculation also starts from the compressor. The vapor injection compressor first solves the suction mass flow rate. And the flash tank model can calculate the condenser outlet enthalpy and injection mass flow rate, which are used in the vapor injection compressor model to find the suction state of the second compression and actual discharge mass flow rate and state. Then heat exchanger refrigerant-side and air-side capacities can be determined. This calculation also goes through an iterative process until all guess variables match the calculated variables. Note that the convergence of suction enthalpy is determined by comparing the target suction superheating.

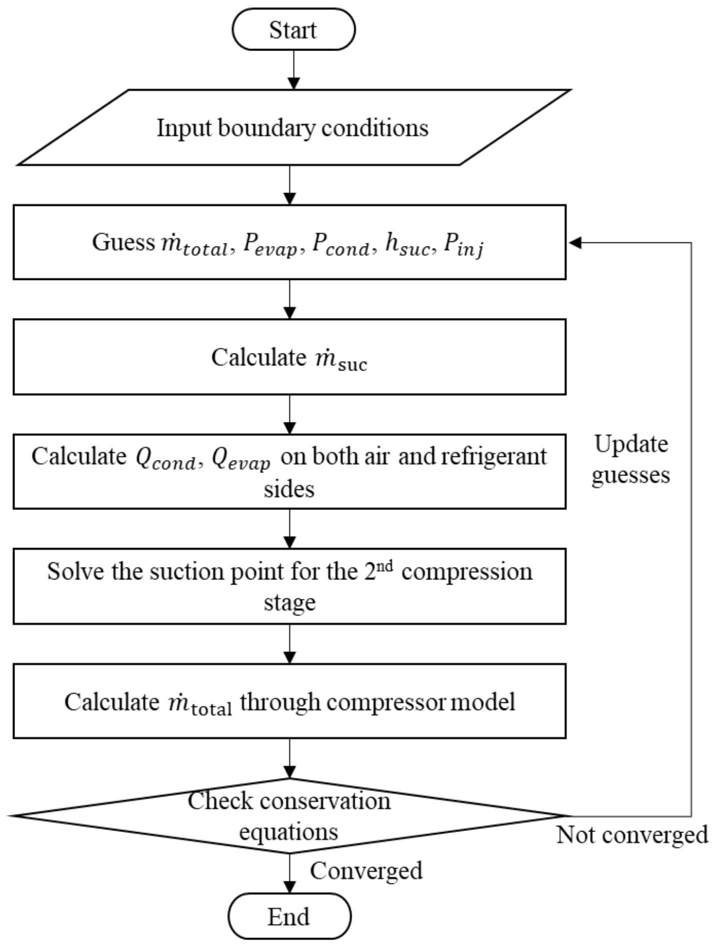

Figure 16: Calculation flowchart of FT-VIC thermodynamic model

3.5 Kangaroo heat pump cycle model

The KC model is developed based on the FT-VIC model. The main-cycle part calculation is the same as the FT-VIC model. Thus, it is not discussed here for brevity. As for the sub-cycle, it is a simplified BC model. The modeling approach of the sub-cycle is the same as that of the BC model. Since both sides of the sub-cycle condenser are in a two-phase region, pure fluid's saturation temperature remains constant when pressure drop is ignored. Therefore, solving the sub-cycle condensing pressure does not require iteration. The rest of the sub-cycle calculation is the same as the BC model.

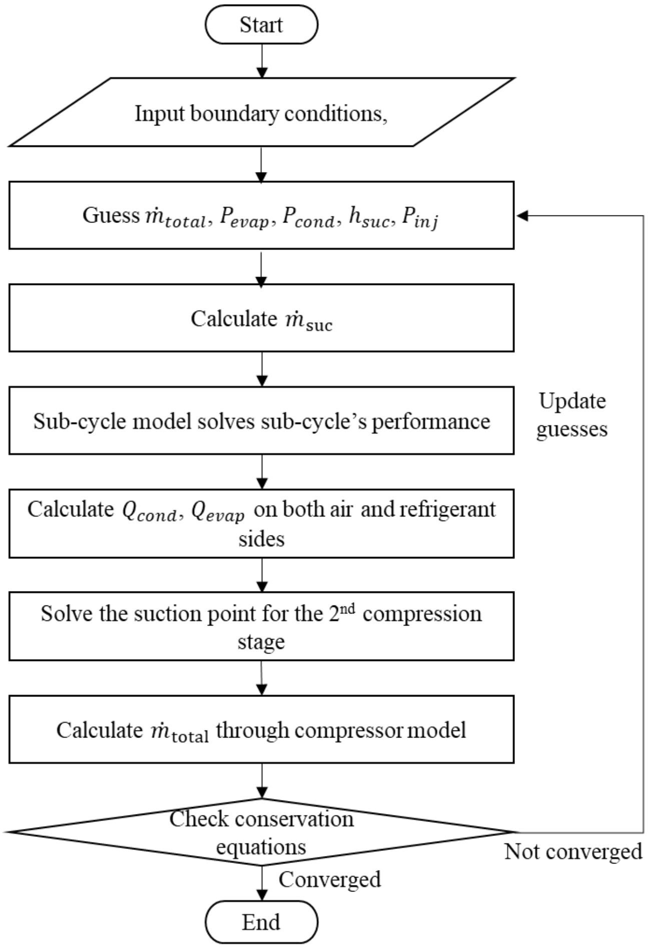

Figure 17: Calculation flowchart of KC thermodynamic model

3.6 Simulation boundary conditions

The developed models were used to compare the cycle performance. In this calculation, the face area of the outdoor heat exchanger is set at 0.142 m^2. Some important boundary conditions for all cycle models are listed in Table 4.

Table 4: Boundary conditions for the thermodynamic model

Parameter	Value	Unit
$T_{sub,cond}$	10	℃
$T_{sup,evap}$	5	℃
$T_{app,evap}$	5	℃
$T_{app,cond}$	10	℃
$T_{app,evap,s}$	5	℃
$T_{app,cond,s}$	10	℃
$T_{sup,evap,s}$	5	℃
$T_{sub,cond,s}$	5	℃

Most conventional MACs have used R134a as their refrigerant [18] due to its good thermophysical properties and nonflammability. However, its high global warming potential (GWP) makes it banned in new light-duty vehicles in the U.S.A. starting in the model year 2021 [55]. R1234yf [18] is one of the most popular alternatives for R134a due to its similar thermophysical properties and negligible GWP. Therefore, in this study, the refrigerant in all calculations is R1234yf.

To compare cycles' performance, calculations were performed based on the simulation matrix shown in Table 5. The cooling mode simulation matrix was from SAE standard J2765 [19]. The heating mode simulation matrix was created to have a similar structure to the cooling mode simulation matrix. In the heating mode, if the condenser's heating capacity is insufficient, a 100% efficient PTC heater is used to fill the capacity gap. Both the heat output and power consumption of the PTC heater are included in the COP calculation.

For VIC and KC, to prevent the compressor model from extrapolation, the maximum overall pressure ratio was capped at 7.66. And the maximum pressure ratio of the BC compressor and the KC's sub-cycle compressor was 8.33. And the speed of all compressor models ranged from 3,000 RPM to 8,600 RPM. If the required compressor speed was lower than the minimum compressor speed, then the minimum compressor speed was used, and vice versa. In addition, to prevent an infeasible solution, the maximum discharge temperature and pressure were set to be 120°C and 3,000 kPa, respectively.

Three operating modes were used in this study: M1, M2, and M3. In M1, BC results were used for all simulation conditions. In M2, FT-VIC was used for extreme conditions, which are tests #1-8 and #37-44. And BC was used for the rest of the simulation conditions. In M3, KC was used for extreme conditions, and BC was used for the rest of the simulation conditions. Note that later during the calculation (using empirical compressor efficiencies), it was found that in simulation #1, even if both the main-cycle compressor and sub-cycle compressor ran at the minimum speed, the model failed to converge. There were two reasons for this model failure: The discharge pressure was higher than the maximum pressure. Second, the discharge temperature was higher than the maximum allowed value. Therefore, when using empirical compressor efficiencies, FT-VIC was used in M3 for simulation #1. Note that calculations using fixed compressor efficiencies were not affected and still used KC in simulation #1.

Table 5: Simulation input matrix

Simulation Number		Mode	Outdoor HX		Indoor HX				
			$T_{air,in}$	V_o	$T_{air,in}$	RH	$\dot{m}_{air}$	Target $T_{air,out}$	
-		-	°C	m/s	°C	-	kg/min	°C	
1		Cooling	45	1.5	35	0.25	9	3	
2			45	2	35	0.25	9	3	
3			45	3	35	0.25	9	3	
4			45	4	35	0.25	9	3	
5			35	1.5	35	0.4	9	3	
6			35	2	35	0.4	9	3	
7			35	3	35	0.4	9	3	
8			35	4	35	0.4	9	3	
9	21		25	1.5	25	0.8	6.5	3	10
10	22		25	2	25	0.8	6.5	3	10
11	23		25	3	25	0.8	6.5	3	10
12	24		25	4	25	0.8	6.5	3	10

13	25		25	1.5	25	0.5	6.5	3	10
14	26		25	2	25	0.5	6.5	3	10
15	27		25	3	25	0.5	6.5	3	10
16	28		25	4	25	0.5	6.5	3	10
17	29		15	1.5	15	0.8	6.5	3	10
18	30		15	2	15	0.8	6.5	3	10
19	31		15	3	15	0.8	6.5	3	10
20	32		15	4	15	0.8	6.5	3	10
33		Heating	5	1.5	5	0	9	30	
34			5	2	5	0	9	30	
35			5	3	5	0	9	30	
36			5	4	5	0	9	30	
37			-5	1.5	-5	0	9	30	
38			-5	2	-5	0	9	30	
39			-5	3	-5	0	9	30	
40			-5	4	-5	0	9	30	
41			-15	1.5	-15	0	9	30	
42			-15	2	-15	0	9	30	
43			-15	3	-15	0	9	30	
44			-15	4	-15	0	9	30	

3.7 Effect of sub-cycle compressor speed

For BC and FT-VIC, compressor speed can be determined by the target cooling capacity. However, KC has two compressors, which makes this problem more complicated. To find out the effect of sub-cycle compressor speed on the cycle performance, a parametric study was performed based on the abovementioned simulation matrix. The calculation was performed for extreme conditions. And during the analysis, the sub-cycle compressor speed ranged from 3,000 RPM to 5,000 RPM with 500 intervals.

Figure 18 shows the parametric study results of the cooling mode. In both ambient temperatures, the system COP decreases as the sub-cycle compressor speed increases. This is because more refrigerant is injected into the compressor when the sub-cycle compressor speed increases. To maintain the condenser capacity, the main compressor speed decreases. In most cases, this results in a decrease in main-cycle compressor power. However, because the increase in sub-cycle compressor power is more significant than the decrease in main-cycle compressor power, the COP still decreases. In addition, sometimes even though the compressor speed decreases, the main-cycle compressor's power consumption is not necessarily reduced due to the increase in discharge mass flow rate. In this calculation, the maximum pressure ratio is limited, which limits the maximum condenser capacity. And the advantage of KC is providing more capacity rather than improving system COP.

When T_{amb} = 35°°, some data points are missing. These calculations failed to converge because they could not reach the target condenser subcooling due to high sub-cycle condenser capacity.

Figure 19 shows the parametric study results of the heating mode. It shares the same trend as the cooling mode.

According to this parametric study, 3,000 RPM is the best sub-cycle compressor speed for extreme conditions for the current model setup. And this speed is used in all calculations later.

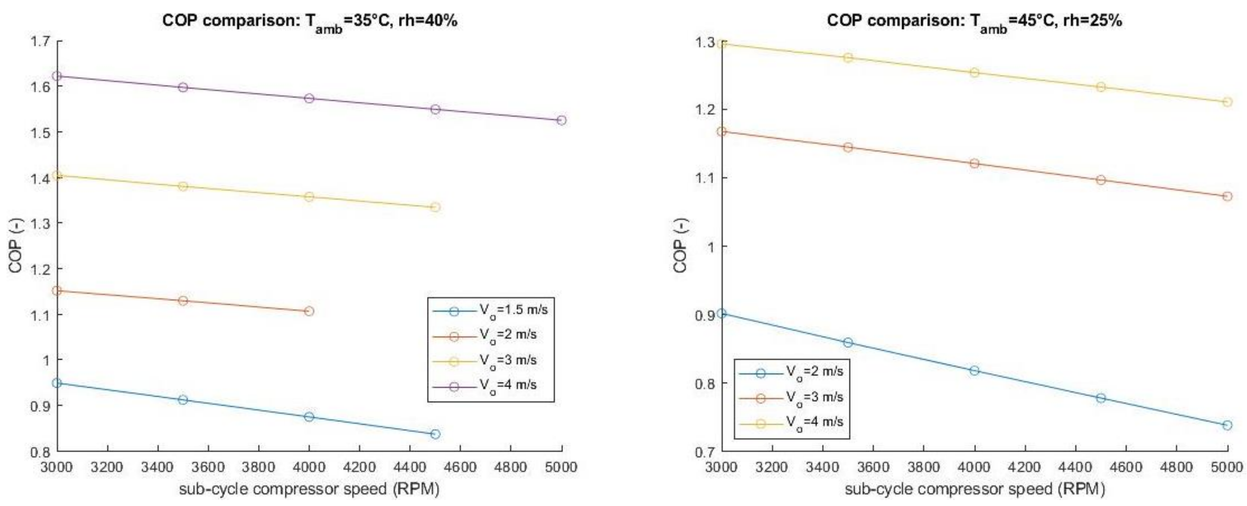

Figure 18: Parametric study for KC, varies sub-cycle comp speed, cooling.

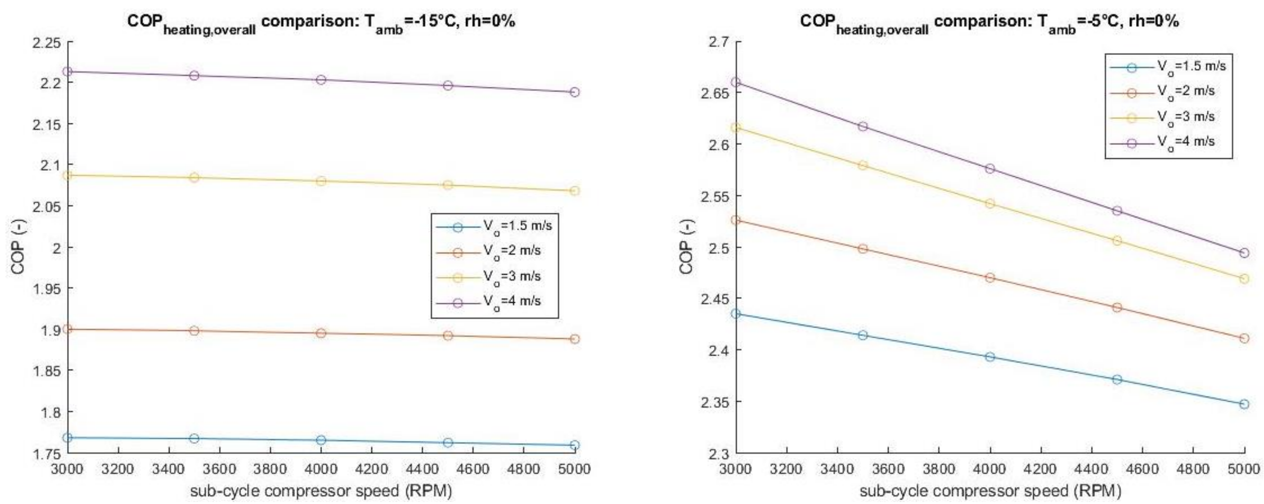

Figure 19: Parametric study for KC, varies sub-cycle comp speed, heating.

3.8 Simulation results based on simulation matrix

Two sets of simulations were performed. As discussed in the previous chapter, both simulations use a semi-empirical vapor injection compressor model. The experimental data fitted the efficiency curves in the first set of simulations. And in the second set of simulations, fixed compressor efficiencies were used [10], listed in Table 6. For the single-stage compressor, first stage efficiencies were used.

Table 6: Fixed compressor efficiency used in the second simulation set.

Parameter	Value
$\eta_{isen,1}$	0.9
$\eta_{vol,1}$	0.7
$\eta_{isen,2}$	0.9
$\eta_{vol,2}$	0.7
η_{motor}	0.7

3.8.1 Results using empirical compressor efficiencies

During the simulation, the FT-VIC model reached the maximum pressure ratio in simulations #1, #2, #3, #5, #6, #41, and #42. And it reached maximum compressor speed in simulations #7, #43, and #44. KC model reached maximum pressure ratio in simulations #2, #3, #6, #41, #42, #43, and #44. And it hit maximum pressure in simulation #5. Also, as mentioned before, the model failed to converge in simulation #1. As for the BC model, it finished the calculation without hitting the maximum pressure ratio limit. However, it reached maximum compressor speed in simulations #2 to #9, #37, and #41 to #44. Figure 20 shows the calculation results for three modes for all simulation scenarios. Because BC is used for the normal operating condition, the results of simulations #9 to #36 are identical. When T_{amb} = 15°C, the target cooling capacity is too small for the system, and the required compressor speed is lower than the minimum compressor speed. Therefore, these simulations used a minimum compressor speed of 3,000 RPM. A similar problem exists from simulations #23 to #28 as well. An increasing trend of cooling capacity can be observed for these simulation conditions. This is because higher velocity means lower temperature difference and pressure ratio when capacity is the same. When the condenser outlet subcooling is fixed, lower condensing pressure means lower condenser outlet specific enthalpy, which leads to higher evaporator enthalpy difference and cooling capacity. In hot weather (simulations #1 to #8), FT-VIC has the highest cooling capacity in most cases and the highest COP in all cases. The only exception is simulation #1, where BC has the highest cooling capacity. This is because the FT-VIC model is constrained by the maximum pressure ratio, while the BC compressor model has a wider operating envelope and can reach higher condensing pressure in this specific case. And KC has a similar cooling capacity as FT-VIC, which is because the introduction of sub-cycle increases the injection ratio. However, the saturation temperature difference is not allowed to change much because the overall pressure ratio is constrained. And the main-cycle compressor speed is reduced to prevent the pressure ratio from exceeding the limit. This leads to a lower suction mass flow rate. So, even though the evaporator enthalpy difference is increased by sub-cycle, evaporator capacity does not necessarily increase. In fact, in many simulations, the cooling capacity decreases slightly. On average, the cooling capacity of KC is 8.8% higher than that of BC. And the cooling capacity of FT-VIC is 10.0% higher than that of BC.

As for heating mode, all three cycles have the same heating capacity because of the PTC heater. And when $T_{amb} = -5°C$, FT-VIC has the highest heating capacity. For KC, the energy saved in the main-cycle compressor could not compensate for the increased energy demand from the sub-cycle compressor speed, which lowers its COP when compared to FT-VIC. The COP of BC is higher than that of KC when the outdoor heat exchanger's air velocity is higher. This is because when capacity is the same, higher velocity means lower temperature difference and lower pressure ratio, which leads to less compressor power consumption. Since the heating load when $T_{amb} = -5°C$ is relatively small and BC can provide enough heating capacity without the help of a PTC heater, KC becomes less efficient when the outdoor heat exchanger's air velocity is high. However, KC performs better than BC for low-speed cases due to the large pressure ratio. And when $T_{amb} = -15°C$, none of these cycles can provide enough heating capacity to meet the heating demand. However, among the three cycles, KC can provide the most heating capacity. As a result, it has the highest overall COP among the three cycles. The advantage would be more evident if the constraint on the pressure ratio were removed.

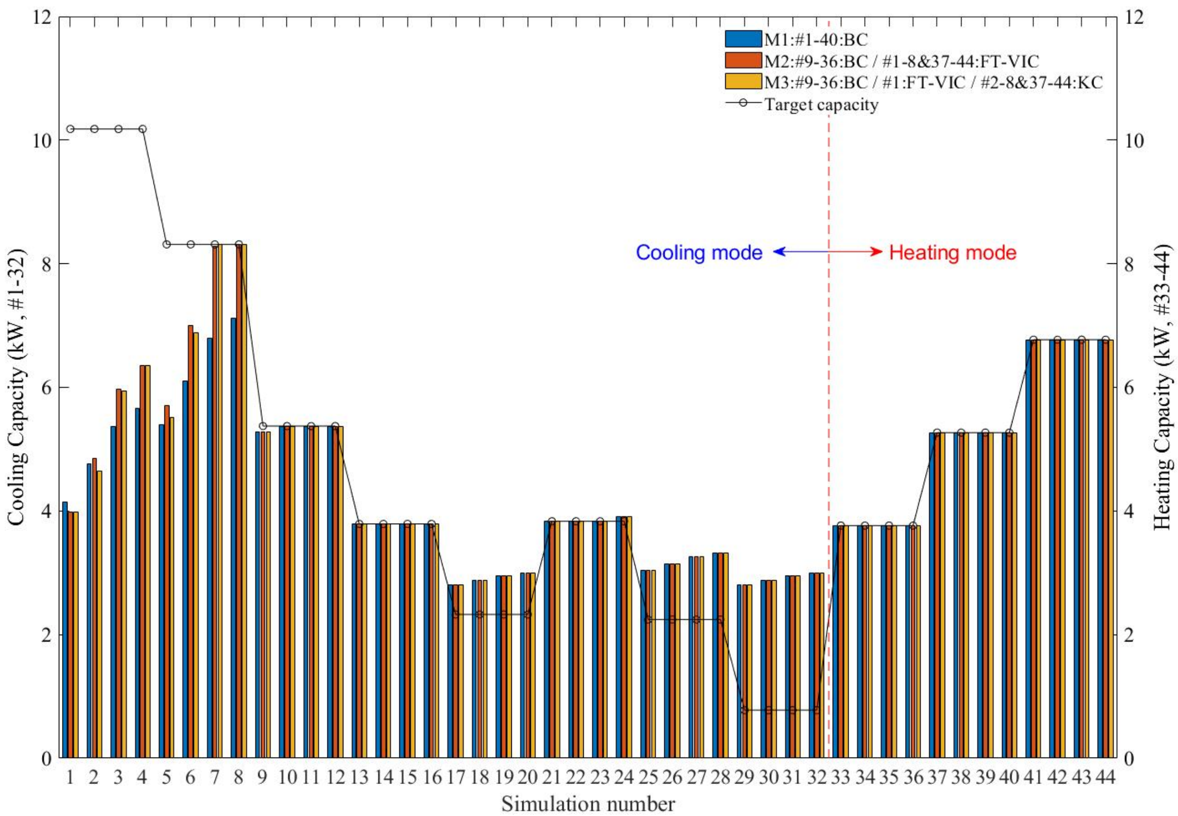

Figure 20: Capacity comparison (empirical compressor efficiencies)

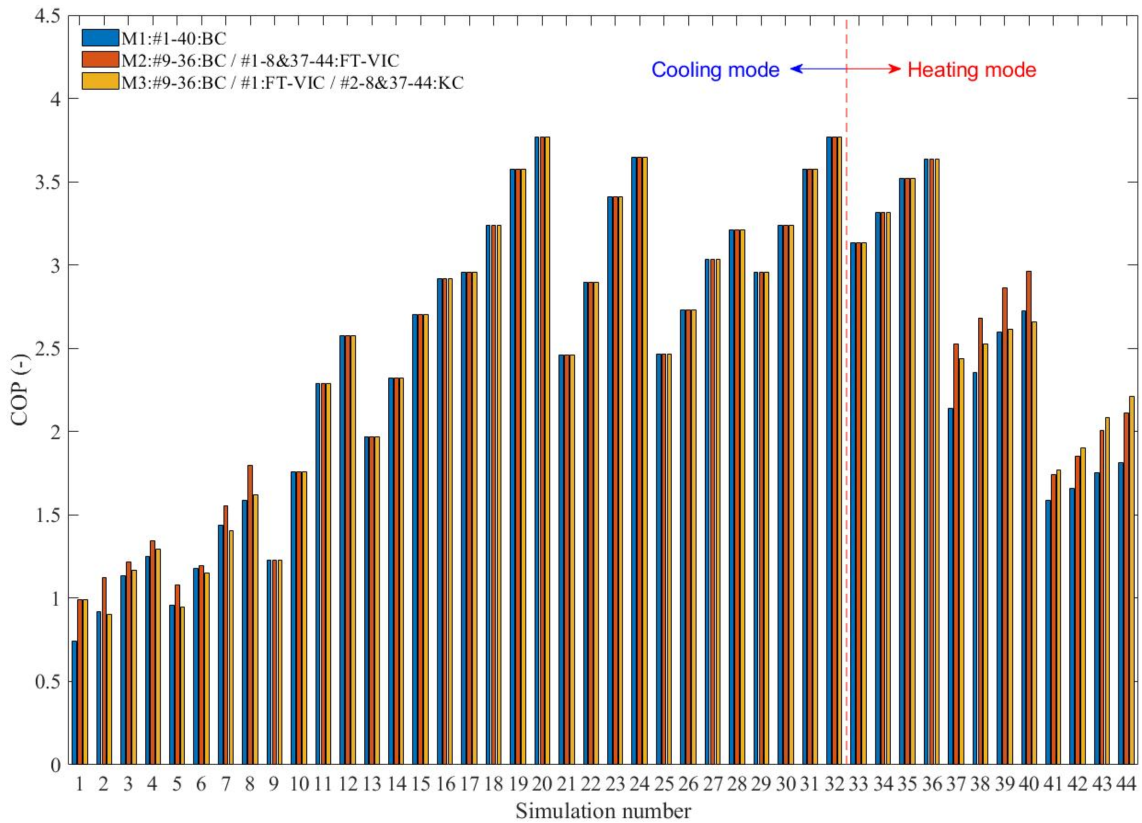

Figure 21: COP comparison (empirical compressor efficiencies)

Table 7: Breakdown of heating capacity when T_{amb} = -15°C (empirical compressor efficiencies)

Simulation Number	M1		M2		M3	
	$\dot{Q}_c$	$\dot{Q}_{PTC}$	$\dot{Q}_c$	$\dot{Q}_{PTC}$	$\dot{Q}_c$	$\dot{Q}_{PTC}$
-	kW	kW	kW	kW	kW	kW
41	59.1%	40.9%	70.1%	29.9%	72.0%	28.0%
42	63.6%	36.4%	76.6%	23.4%	78.9%	21.1%
43	69.0%	31.0%	84.1%	15.9%	87.4%	12.6%
44	72.2%	27.8%	88.4%	11.6%	92.4%	7.6%

3.8.2 Results using fixed compressor efficiency

Figure 22 shows the capacity comparison results. In hot weather (simulations #1 to #8), the cooling capacity of KC is on average 28.1% higher than that of BC. And the cooling capacity of FT-VIC is on average 23.6% higher than that of BC. And in simulations #1 to #5, cooling capacities are limited by the maximum condensing pressure.

Figure 23 shows the comparison of system COP. For simulations #6 to #8, the COP of the KC is 12% and 11% lower than that of BC and FT-VIC, respectively. For simulations #1 to simulation #5, FT-VIC has a similar COP as that of KC. And KC's COP is on average 4% higher than that of BC.

Table 8 shows the breakdown of heating capacity when T_{amb} = -15°C. As shown, KC dramatically increases the heating capacity, reducing the PTC heater percentage and improving system COP. Compared to the BC, the heating capacity of the KC is on average improved by 28.8% when T_{amb} = -15°C.

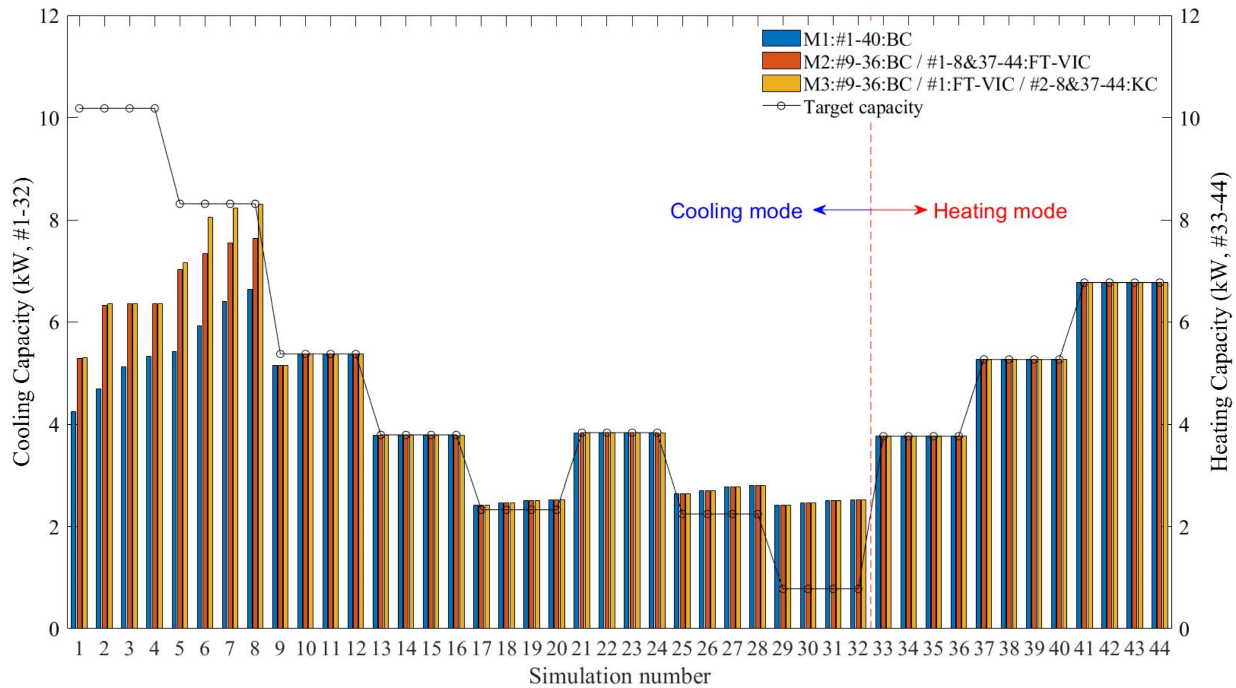

Figure 22: Capacity comparison (fixed compressor efficiencies)

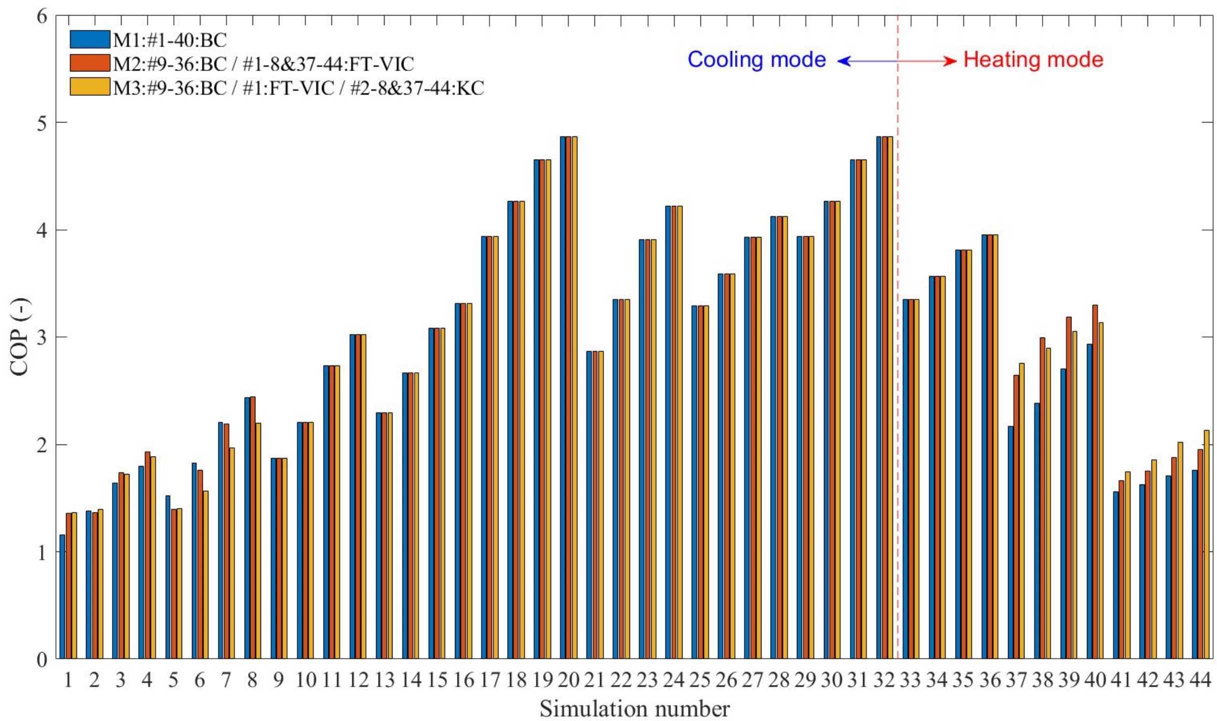

Figure 23: COP comparison (fixed compressor efficiencies)

Table 8: Breakdown of heating capacity when T_{amb} = -15°C (fixed compressor efficiencies)

Simulation Number	M1		M2		M3	
	$\dot{Q}_c$	$\dot{Q}_{PTC}$	$\dot{Q}_c$	$\dot{Q}_{PTC}$	$\dot{Q}_c$	$\dot{Q}_{PTC}$
-	kW	kW	kW	kW	kW	kW
41	49.6%	50.4%	55.8%	44.2%	62.6%	37.4%
42	53.0%	47.0%	59.9%	40.1%	67.7%	32.3%
43	57.1%	42.9%	65.0%	35.0%	74.1%	25.9%
44	59.4%	40.6%	68.0%	32.0%	78.0%	22.0%

3.9 Heating performance comparison

The previous calculation aimed to meet the target cooling or heating capacity and then compare the system COP. However, the advantage of KC is providing more heating capacity at the sacrifice of more power consumption. Another parametric study was performed to show how much KC can provide more heating capacity compared to BC and FT-VIC with the same speed. In this parametric study, N_s was fixed at 3,000 RPM. And N_m ranged from 3,000 RPM to 8,000 RPM. However, not all calculations converged. Here only the cases where all three models converged are discussed. Compared to BC and T_{amb} = -5°C, KC on average increases heating capacity and decreases COP by 34.0% and 28.6%, respectively. And when compared to BC and T_{amb} = -15°C, KC on average increases heating capacity and decreases COP by 32.2% and 22.7%. Compared to FT-VIC and T_{amb} = -5°C, KC on average increases heating capacity and decreases COP by 25.7% and 25.8%, respectively. And when compared to FT-VIC and T_{amb} = -15°C, KC on average increases heating capacity and decreases COP by 20.1% and 18.9%. In addition, the increment of capacity increases as N_m increases. And the reduction of COP decreases as N_m increases.

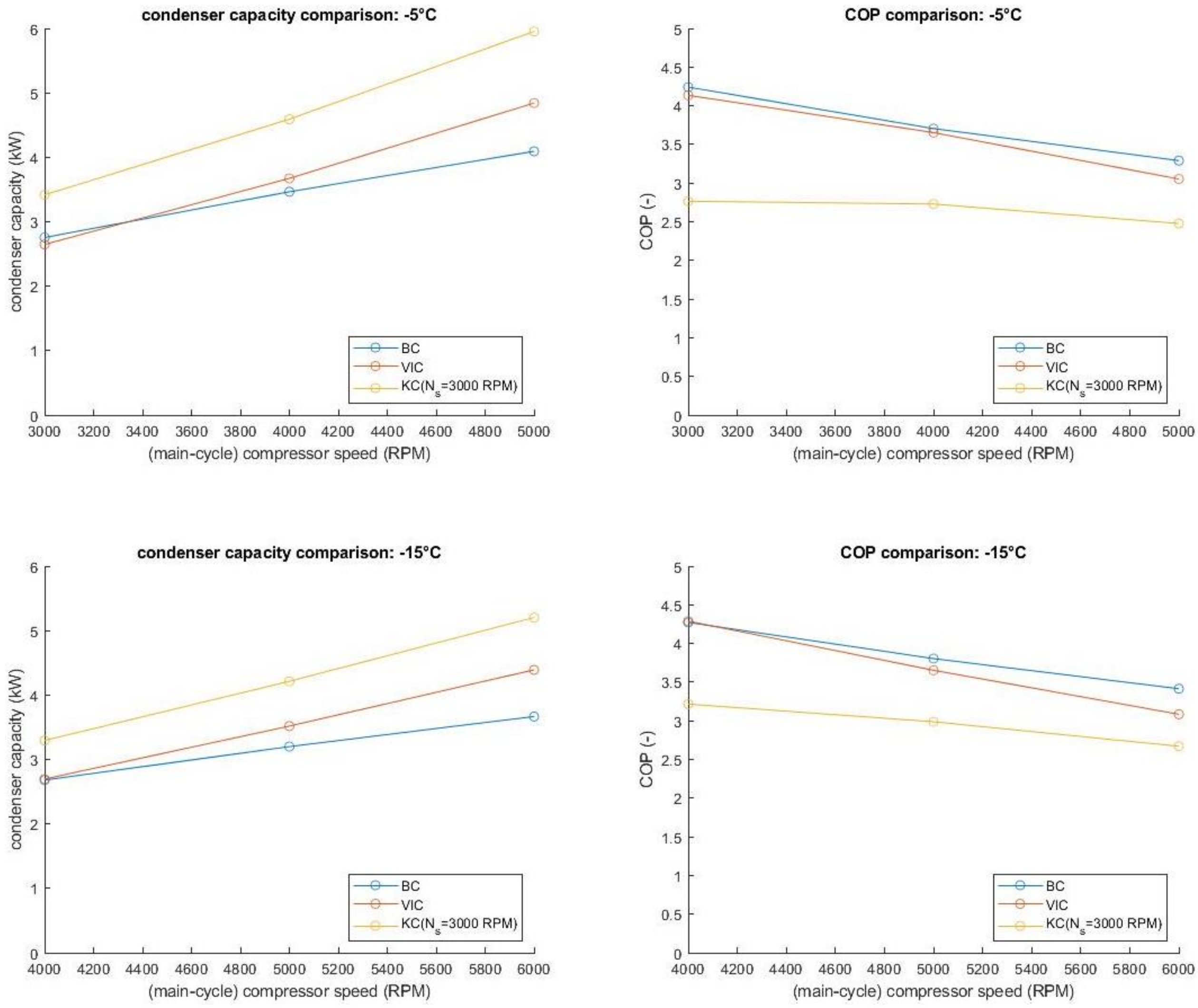

Figure 24: Heating performance comparison

3.10 Annual energy consumption calculation

To evaluate the annual energy consumption of cycles, the method used in LCCP evaluation [16,17] was used.

The first step of annual energy consumption is to process the weather data. TMY3 database [56] was used, which includes hourly weather data of a typical meteorological year for various locations in the U.S.A. In addition to the existing data from the TMY3 database, it was necessary to calculate the mean radiant temperature for each hour, which was later used in the thermal comfort model. The equation for mean radiant temperature is shown below [57].

$$T_{mrt} = T_{amb} + \frac{17\int_0^t \dot{Q}_{solar}}{6800} \tag{38}$$

Where $\int_0^t Q_{solar}$ is accumulated solar radiation, and its unit is Wh/m^2. One limitation of the above equation is that the accumulated solar radiation is monotonically increasing, which leads to inconstant temperatures across midnight. To solve this problem, a correction factor was applied. Because solar radiation usually caps at 15:00 and is almost non-exist at 20:00, the correction factor was set at 1 before 15:00 and 0 after 20:00. A linear function was used in between.

Based on SAE standard J2766 [16], the temperature bin method was used to process the weather data. And the average values of each temperature bin were used. Same as the standard, only the data between 6:00 and 24:00 were used during the calculation.

In this study, dry bulb temperatures were grouped into eight bins. Six ranges from -20°C to 40°C with 10°C intervals. And the rest two bins cover both ends. After grouping, the frequency (percentage over a typical meteorological year), average temperature, average relative humidity, and the average mean radiant temperature was calculated.

After processing the weather data, a cabin thermal comfort model [57–59] was used to calculate the manually controlled AC on-time. The below equations calculated the Predict Mean Vote (PMV).

$$PMV = (0.303e^{-0.036M} + 0.028) \times (M - E_{diff} - E_{rsw} - E_{res} - C_{res} - R - C) \tag{39}$$

$$E_{diff} = 3.05(5.73 - 0.007M - p_a) \tag{40}$$

$$E_{rsw} = 0.42(M - 58.15) \tag{41}$$

$$E_{res} = 0.0173M(5867 - p_a) \tag{42}$$

$$C_{res} = 0.0014M(34 - T_a) \tag{43}$$

$$R = 3.96 \times 10^{-8} f_{cl}[(T_{cl} + 273)^4 - (T_{mrt} + 273)^4] \tag{44}$$

$$C = f_{cl} h_c (T_{cl} - T_a) \tag{45}$$

Where *M* is the rate of metabolic heat production, E_{diff} is the rate of heat loss from the evaporation of moisture diffused through the skin, E_{rsw} is the rate of heat loss from sweat evaporation, E_{res} is the rate of evaporative heat loss from respiration, C_{res} is the rate of convective heat loss from respiration, *R* is radiation heat loss from the skin, *C* is the rate of convective heat loss from the skin. The equations below calculate the partial vapor pressure in the air [60].

$$p_s = \begin{cases} 0.61121 e^{\left[\left(18.678 - \frac{T_a}{234.5}\right)\left(\frac{T_a}{257.15 + T_a}\right)\right]}, & T > 0 \\ 0.61115 e^{\left[\left(23.036 - \frac{T_a}{333.7}\right)\left(\frac{T_a}{279.82 + T_a}\right)\right]}, & T < 0 \end{cases} \tag{46}$$

$$p_a = \frac{RH}{100} \times p_s \tag{47}$$

And the clothing's outer surface temperature T_{cl} could be calculated using the equations below through an iterative process.

$$T_{sk,req} = 35.7 - 0.0275M \tag{48}$$

$$T_{cl} = T_{sk,req} - I_{cl} \times clo \times (R - C) \tag{49}$$

The clothing area factor was calculated by:

$$f_{cl} = \begin{cases} 1.0 + 0.2 I_{cl}, & I_{cl} \le 0.5clo \\ 1.05 + 0.1 I_{cl}, & I_{cl} > 0.5clo \end{cases} \tag{50}$$

Where 1 clo = 0.155 m^2K/W. The convective heat transfer coefficient could be calculated by using the below equation.

$$h_c = \max\left(2.38(T_{cl} - T_a)^{0.25}, 12.1\sqrt{V_a}\right) \tag{51}$$

And the below equation could calculate the percent predicted dissatisfied (PPD), which is also the system on-time.

$$PPD = 100 - 95e^{-0.03353PMV^4 - 0.2179PMV^2} \tag{52}$$

Ambient temperature and relative humidity were used to evaluate thermal comfort. In this calculation, it was assumed that the rate of metabolic heat production was 1.5 met (driving, =87.15 W/m^2), and the air velocity was assumed to be 0.1 m/s [16]. As for the clothing insulation, in cooling mode I_{cl} = 0.61 clo (trousers, long-sleeved shirt), and in heating mode I_{cl} = 1.01 clo (trousers, long-sleeved shirt, long-sleeved sweater, T-shirt) [58].

Polynomial equations were fitted based on simulation results mentioned in the previous chapter. These polynomial equations were functions of vehicle speed and were used to predict system capacity and power consumption. The vehicle speed was categorized into four categories, and the relationship between outdoor heat exchanger air face velocity and vehicle speed is listed in Table 9. In addition to the compressor power consumption, fan power was also considered, which was calculated by using the profile provided in the Green-MAC-LCCP tool [17].

$$W_{tot} = W_{sys} + W_{fan} \tag{53}$$

Table 9: Vehicle velocity profile

Speed category	Vehicle velocity	Outdoor HX air face velocity
-	km/h	m/s
Idle	10	1.5
Low	25	2
Medium	65	3
High	80	4

To calculate the annual energy consumption, the energy consumption for one full driving cycle was first calculated. A driving cycle is a vehicle speed profile that mimics actual driving behavior. In this study, the driving cycle used in the calculation is a combination of the Federal Test Procedure (FTP-75) and the Highway Fuel Economy Driving Schedule (HWFET) [20].

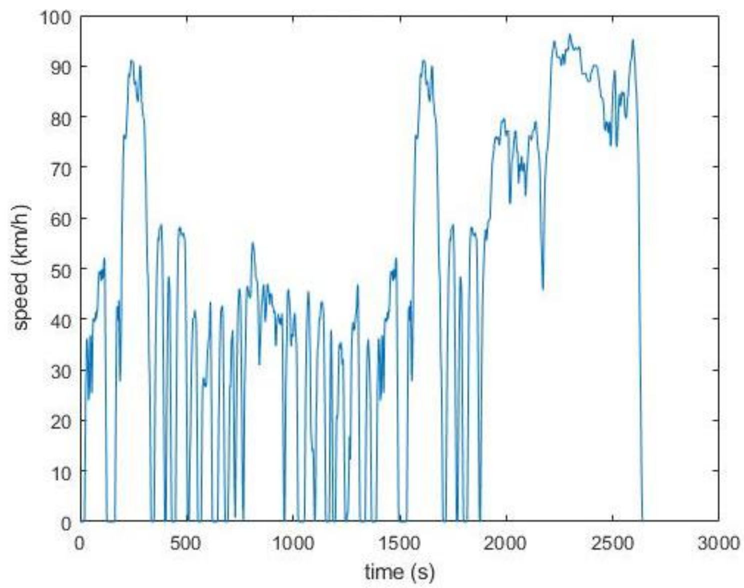

Figure 25: Driving cycle: FTP-75+HWFET

The energy consumption of one driving cycle was performed second-by-second using the abovementioned polynomial equations. In addition, to take the effect of relative humidity into the calculation, the relative humidity correction factor from SAE standard J2766 [16] was used to correct cooling capacity. Since it did not include a correction factor for 45°C, the correction factor for 35°C was used for 45°C cases.

The annual driving distance (D_{annu}) was assumed to be 20,050 km [16], equivalent to roughly 586 driving cycles. The total number of driving cycles was then assigned to each temperature bin according to their percentage. And the annual energy consumption was calculated by the below equation.

$$W_{annual} = n_{DC} \sum [W_{dc} \times pct_{tb} \times (pct_M \times OT + pct_A)] \tag{54}$$

Where n_{DC} is the total number of the driving cycle, W_{dc} is the power consumption of one driving cycle, pct_{tb} is the percentage of each temperature bin, OT is the percentage of the manually controlled system on time, pct_M is the percentage of manually controlled, and pct_A is the percentage of the auto-controlled system. In this study, pct_M was assumed to be 65%. And for the auto-controlled system, its system on-time was assumed to be 100%.

The calculation result of W_{dc} shows that when T_{amb} = -15°C, W_{dc} of KC is 14.1% and 3.1% lower than that of BC and FT-VIC, respectively. Of course, carrying additional weight diminishes energy savings. According to Weiss et al. [61], a typical passenger car consumes 0.6 ± 0.1 kWh energy per 100 km per 100 kg. Therefore, we set incremental energy consumption (IEC) to be 6×10^{-5} kWh/(kg×km). The weight of BC was the default value from the Green-MAC-LCCP tool, and it was assumed that the FT-VIC had the same weight. While the KC was assumed to have 25% more weight due to additional components. After factoring in the extra energy consumption due to carrying additional weight, the energy-saving was reduced to 13.8% (vs. BC) and 2.7% (vs. FT-VIC). This energy-saving helps extend the driving distance of the vehicle in extremely cold weather.

The annual energy consumption of all locations in the TMY3 database was evaluated. And these results were then averaged by the state to create state-level results.

3.11 LCCP calculation

As mentioned in the literature review, LCCP consists of two parts: direct emission and indirect emission. The direct emission was calculated by using the same method and number from the SAE J2766 standard [16].

Belt efficiency and alternator efficiency were removed from the calculation as the belt no longer drives the compressor, and the electricity directly comes from the battery. Instead, two efficiencies were introduced to the model. One is the electricity transmission and distribution efficiency η_{td}. According to U.S. EPA, roughly 5% of electricity is lost during transmission and distribution [62]. Therefore, in this study η_{td} = 95%. The other added efficiency is charging efficiency η_{charge}. A typical lithium-ion battery has 80% to 90% charging efficiency [63,64]. As a result, in this study η_{charge} = 85%.

The conversion factor mentioned in the standard was for fossil fuel. However, in this study, the electricity comes from power plants. Therefore, the conversion factor C_1 is obtained by times the U.S. average emission factors [65] of each greenhouse gas with its GWP (100-year time horizon) [66]. The equation for solving LCCP is shown below.

$$LCCP = Direct\ Emission + Indirect\ Emission \tag{55}$$

$$\begin{aligned} &Direct\ Emission \\ &\quad = GWP(direct\ from\ MACs\ leakage) \\ &\quad + GWP(direct\ from\ additional\ sources) \end{aligned} \tag{56}$$

$$\begin{aligned} &Indirect\ Emission \\ &\quad = GWP(Indirect\ from\ MACs\ operation) \\ &\quad + GWP(Indirect\ from\ additional\ sources) \end{aligned} \tag{57}$$

$$Indirect\ emission\ from\ MACs\ operation = W_{tot} \times Life \times C_1/(\eta_{td} \times \eta_{charge}) \tag{58}$$

$$\begin{aligned} &Indirect\ emission\ from\ transportation \\ &\quad = Weight \times IEC \times D_{annu} \times Life/(\eta_{td} \times \eta_{charge}) \times C_1 \end{aligned} \tag{59}$$

$$C_1 = GWP_{CO_2}C_{co_2} + GWP_{N_2O}C_{N_2O} + GWP_{CH_4}C_{CH_4} \tag{60}$$

As mentioned before, carrying MACs also consumes energy. Equation (59) was used to account for the emission caused by transportation.

The input variables for LCCP calculation are listed in Table 10, whose values come from Green-MAC-LCCP tool version 3b [17] and SAE J2766 standard [16]. VIC is assumed to have the same weight as BC, and KC is 25% heavier than BC due to additional required components.

Table 10: Parameters for LCCP calculation

Parameter name	Unit	Value
Refrigerant charge (BC)	g	550
Charge (FT-VIC)	g	550
Charge (KC)	g	687.5
Refrigerant lost in the assembly	g	3.5
Leak rate	g/year	8.8
Leakage before service	g	200
Leakage due to accident	g/year	17
Vehicle lifetime	year	9
Percentage of DIY service	%	25
Leakage during professional service	g/service	35
Leakage during DIY service	g/service	52
Loss from can heels during professional service	g/service	5
Loss from can heels during DIY service	g/service	108
Weight (BC)	kg	20.2
Weight (FT-VIC)	kg	20.2
Weight (KC)	kg	25.25

3.12 LCCP results

3.12.1 Results using empirical compressor efficiencies

Figure 26 shows the simulation results of annual operating energy consumption across the U.S. Note that this calculation did not consider the energy cost to carry the system. Overall, southern and northern states consume more energy due to high cooling or heating demand. Although FT-VIC has a higher COP than BC in all simulation scenarios, its capacity is also higher than that of BC. As a result, its total power consumption could be higher than that of BC. The calculation result shows that M2 has the lowest energy consumption in 34 states, which makes it the most efficient mode. M3 has lower energy consumption than M1 in 21 states, most of which are northern states. And it has lower energy consumption in these states mainly due to its high efficiency in the heating mode. And in all states, M3 has higher energy consumption than

M2 as M3 has lower COP in most simulation scenarios. On average, the annual energy consumption of M3 is 1.3% higher than that of M1 and 3.0% higher than that of M2.

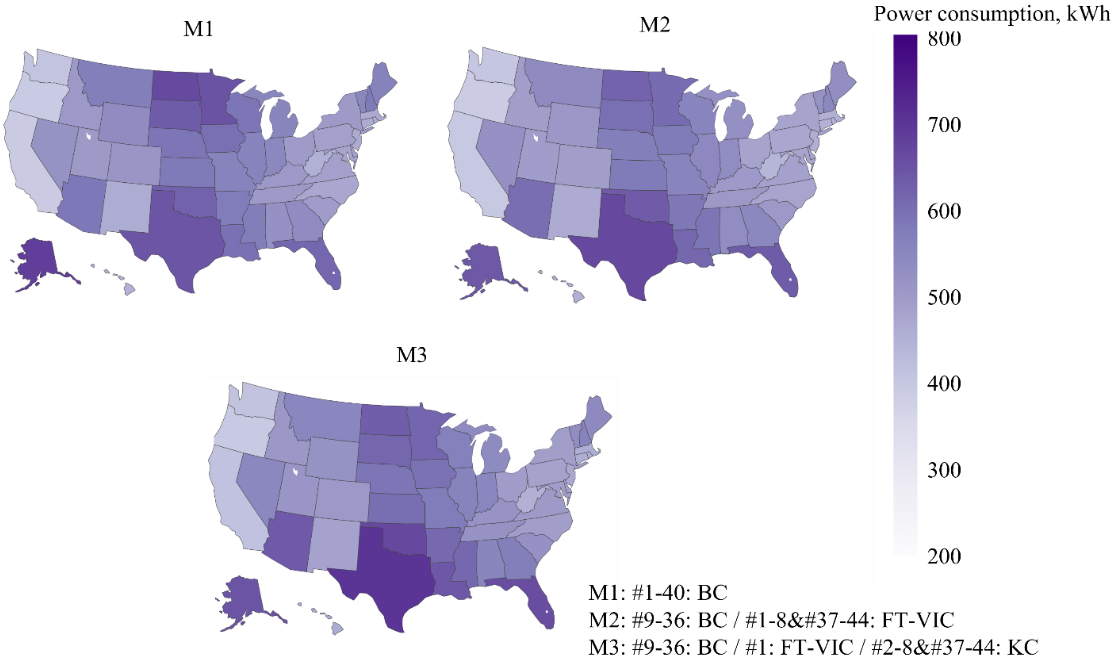

Figure 26: Choropleth maps of annual operating energy consumption (empirical compressor efficiencies)

Figure 27 shows the choropleth maps of LCCP simulation results. Because all states share the same conversion factor, the pattern remains like the choropleth maps of annual operating energy consumption. M2 has the lowest LCCP in 34 states, like the annual operating energy consumption results. Although M3 is more efficient than M1 in many states, the additional emission caused by carrying extra weight reduces its advantage. The LCCP of M3 is lower than M1 in 11 states. And because M2 is more efficient than M3, its LCCP is also lower than M3 in all states. Nationwide averaged data show that M3 has a 3.0% higher emission than M1 and 4.6% higher emission than M2, while the emission of M2 is 1.5% lower than that of M1.

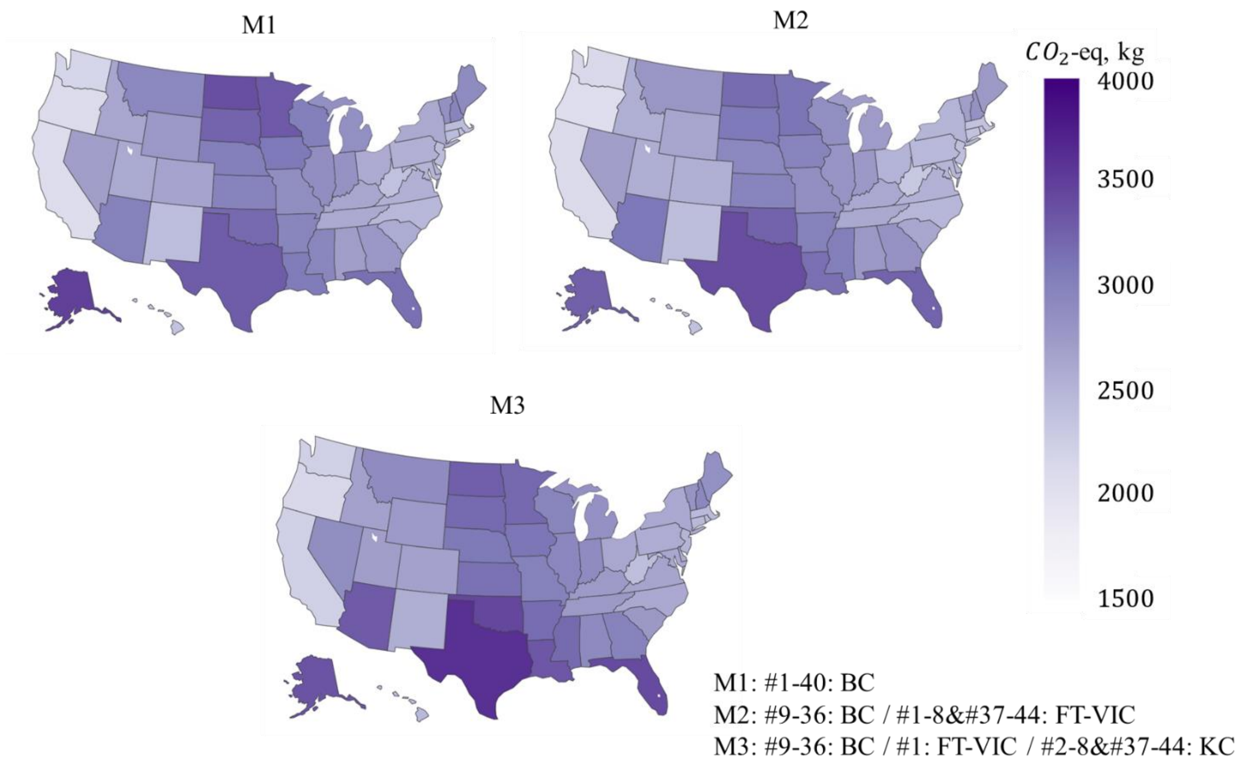

Figure 27: Choropleth maps of LCCP CO_2-equivalent emission (empirical compressor efficiencies)

Figure 28 shows the breakdown of LCCP at various selected locations. Because the GWP of R1234yf is extremely small, the direct emission is negligible. The significant contribution to LCCP is operating emissions, followed by transportation emissions. And the last portion that is visible is the manufacture and end-of-life emission. As mentioned before, though FT-VIC has a higher COP than BC in hot weather, its cooling capacity is also higher, which could lead to higher power consumption. As a result, for cities with a hot climate like Phoenix and Miami, M1 has the lowest LCCP. And in the cold region, M2 has the lowest LCCP among the three cycles. In addition, in cold cities like Bethel, the excellent heating performance of KC helps M3 have lower LCCP than M1.

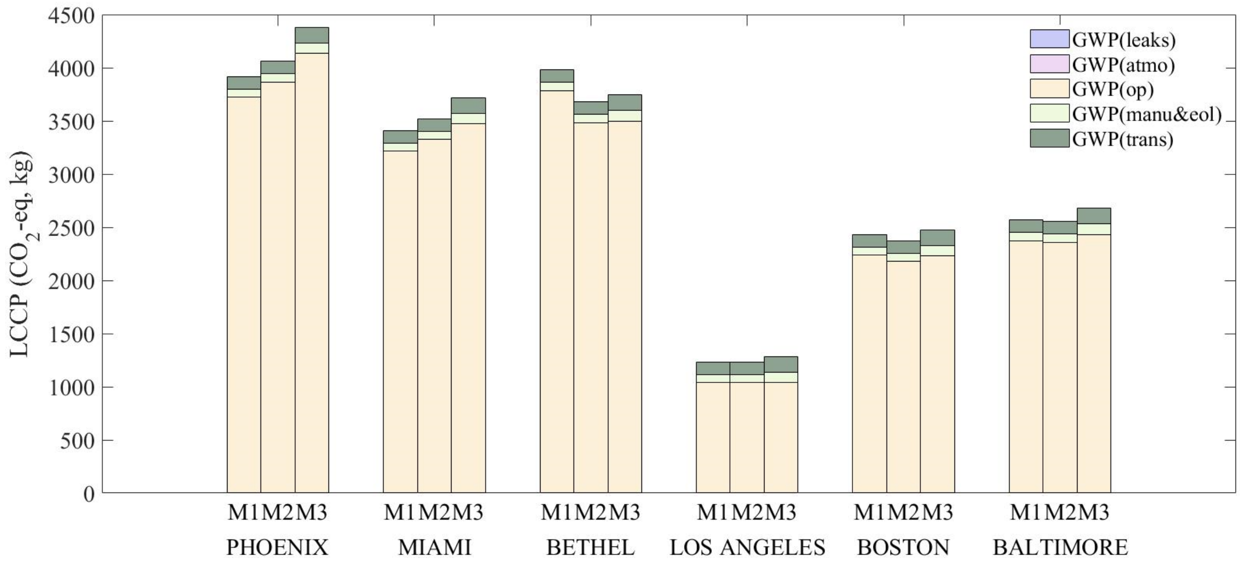

Figure 28: LCCP CO_2-equivalent emission breakdown at various locations

Table 11: Percentage of each temperature bin for selected cities

Temp. bin	PHOENIX	MIAMI	BETHEL	LOS ANGELES	BOSTON	BALTIMORE
>40°C	6%	0%	0%	0%	0%	0%
30°C – 40°C	31%	13%	0%	<0.5%	2%	5%
20°C – 30°C	29%	75%	1%	25%	23%	30%
10°C – 20°C	28%	12%	23%	73%	30%	30%
0°C – 10°C	6%	<0.5%	34%	2%	32%	25%
-10°C – 0°C	0%	0%	21%	0%	12%	9%
-20°C – 10°C	0%	0%	17%	0%	1%	1%
<-20°C	0%	0%	4%	0%	0%	0%

Table 12: Manual controlled system on-time percentage for selected cities

Temp. bin	PHOENIX	MIAMI	BETHEL	LOS ANGELES	BOSTON	BALTIMORE
>40°C	100%	-	-	-	-	-
30°C – 40°C	100%	99%	-	96%	100%	100%
20°C – 30°C	21%	36%	10%	17%	25%	28%
10°C – 20°C	41%	25%	55%	23%	37%	39%
0°C – 10°C	61%	86%	98%	80%	98%	98%
-10°C – 0°C	-	-	100%	-	100%	100%
-20°C – 10°C	-	-	100%	-	100%	100%
<-20°C	-	-	100%	-	-	-

3.12.2 Results using fixed compressor efficiency efficiencies

The choropleth maps of annual operating energy consumption using fixed compressor efficiencies are shown in Figure 29. Because this calculation does not limit the pressure ratio, KC's advantages in cold weather are enlarged. The result indicates that M3 has lower annual energy consumption than FT-VIC in 7 states, all of which are northern states. And M2 has less energy consumption than M1 in 29 states. On average, M1 has annual energy consumption similar to M2, and M3 consumes 3.0% more energy than M1. Note that in this calculation, the cooling and heating capacity under extreme conditions differs between cycles. KC has the highest capacity, followed by FT-VIC.

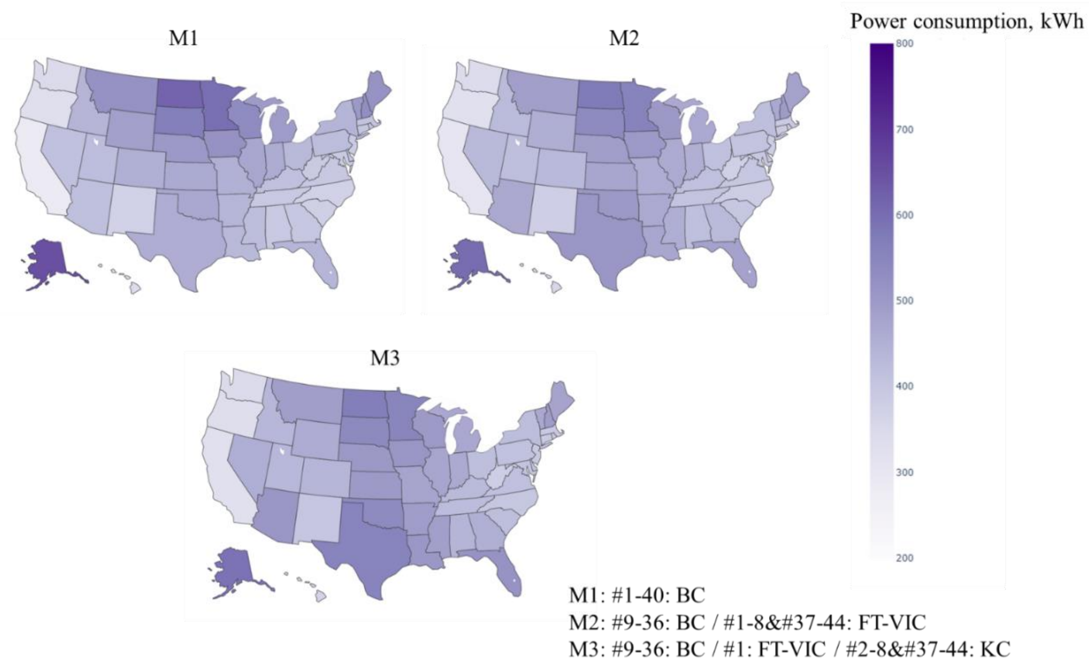

Figure 29: Choropleth maps of annual operating energy consumption (fixed compressor efficiencies)

Figure 30 shows the choropleth maps of LCCP across the U.S. Since the KC has a much larger system weight and refrigerant charge, M3 has a higher LCCP than M2 in every state. And on average the difference is 4.9%. M2 also has lower LCCP than M1 in 29 states, but the difference is minimal on average, which is 0.2%.

Figure 31 shows the breakdown of LCCP at various locations. In Bethel, M3 has the lowest LCCP due to cold weather. However, M3 tends to have the highest LCCP among the three cycles in other cities. Overall, the trend is the same as the case where empirical compressor efficiencies were used.

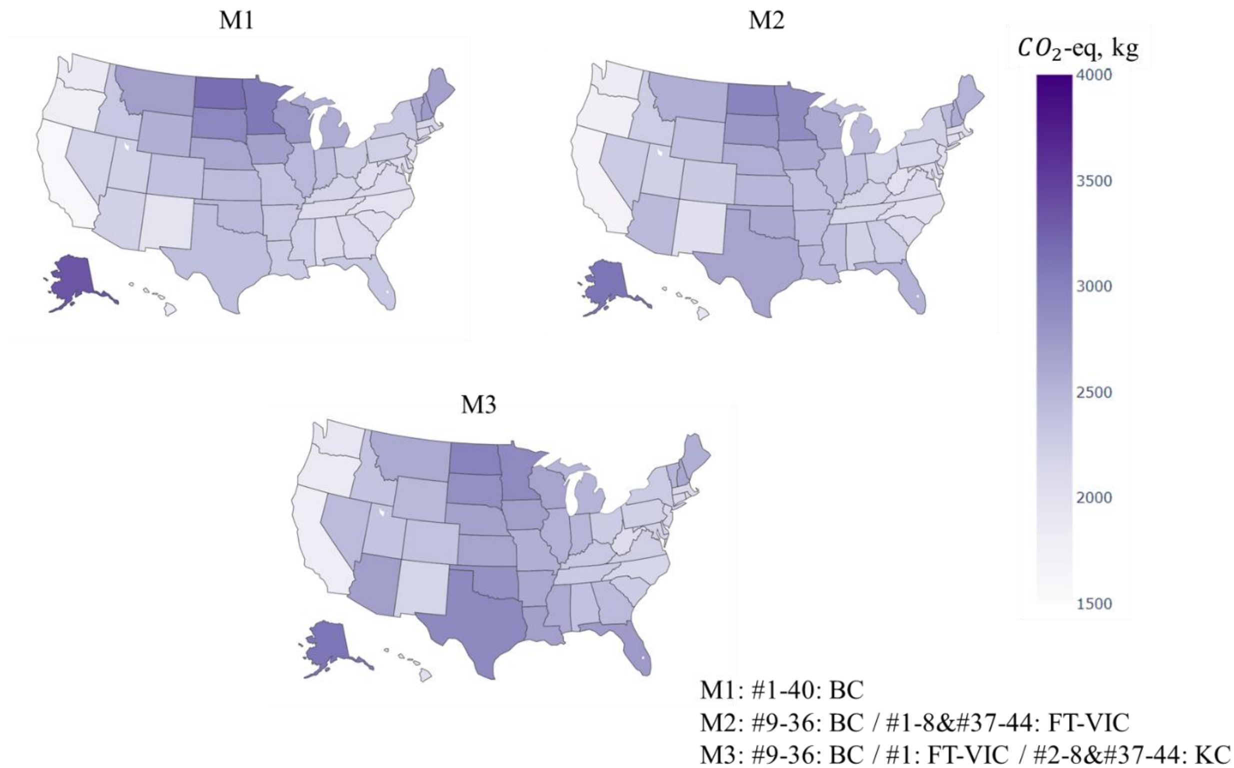

Figure 30: Choropleth maps of LCCP CO_2-equivalent emission (fixed compressor efficiencies)

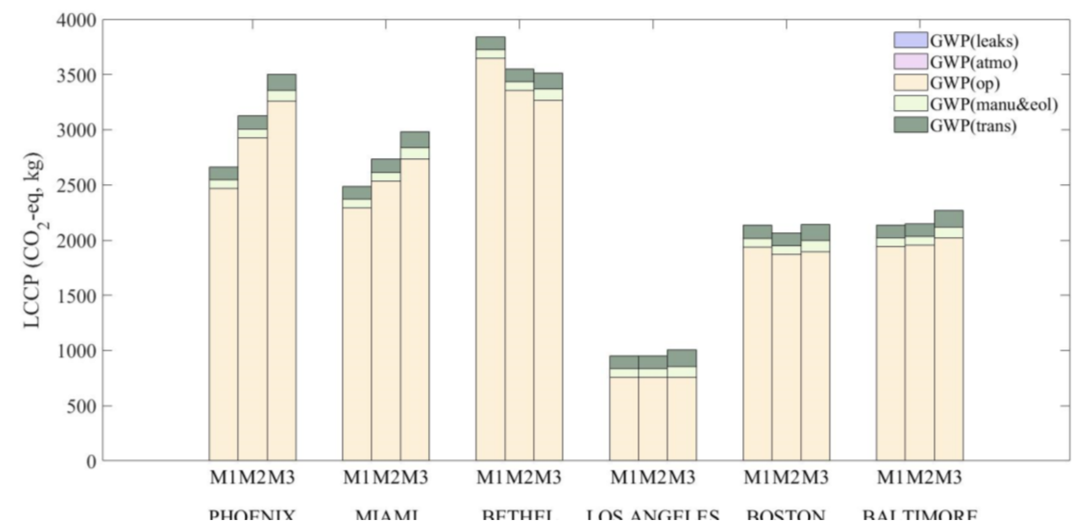

Figure 31: LCCP CO_2-equivalent emission breakdown at various locations (fixed compressor efficiencies)

3.13 Chapter summary and conclusions

In this chapter, thermodynamic models were developed of the basic heat pump cycle (BC), flash tank-based vapor injection heat pump cycle (FT-VIC), and kangaroo heat pump cycle (KC). In those models, heat exchangers were modeled using a fixed approach temperature. And compressor models were efficiency-based semi-empirical models. A simulation matrix derived from SAE standard J2765 was used to calculate cycle performance. The annual energy consumption of each cycle was calculated at every location and recorded in the TMY3 database. And LCCP value was evaluated as well. The summary of simulation results is shown below:

- Effect of KC's sub-cycle compressor speed:
    - When the target cooling or heating capacity is fixed, increasing the sub-cycle compressor speed lowers COP. Therefore, operating a sub-cycle compressor at the minimum speed (3,000 RPM) is the most efficient strategy for the given simulation matrix.
- Heating performance comparison:
    - When the main compressor speed is the same, KC has the highest heating capacity and the lowest COP. When compared to FT-VIC and $T_{amb} = -15°C$, KC on average increases heating capacity and decreases COP by 20.1% and 18.9%, respectively.
- Simulation results based on the simulation matrix (Table 5):
    - Since the primary purpose of FT-VIC and KC is to increase heating capacity, they are only used in extreme conditions. Because the cooling and heating loads are small when T_{amb} is between 25°C and 5°C, BC is used in these conditions. This arrangement results in three operating modes:

    - M1: use BC for all conditions.
    - M2: use BC from simulations #9 to #36 and use FT-VIC for the rest of the conditions.
    - M3: use BC from simulations #9 to #36 and use KC for the rest conditions. Note that in simulation #1 even minimum compressor speed leads to higher than limited discharge pressure and temperature when using empirical compressor efficiencies. As a result, FT-VIC is used in this circumstance.
- Use empirical compressor efficiencies:
    - BC has the highest cooling capacity when T_{amb} = 45°C and V_0 = 1.5 m/s, as the FT-VIC and KC models were limited by the maximum compressor overall pressure ratio.
    - Due to the maximum compressor overall pressure ratio limitation, FT-VIC and KC models show similar cooling capacities in hot weather (simulations #1 to #8). On average, the cooling capacity of KC is 8.8% higher than that of BC. And cooling capacity of FT-VIC is 10.0% higher than that of BC.
    - When T_{amb} = -15°C heating capacity of KC is on average 25.1% and 3.5% higher than that of BC and FT-VIC, respectively. W_{dc} of KC is 14.1% and 3.1% lower than that of BC and FT-VIC, respectively. After factoring in the extra energy consumption due to carrying additional weight, the energy-saving was 13.8% (vs. BC) and 2.7% (vs. FT-VIC).

        - VIC has the highest COP in the most extreme conditions. The only exception is when $T_{amb} = -15°C$, where KC has the highest COP. Under this condition, all cycles failed to reach the target heating capacity. Since the vapor injection compressor pressure ratio does not reach its maximum yet, KC can deliver a higher heating capacity than FT-VIC. And KC has a lower COP than VIC in most cases because the energy saved by reducing the main-cycle compressor speed is less than the additional energy required by the sub-cycle compressor.
    - Use fixed compressor efficiencies:
        - Because the maximum pressure ratio limitation is removed, KC shows the highest cooling capacity in hot weather (simulations #1 to #8). On average, the cooling capacity of KC is 28.1% higher than that of BC. And cooling capacity of FT-VIC is 23.6% higher than that of BC.
        - When T_{amb} = -15°C heating capacity of KC is on average 28.8% and 13.5% higher than that of BC and FT-VIC, respectively.
        - FT-VIC has the highest COP in most hot weather; the COP of KC is 12% and 11% lower than that of the BC and the FT-VIC.
- LCCP:
    - Use empirical compressor efficiencies:
        - For annual energy consumption, M2 has less energy consumption than M3 in every state and has less energy consumption than M1 in 34 states. And M3 has less energy consumption than M1 in 21 states. On average, the

annual energy consumption of M3 is 1.3% higher than that of M1 and 3.0% higher than that of M2.

    - For LCCP, the LCCP of M3 is higher than that of M2 in every state. And LCCP of M3 is lower than that of M1 in 11 states. On average, M3 has a 3.0% higher emission than M1 and 4.6% higher emission than M2, while the emission of M2 is 1.5% lower than that of M1.

- Use fixed compressor efficiencies:
    - For annual energy consumption, M2 has less energy consumption than M3 in 43 states and has less energy consumption than M1 in 29 states. And M3 has less energy consumption than M1 in 22 states. And the states where M3 has less energy consumption than M2 are northern states. On average, the annual energy consumption of M3 is 3.0% higher than that of M1 and M2.
    - For LCCP, because KC has additional system weight, its transportation emission is more significant than other systems. As a result, the LCCP of M3 is higher than that of M2 in every state. And LCCP of M3 is lower than that of M1 in 18 states. And LCCP of M2 is lower than that of M1 in 29 states. On average, the LCCP of M3 is 4.9% higher than that of M2.
- Operating emission is the most significant part of LCCP, followed by transportation emission. And because the GWP of R1234yf is very small, the direct emission can be neglected.

4 Dynamic automobile air conditioning system model and transient simulation

4.1 Dynamic automobile air conditioning system model

Dymola is a commercial software widely used for transient simulation. It is essential for the dynamic modeling of automatic air conditioning systems (MACs) because of their highly transient behavior during driving. The dynamic MACs model was developed in this study based on the CEEE Modelica Library (CML) [67]. System components were modeled individually and could be connected to create cycle models. There are three types of component models: compressor, heat exchanger, and expansion valve. Since the compressor and expansion valve have a relatively small internal volume compared to heat exchangers, they have less thermal inertia than heat exchangers. Also, their response time to input variation is shorter. Therefore, the compressor and the expansion valve were modeled for a quasi-steady-state model. In other words, they share the same governing equations with their steady-state model. The modeling of the heat exchanger is much more complicated, so its details are explained in the following sections.

4.1.1 Modeling approach and validation for the component model

4.1.1.1 Compressor models

In Dymola, compressors were modeled for a quasi-steady-state model. The compressor model comprises two sub-models: a lumped control volume model and a compressor base model.

The compressor base model is the same model used in the thermodynamic model, so is not discussed here for brevity. The lumped control volume is a simplified refrigerant control volume, which sets the number of segments to 1. Details of it are discussed in section 4.1.1.5.1.1.

The lumped control volume added here was used to store the refrigerant and is located between the compressor model inlet ports and the inlet of the base model.

4.1.1.2 Expansion valve model

The expansion valve was modeled as a simple orifice. Its governing equation is as follows.

$$\dot{m} = \frac{u}{u_{max}} C_v D_i^2 \sqrt{\rho_{in} \Delta p} \tag{61}$$

Where u is the input signal indicating the opening of the valve, C_v is the flow coefficient of the valve, D_i is the inner diameter of the valve with maximum opening, ρ_{in} is the inlet refrigerant density, and Δp is the pressure drop across the valve.

When using this model, it is connected to a PID controller, which sends the input signal u based on the monitored result. Typical input signals are compressor suction superheating and discharge superheating.

4.1.1.3 Accumulator, receiver, and flash tank models

In CML, the accumulator and receiver are the same models with different geometry setups. In both models, the refrigerant is assumed to be separated perfectly. In the accumulator, the inlet port has the same height as the outlet port, and they are located near the top of the tank so that the outlet flow is vapor. The outlet port is located at the bottom of the receiver, ensuring the outlet flow is liquid. The accumulator tank itself is modeled as a lump control volume. And its refrigerant quality is also the ratio of liquid level over the tank height. The below equation can calculate the outlet enthalpy of the accumulator and receiver model.

$$h_{out} = \begin{cases} \min\,(h, h_l) & when\ H_{level} > H_o + D_o \\ h_v + \dfrac{H_{level} - H_{out}}{D_o} & when\ H_o + D_o \geq\ H_{level} \geq H_o \\ \max\,(h, h_v) & when\ H_{level} < H_o \end{cases} \tag{62}$$

Where H_{level} is the liquid level inside the accumulator or receiver, H_o is the height of the outlet port, D_o is the outlet port diameter, h_v is dew point enthalpy, and h_l is bubble point enthalpy. This equation indicates that if the outlet flow wants to be subcooled liquid, the tank must be filled with liquid first, and vice versa.

The flash tank model is a specialized accumulator model with one liquid outlet port and one vapor outlet port. In the flash tank model, inlet and outlet port geometry are no longer modeled, and the following equations define the outlet enthalpy of liquid and vapor ports.

$$h_{out,liquid} = \begin{cases} \mathrm{h} & when\ H_{level} > H \\ h_l & when\ H \geq\ H_{level} \geq 0 \\ \mathrm{h} & when\ H_{level} < 0 \end{cases} \tag{63}$$

$$h_{out,vap} = \begin{cases} \mathrm{h} & when\ H_{level} > H \\ h_v & when\ H \geq\ H_{level} \geq 0 \\ \mathrm{h} & when\ H_{level} < 0 \end{cases} \tag{64}$$

Where H is the height of the flash tank.

4.1.1.4 Cabin model

The cabin model was developed based on work from Eisele[68] and Lee et al[69]. Its governing equations are shown below.

$$\begin{aligned} M_r c_{pr} \frac{dT_r}{dt} + M_c c_{pc} \frac{dT_c}{dt} &= \frac{\dot{m}_{in}\left(c_{pa} + C_{pb}\right)}{2}(T_s - T_r) + \dot{Q}_{sol} \\ &+\dot{Q}_{pst} + U_o A_o (T_{amb} - T_r) + \dot{m}_{iv} c_{pamb}(T_{amb} - T_r) \end{aligned} \tag{65}$$

$$M_c c_{pc} \frac{dT_c}{dt} = -htc_c A_c (T_c - T_r) \tag{66}$$

$$M_r \frac{dx_r}{dt} = \left(\dot{m}_{water,s} + \dot{m}_{water,o} + \dot{m}_{water,infil}\right) + \dot{Q}_{plt}/h_{fg} \tag{67}$$

Where equation (65) is the energy balance equation. On the right-hand side, the first term accounts for the cooling or heating load. The second term is the solar radiation load. The third term is the sensible passenger load. The fourth term is the heat transfer between the vehicle surface and ambient air. And the last term is the load related to the leakage of air. Equation (66) accounts for the heat transfer between the cabin compartment and the cabin room air. And equation (67) is the mass balance equation used to calculate the change in cabin relative humidity. The cabin model was validated by using the results from Huang [70], and the validation result is shown in Figure 32.

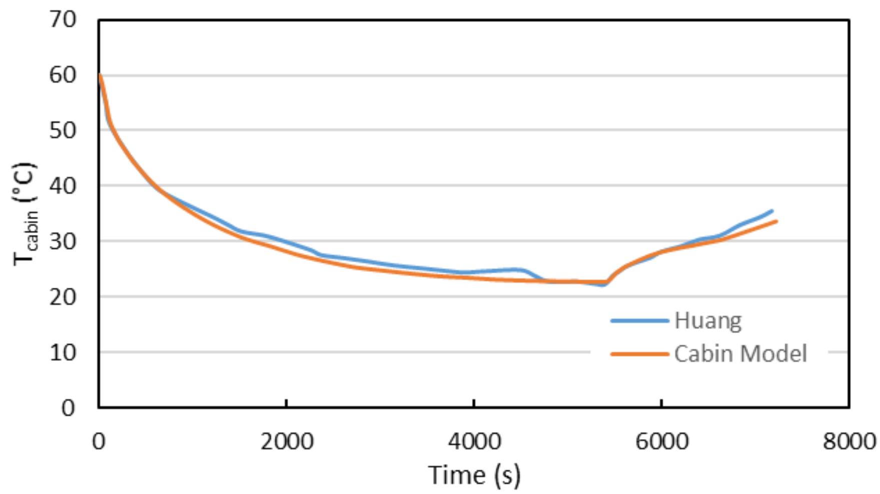

Figure 32: Cabin model validation

4.1.1.5 Heat exchangers

The heat exchanger model is the most complicated in CML. It was modeled based on energy, mass, and momentum conservation. First, a heat exchanger is separated into several control volumes, which are volumes of particular interest. The simplest form of the heat exchanger model has three control volumes: high-temperature side fluid control volume, wall control volume, and low-temperature side fluid control volume. The fluid control volume can be further divided into refrigerant control volume, air control volume, and coolant control volume. Since the fluid properties change a lot inside the heat exchanger and a single segment cannot represent the entire heat exchanger correctly unless it is very short, each control volume is divided into multiple small segments along the flow direction. During simulation, most calculations for the heat exchanger model are performed in each small segment. And those segments are connected through the governing equation. Before explaining the detailed control volumes and heat exchanger model, I want first to explain some error sources that are in general for all heat exchanger models:

- Only one flow passage of each pass is calculated in the heat exchanger model. And this flow passage is used to represent the entire pass. However, in reality, every passage is unique. So, this simplification would bring some errors.
- Another issue with the simplification mentioned above is that it requires the number of channels on both sides of the heat exchanger to be the same. Otherwise, there will be an energy imbalance. For a plate heat exchanger, the number of channels on two sides is often offset by one. In that case, the smaller number is chosen, and the side with more channels gets a correction factor for the heat transfer area to keep the total heat transfer area the same. This approach helps improve the model's accuracy, especially when the number of channels is high.
- Refrigerant maldistribution in microchannel heat exchangers is not considered.
- Other model simplifications, such as evaluating the air-side heat transfer coefficient only once in the inlet, could also contribute to the significant deviation.
- Headers are not modeled. The pressure drop is evenly distributed along the channel when the simulation reaches a steady-state.
- The experimental data may not be 100% accurate. Unfortunately, the uncertainty of experimental data used in this study was not obtainable.

4.1.1.5.1 Control volumes

As mentioned before, heat exchanger models are assembled by individual control volumes. They are explained below:

4.1.1.5.1.1 Refrigerant-side control volume

In the steady-state model, energy flows into the control volume is always equal to energy flows out. However, it is not the same in the transient model. Part of the energy can be stored in or released from the control volume.

The assumptions for the refrigerant-side control volume are:

- The refrigerant flow is a homogeneous flow, which means the vapor velocity is the same as the liquid velocity in the two-phase region. This assumption simplifies the calculation.
- The refrigerant properties inside one segment are uniform.
- No heat loss

The governing equations for the refrigerant-side control volume are:

$$\frac{dU}{dt} = \dot{m}_{in}h_{in} - \dot{m}_{out}h_{out} + \dot{Q} \tag{68}$$

$$\frac{dM}{dt} = \dot{m}_{in} - \dot{m}_{out} \tag{69}$$

Where U is the internal energy, $\dot{Q}$ is the heat flow to the wall, and M is the total mass. Depending on the selection of state variables, there are two methods to calculate the left side of the equation. The first method uses pressure and enthalpy as state variables, and these two variables determine all the other properties. The left side of the equation can then be written as follows:

$$\frac{dU}{dt} = V\left[\left(h\left.\frac{\partial\rho}{\partial p}\right|_h - 1\right)\frac{dp}{dt} + \left(h\left.\frac{\partial\rho}{\partial h}\right|_p + \rho\right)\frac{dh}{dt}\right] \tag{70}$$

$$\frac{dM}{dt} = V\left(\frac{\partial\rho}{\partial h}\bigg|_p \frac{dh}{dt} + \frac{\partial\rho}{\partial p}\bigg|_h \frac{dp}{dt}\right) \tag{71}$$

These equations are the governing equation's standard form and work well in most scenarios. Poor mass conservation is a drawback of using pressure and enthalpy as state variables. Due to the truncation error, the total refrigerant charge in the closed-loop system is not constant but a fluctuating value. And the change in the refrigerant charge is affected by the solver tolerance and simulation steps.

The other method to calculate the governing equations is to use pressure and density as state variables. The equations become:

$$\frac{dU}{dt} = V\left[\left(\rho\frac{\partial h}{\partial p}\bigg|_\rho - 1\right)\frac{dp}{dt} + \left(\rho\frac{\partial h}{\partial \rho}\bigg|_p + h\right)\frac{d\rho}{dt}\right] \tag{72}$$

$$\frac{dM}{dt} = V\left(\frac{d\rho}{dt}\right) \tag{73}$$

And the change of enthalpy can be easily calculated by the equation below

$$\frac{dh}{dt} = \frac{\partial h}{\partial p}\bigg|_\rho \frac{dp}{dt} + \frac{\partial h}{\partial \rho}\bigg|_p \frac{d\rho}{dt} \tag{74}$$

It can then be added as the third state variable. Using pressure and enthalpy, one can calculate all other refrigerant properties. Using this set of governing equations can improve the mass conservation of the model. However, it is less robust and requires a minor time step. And because the density calculation is purely based on its derivative rather than the refrigerant property routine, its derivative must be very accurate to calculate the density correctly.

The aforementioned governing equations are for transient simulation. Setting $\frac{dU}{dt}$ and $\frac{dM}{dt}$ to 0 during the model initialization converts the transient model into a steady-state model. This approach is helpful during the component-level steady-state simulation. In the cycle model, due to nonlinear equations, the model is challenging to solve and often results in simulation failure.

The convective heat transfer from the refrigerant-side to the wall surface can be calculated by using the basic convection equation

$$\dot{Q} = h_{ref} A (T_{wall} - T_{ref}) \tag{75}$$

Where h_{ref} is the refrigerant side heat transfer coefficient, A is the refrigerant side heat transfer area, T_{ref} is the refrigerant temperature and T_{wall} is the wall temperature. h_{ref} can be calculated by empirical correlations. Since h_{ref} is different for each refrigerant phase, other empirical correlations are needed for each refrigerant phase. In the steady-state simulation, one can select which correlation to be used based on the refrigerant phase. In the transient simulation, it is essential to prevent an abrupt change in h_{ref}. The typical approach is to create a smooth transition when phase change happens. This approach requires knowing h_{ref} in all phases and constructing a smooth function between them. Therefore, in this study, h_{ref} of liquid, vapor, and two-phase are calculated simultaneously. And the smooth transition is realized using the "*spliceFunction*" in Modelica.

Empirical correlations are in general accurate. However, they are usually nonlinear and do not have a smooth first-order derivative. This fact can trigger solver chattering or stiff in Dymola, making the model difficult or slow to solve. Therefore, empirical correlations are only used during the component-level simulation in this study. When the heat exchanger model is used in system-level simulation, a simple heat transfer coefficient calculation method is used, where it is assumed that the heat transfer coefficient is purely a function of refrigerant mass flow rate. The below equation can calculate the heat transfer coefficient of each refrigerant phase.

$$h_{ref} = K \left(\frac{\dot{m}}{\dot{m}_0} \right)^n h_0 \tag{76}$$

Where h_0 is the heat transfer coefficient calculated at $\dot{m}_0$. Coefficients K and n are 1 and 2, respectively. This simple model does not require refrigerant properties, and its derivative can be quickly resolved. Therefore, it can significantly speed up the calculation.

Similar to the heat transfer coefficient, the same equation also calculates the refrigerant pressure drop in the heat exchanger.

$$\frac{\Delta p}{\Delta p_0} = K\left(\frac{\dot{m}}{\dot{m}_0}\right)^n \tag{77}$$

Where Δp_0 and $\dot{m}_0$ are the pressure drop and mass flow rate measured in the experiment. Similar to the heat transfer coefficient equation, the default values for K and n are 1 and 2, respectively.

A staggered scheme solves the governing equations inside the refrigerant control volume. The mass and energy conservation equations are solved in one grid, while the pressure drop is calculated in the staggered grid (offset by half the segment length). By doing so, the governing equations are decoupled and become easier to solve.

4.1.1.5.1.2 Air-side control volume

The air-side control volume differs from the refrigerant-side control volume in two aspects. First, the flow direction is different. A typical refrigerant-to-air heat exchanger has a cross-flow configuration, which means that while the refrigerant flows from the pipe inlet to the pipe outlet, the air flows from one side of the pipe to the other. Second, although the dry air doesn't have phase change, the water vapor is condensed during the condensation process in most cases. These differences make air-side control volume unique compared to other flow control volumes.

The assumptions for the air-side control volumes are:

- The air-side mass flow rate is evenly distributed into each small segment.

- The inlet air temperature and humidity ratio calculate the air-side properties, which avoids iteration in the calculation. Since the mass flow rate of each segment is the same, the heat transfer coefficients of each segment are the same and only needed to be evaluated once per timestep.
- There is no pressure drop on the airside. Except when the frost is taken into consideration.

The following governing equations model the air-side control volume:

$$\dot{m}_a c_{p,a} \frac{dT_a}{dy} \Delta y = \alpha_a \left(A_{o,t} + \eta_{fin} A_{o,fin}\right)(T_w - T_a) \tag{78}$$

$$\dot{m}_a \frac{d\omega_a}{dy} \Delta y = \alpha_m \left(A_{o,t} + \eta_{fin} A_{o,fin}\right)(\omega_{w,s} - \omega_a) \tag{79}$$

Where $\alpha_m = \frac{\alpha_a}{c_{p,a} Le^{2/3}}$. The first equation is used to calculate the sensible load, while the second equation is used to calculate the latent load.

In this study, air-to-refrigerant heat exchangers are microchannel heat exchangers using louver fins. The heat transfer area is evaluated by using the below equation

$$\mathrm{A}_{o,t} = 2 \times \left(L_t - t_f \times n_f\right) \times T_d + 2 \times L_t \times T_h \tag{80}$$

$$\mathrm{A}_{o,fin} = \begin{cases} 2 \times (F_l \times F_d) \times n_f \times \left(1 + \frac{1}{nt}\right) & if\ fin\ extended \\ 2 \times (F_l \times F_d) \times n_f \times \left(1 - \frac{1}{nt}\right) & if\ fin\ not\ extended \end{cases} \tag{81}$$

Where L_t is tube length, t_f is fin thickness, n_f is the number of fins, T_d is tube depth, T_h is tube height, F_l is fin length, F_d is fin depth.

The fin efficiency is calculated by the below equation[71]

$$\eta_{\mathrm{fin}} = \frac{\tanh(ml)}{ml} \tag{82}$$

$$m = \sqrt{\frac{2h}{k_f \delta}\left(1 + \frac{\delta}{L_f}\right)} \tag{83}$$

$$l = \frac{b}{2} - \delta \tag{84}$$

Where h is the heat transfer coefficient, k_f is fin conductivity, δ is fin thickness, L_f is fin height, b is the fin height. This study's heat transfer coefficient was calculated using empirical correlations from Chang and Wang [72].

4.1.1.5.1.3 Air-side control volume for frost simulation

A frost formation model is added to the air side model to predict the frost formation on the outside heat exchanger in the heat pump mode. The model mainly follows the work of Qiao [73]. To speed up the calculation, the frost model used in this study is one-dimensional.

The sensible and latent load calculation is similar to the air side control volume. The main difference is that the heat transfer temperature is evaluated based on the frost surface temperature rather than the tube temperature.

$$\dot{m}_a c_{p,a} \frac{dT_a}{dy} \Delta y = \alpha_a \left(A_{o,t} + \eta_{fin} A_{o,fin}\right)\left(T_{fs} - T_a\right) \tag{85}$$

$$\dot{m}_a \frac{d\omega_a}{dy} \Delta y = \alpha_m \left(A_{o,t} + \eta_{fin} A_{o,fin}\right)(\omega_{fs,s} - \omega_a) \tag{86}$$

During the frosting process, the water mass flow rate ($\dot{m}_w$) can be split into two parts: the diffusing mass flow rate ($\dot{m}_\rho$) and condensing mass flow rate ($\dot{m}_\delta$). The former accounts for the water vapor diffusing into the frost layer. While the latter represents the water vapor that builds up the frost thickness.

$$\dot{m}_w = \dot{m}_\rho + \dot{m}_\delta \tag{87}$$

The frost layer is one-dimensional in each segment, and the frost density is assumed to be homogeneous. Therefore, the equations from Breque and Nemer [74] could be used to calculate the frost surface temperature and density change without calculating the temperature profile of the frost layer.

$$T_{fs} = T_{wall} + \frac{\delta_f}{k_{eff}A_o} \times \left(-\dot{Q}_{sen} - \dot{m}_\delta\, L_{sv} + \frac{1}{2}\dot{m}_\rho L_{sv}\right) \tag{88}$$

$$\dot{m}_\rho = \frac{2D_{eff}A_o\rho_{dry,air}}{\delta_f}\left(\omega_{sat}(T_{wall}) - \omega_{sat}\left(T_{surf}\right)\right) \tag{89}$$

Where D_{eff} is the effective diffusion coefficient, which is obtained by multiplying the diffusion coefficient (D_s) with a diffusion resistance factor (μ).

$$D_{eff} = D_s\mu \tag{90}$$

$$D_s = 2.302\left(\frac{P_o}{P}\right)\left(\frac{T}{T_0}\right)^{1.81} \times 10^{-5} \tag{91}$$

This study uses the diffusion factor from Brain et al. [75].

$$\mu = \frac{\epsilon}{\tau} \tag{92}$$

$$\epsilon = 1 - \rho_f/\rho_{ice} \tag{93}$$

$$\tau = \frac{\epsilon}{1-(1-\epsilon)^{0.5}} \tag{94}$$

The effective frost thermal conductivity (k_{eff}) was calculated by using the correlation proposed by Lee et al. [76] (ρ_{fs} < 500 kg/m^3).

$$k_{eff} = 0.132 + 3.13 \times 10^{-4}\rho_{fs} + 1.6 \times 0^{-7}\rho_{fs}^2 \tag{95}$$

The experimental data of Case #1 from Breque and Nemer [77] was used to validate the air side control volume. Similar to their model, a correction factor (Γ) on the air side pressure drop is applied.

$$\Gamma = 72.146 \times \delta_{f*}^2 - 3.0462 \times \delta_{f*} + 0.9622 \tag{96}$$

Where δ_{f^*} is the dimensionless frost thickness, which is defined as $\delta_{f*} = \frac{\delta_f}{F_s/2}$. The coefficients of the above polynomial equation were obtained by matching the simulated pressure drop with the experiment pressure drop.

The validation results are shown in Figure 33 to Figure 35. The model captures the capacity trend. As expected, the pressure drop matches well with the experimental data with the help of the correction factor. And the rate of the frost mass increases matches the experimental data very well.

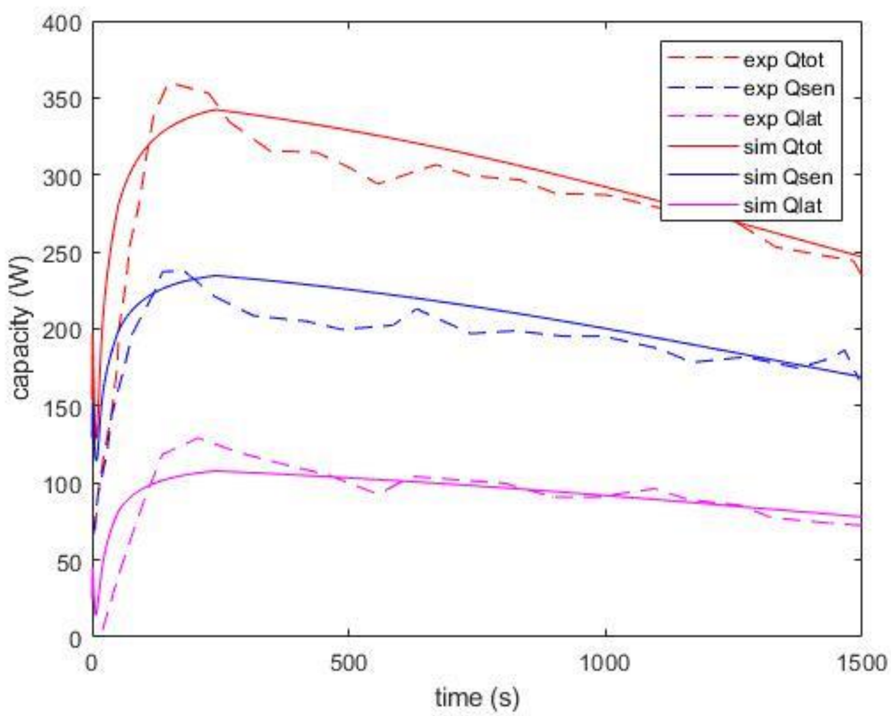

Figure 33: Simulated capacity vs. experiment data

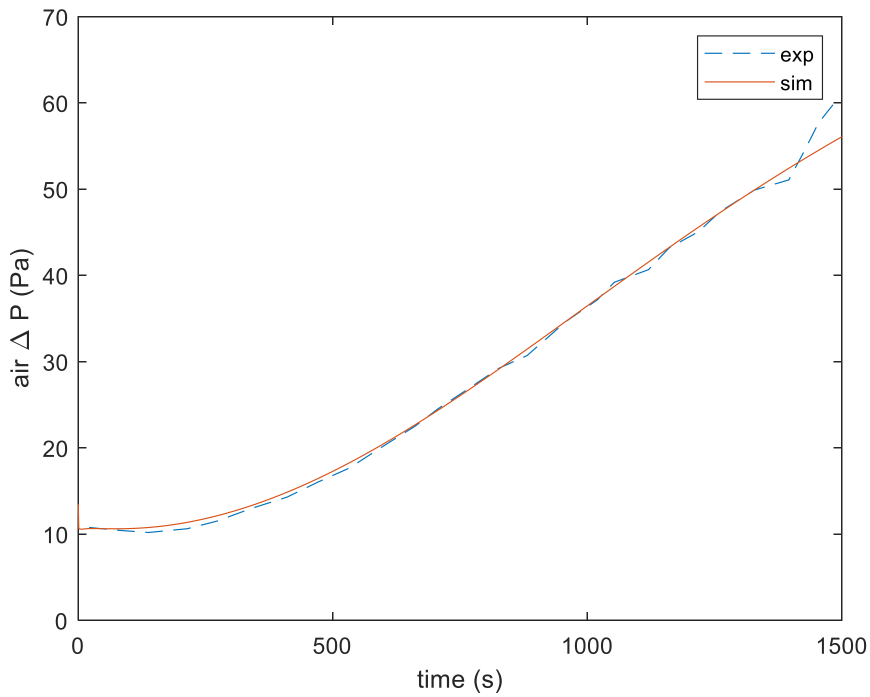

Figure 34: Simulated pressure drop vs. experiment pressure drop

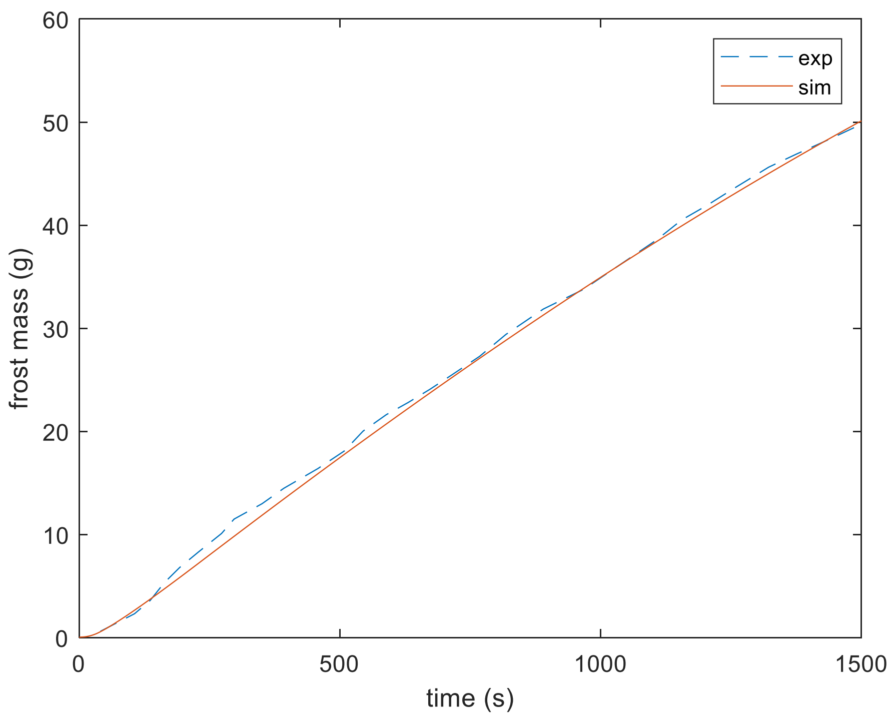

Figure 35: Simulated frost mass vs. experiment frost mass

Because the heat load of each segment is different, the frost growth rate is different too. This result leads to various minimum flow areas and air mass flow rate maldistribution. Since this calculation also involves the fan model, it is discussed in section 4.1.1.6.

4.1.1.5.1.4 Wall control volume

The wall control volume is much simpler, and it has only one governing equation:

$$\dot{Q}_1 + \dot{Q}_2 = C_p m \frac{dT}{dt} \tag{97}$$

Where $\dot{Q}_1$ and $\dot{Q}_2$ are the heat flows from each side of the wall, C_p is the specific heat capacity of the wall, m is the total wall mass, T is temperature, and t is time. As mentioned before, the heat flows are determined inside fluid control volumes. In steady-state, $\dot{Q}_1$ is equal to $\dot{Q}_2$ and $\frac{dT}{dt} = 0$.

4.1.1.5.2 Outdoor heat exchanger model

The outdoor heat exchanger is a microchannel heat exchanger with louver fins. And its face area is 0.14 m^2. The correlations used to solve the heat transfer coefficient on the air and refrigerant side are shown in Table 13. A 1.5 correction factor was applied to both sides to improve the model's accuracy. As mentioned, the empirical correlation makes the model slow and challenging to use in the cycle models. Thus, the simple heat transfer coefficient is also applied. In addition, the pressure drop was calculated based on a regression model. Figure 36 and Figure 37 show the validation results of capacity and pressure drop, respectively. During the tests, the outdoor heat exchanger serves as a condenser. The maximum deviation of heating capacity is 15%. The simple h_{ref} model can capture the trend and has a slightly larger discrepancy than the empirical correlations. As for the pressure drop, because the model was fitted based on the experiment data, its deviation is less than 4%.

Table 13: Correlations for outdoor heat exchanger model

Location	Variable	Calculation method	Correction factor

Air-side	Heat transfer coefficient	Chang Wang Louver HTC	1.5
Refrigerant-side	Single-phase HTC	Gnielinski for turbulence flow, fixed Nu for laminar flow	1.5
	Two-phase HTC	Shah Cond 2016 Shah Evap 2016 [78]	
	Pressure drop	Normalized pressure drop (fitting)	-

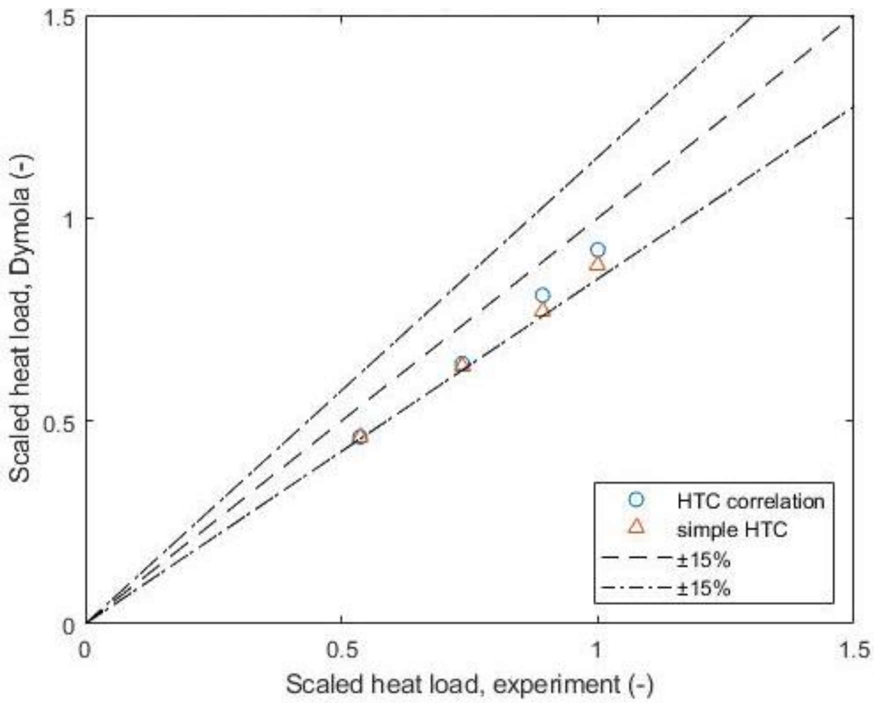

Figure 36: Outdoor heat exchanger capacity validation (non-dimensionalized, original unit: W)

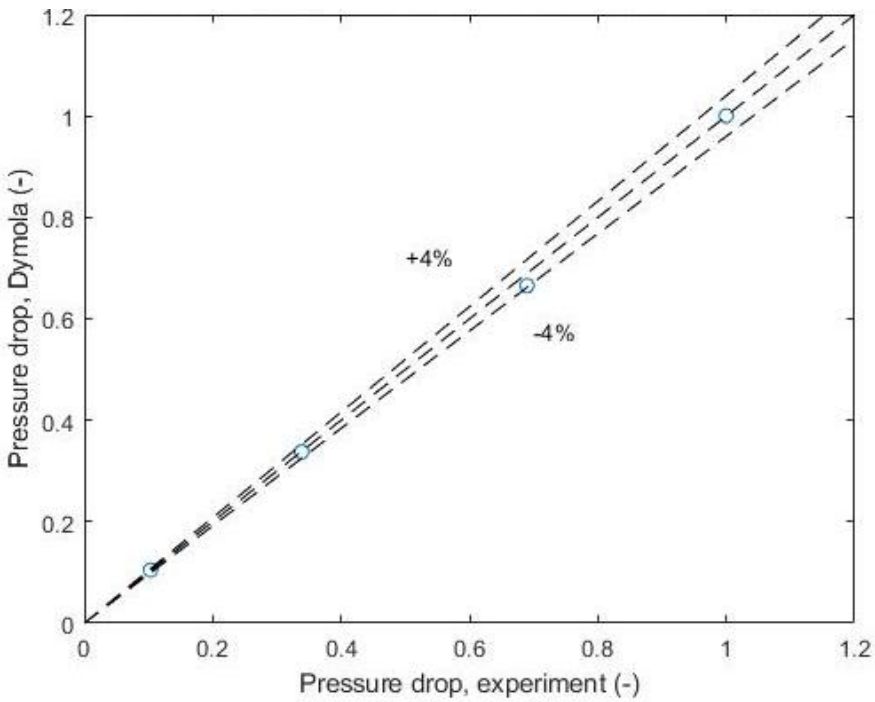

Figure 37: Outdoor heat exchanger pressure drop validation (non-dimensionalized, original unit: kPa)

4.1.1.5.3 Indoor heat exchanger model

The indoor heat exchanger is a microchannel heat exchanger with a louver fin. And its face area is 0.14 m^2. It uses the same heat transfer coefficient correlations and correction factor as shown in Table 13. During the test, the indoor heat exchanger served as an evaporator. Figure 38 shows the validation results of cooling capacity. When using empirical heat transfer coefficient correlation, its maximum deviation is less than 9%. And when using the simple heat transfer coefficient model, the maximum deviation is less than 8%. And Figure 39 shows the maximum deviation of pressure drop, which is less than 1%. Overall, the simple heat transfer coefficient and pressure drop model work well.

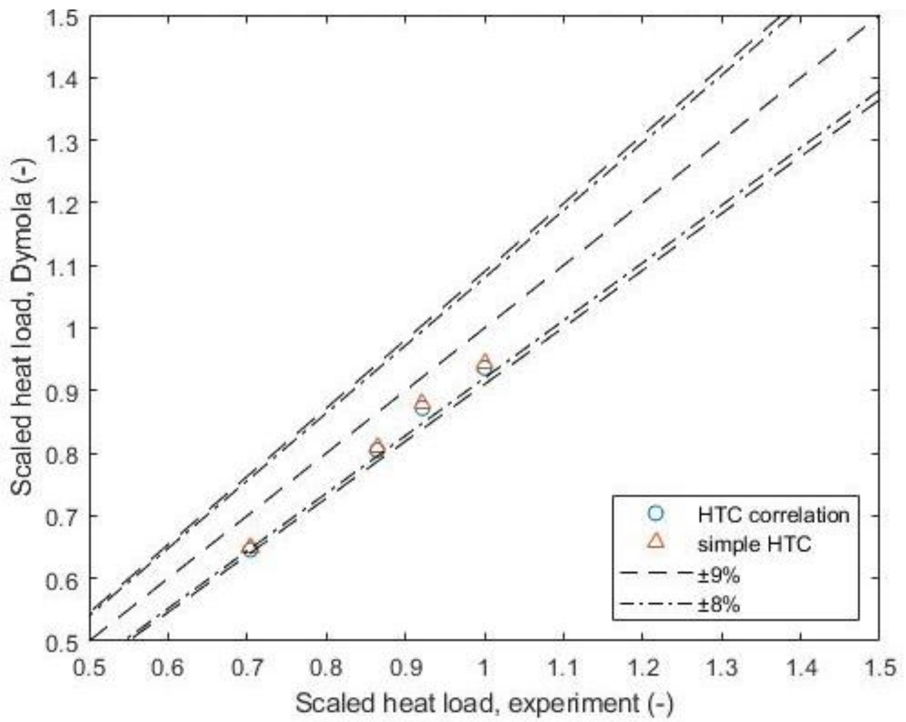

Figure 38: Indoor heat exchanger capacity validation (non-dimensionalized, original unit: W)

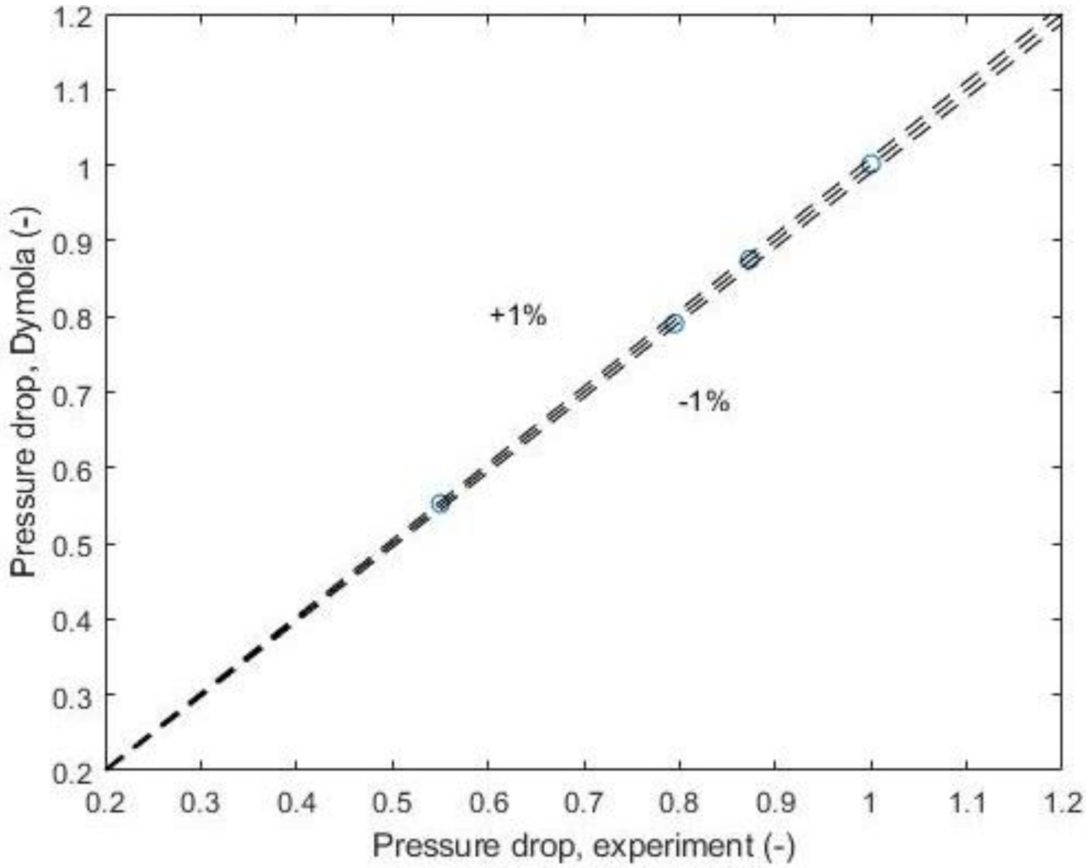

Figure 39: Outdoor heat exchanger pressure drop validation (non-dimensionalized, original unit: kPa)

4.1.1.6 Fan model and air maldistribution calculation

The fan model is a quasi-steady state model. The most important part of the fan model is its fan curve, which calculates the air side pressure rise as a function of the air volume flow rate. A second-order polynomial equation was used to generate the fan curve.

$$\Delta P_{\mathrm{fan}} = a_0 + a_1 \times CFM + a_2 \times CFM^2 + a_3 \times CFM^3 \tag{98}$$

Where ΔP_{fan} is the pressure change of the fan, a is the coefficients, and CFM stands for cubic feet per minute. The data from SPAL VA10-AP70/LL-61 [79] was used to create the fitting. The coefficients are shown in Table 14, and the fitting is plotted in Figure 40. The R^2 of the fitting is 0.993.

Table 14: Outdoor fan curve coefficients

Parameter	Value	Unit
a_0	-2.51e-7	Pa
a_1	4.661e-4	Pa/CFM
a_2	-0.407	Pa/CFM^2
a_3	283.4	Pa/CFM^3

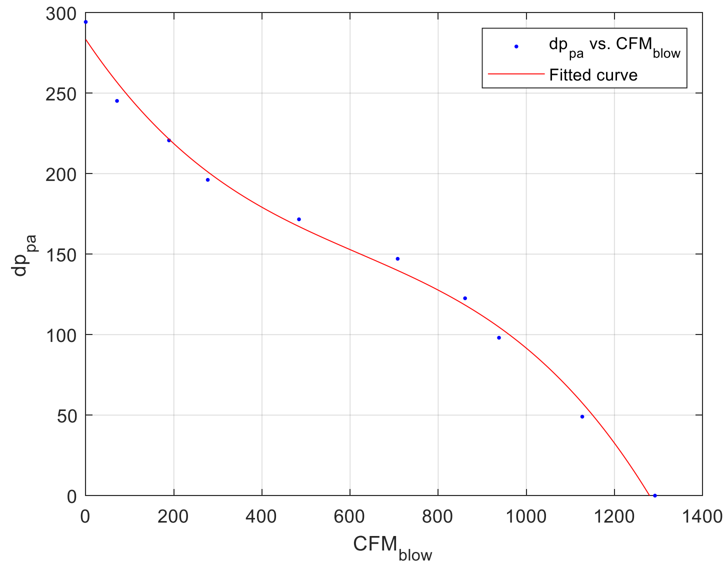

Figure 40: Fan curve fitting results

Typically, the air mass flow rate is given to the model instead of calculating it using a fan model. Depending on the simulation boundary, it can be a constant or a variable that changes over time. However, when frost happens, things become much more complicated. As the frost grows, the minimum airflow area keeps decreasing. The frost growth rate depends on the situation and is impossible to predict. Because of this, the air mass flow rate can no longer be a direct input. Instead, a fan model is needed to calculate the air mass flow rate accurately.

In the vehicle, the air stream passes through the frontal grill, radiator, and condenser. When the vehicle is stationary, the sum of the pressure drop across the frontal grill, radiator, and condenser should equal the pressure rising across the fan. And when the vehicle is moving, the air rammed on the grill causes the air pressure to rise, which is referred to as "ram air". This ram air allows more air to pass through the aforementioned heat exchanger and improves its performance. According to Ap et al. [80], the air side pressure drop passing through the cooling compartment can be calculated by

$$\Delta P_{\text{fan}} = \Delta P_{grill} + \Delta P_{cond} + \Delta P_{radiator} - \Delta P_{ram} \tag{99}$$

Where

$$\Delta P_{grill} = \frac{1}{2}\rho_{air} C_{p,grill} V_{grill}^{2} \tag{100}$$

$$\Delta P_{ram} = \frac{1}{2}\rho_{air} C_{p,ram} V_{car}^{2} \tag{101}$$

And $C_{p,grill}$ = 2.0 and $C_{p,ram}$ = 0.7. In this study, the grill is not considered and the radiator is not presented. Thus, ΔP_{grill} and $\Delta P_{radiator}$ are removed from the equation.

The heat exchanger's air side pressure drop is calculated by using the empirical correlation from Kim and Bullard [81] for louver fins.

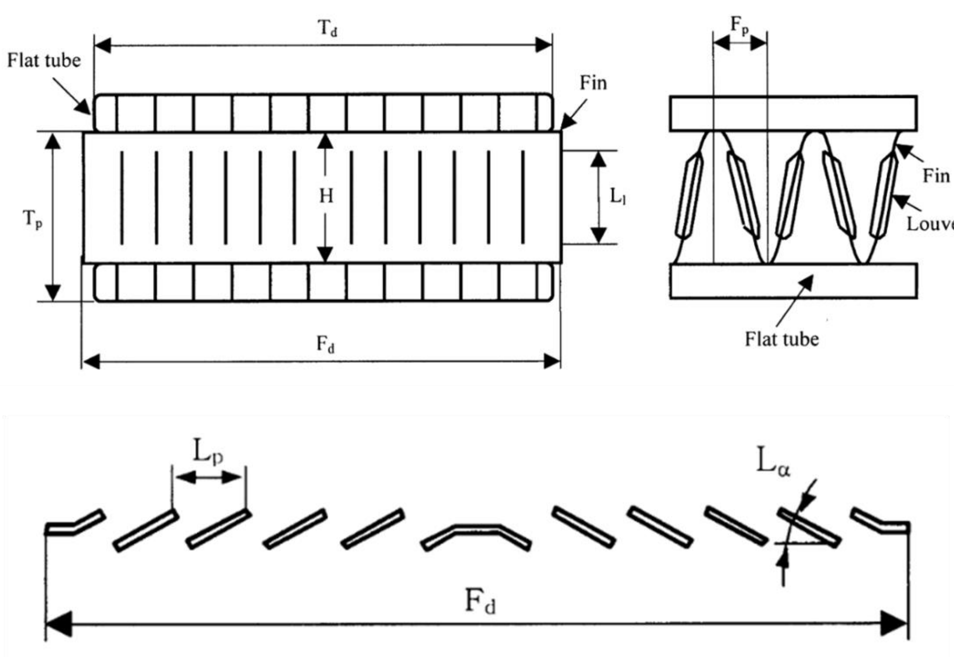

Figure 41: Louver fin geometry [81]

$$f = \mathrm{Re}_{\mathrm{Lp}}^{-0.781} \left(\frac{L_\alpha}{90}\right)^{0.444} \left(\frac{F_p}{L_P}\right)^{-1.682} \left(\frac{H}{L_p}\right)^{-1.22} \left(\frac{F_d}{L_p}\right)^{0.818} \left(\frac{L_l}{L_p}\right)^{1.97} \tag{102}$$

where f is the fanning friction factor. And the definition of the geometry parameters can be found in Figure 41.

As mentioned before, because the air side control volume is a segment-by-segment model, the cooling load of each segment is different depending on the refrigerant side state. As a result, the frost growth rate of each segment varies. This leads to air mass flow rate maldistribution.

To efficiently calculate the air mass flow rate maldistribution, the approach proposed by Qiao et al. [73] was used. On top of the original equation, additional terms that factor in the ram air effect were added to the calculation. The below section explains it in more detail.

Based on the mass conservation inside the fan, we can get

$$\sum \Delta \dot{m}_i = \rho_{fan} \Delta \dot{V}_{fan} \tag{103}$$

where *i* is the segment index.

Then, the change of pressure at each time step can be approximated by the below equations

$$\Delta P_i(\dot{m}_i + \Delta \dot{m}_i) \approx \Delta P_i(\dot{m}_i) + \left.\frac{\partial(\Delta P_i)}{\partial \dot{m}_i}\right|_{\dot{m}_i} \Delta \dot{m}_i \tag{104}$$

$$\Delta P_{fan}\left(\dot{V}_{fan} + \Delta \dot{V}_{fan}\right) \approx \Delta P_{fan}\left(\dot{V}_{fan}\right) + \left.\frac{\partial\left(\Delta P_{fan}\right)}{\partial \dot{V}_{fan}}\right|_{\dot{V}_{fan}} \Delta \dot{V}_{fan} \tag{105}$$

$$\Delta P_{ram}\left(\dot{U}_{car} + \Delta \dot{U}_{car}\right) \approx \Delta P_{ram}\left(\dot{U}_{car}\right) + \left.\frac{\partial(\Delta P_{ram})}{\partial \dot{U}_{car}}\right|_{\dot{U}_{car}} \Delta \dot{U}_{car} \tag{106}$$

Where ΔP_i is the pressure drop of each heat exchanger segment, ΔP_{ram} is the pressure change caused by the ram air. $\left.\frac{\partial(\Delta P_i)}{\partial \dot{m}_i}\right|_{\dot{m}_i}$ is the derivative of air side pressure drop with respect to the air side mass flow rate and evaluated at $\dot{m}_i$, $\left.\frac{\partial(\Delta P_{fan})}{\partial \dot{V}_{fan}}\right|_{\dot{V}_{fan}}$ is the derivative of fan pressure change with respect to the fan volume flow rate and evaluated at $\dot{V}_{fan}$, and $\left.\frac{\partial(\Delta P_{ram})}{\partial \dot{U}_{car}}\right|_{\dot{U}_{car}}$ is the derivative of ram air pressure change with respect to the vehicle speed and evaluated at $\dot{U}_{car}$.

Though the air mass flow rate in each segment is different, the air side pressure drop across the heat exchanger should be the same for each segment, which leads to the below equation:

$$\Delta P_i - \Delta P_{ram} = \Delta P_{fan} \tag{107}$$

Substitute the previous pressure drop equations back into equation (107), one can get

$$\begin{gathered}\Delta P_i(\dot{m}_i) + \left.\frac{\partial(\Delta P_i)}{\partial \dot{m}_i}\right|_{\dot{m}_i} \Delta\dot{m}_i = [\Delta P_{fan}(\dot{V}_{fan}) + \left.\frac{\partial(\Delta P_{fan})}{\partial \dot{V}_{fan}}\right|_{\dot{V}_{fan}} \Delta\dot{V}_{fan}] + \\ \Delta P_{ram}(\dot{U}_{car}) + \left.\frac{\partial(\Delta P_{ram})}{\partial \dot{U}_{car}}\right|_{\dot{U}_{car}} \Delta\dot{U}_{car}\end{gathered} \tag{108}$$

The equation to calculate the change of mass flow rate can be obtained by rearranging the above equation.

$$\begin{aligned}\Delta\dot{m}_i = & \frac{\Delta P_{fan}(\dot{V}_{fan}) + \left.\frac{\partial(\Delta P_{fan})}{\partial \dot{V}_{fan}}\right|_{\dot{V}_{fan}} \Delta\dot{V}_{fan}}{\left.\frac{\partial(\Delta P_i)}{\partial \dot{m}_i}\right|_{\dot{m}_i}} \\ & + \frac{\Delta P_{ram}(\dot{U}_{car}) + \left.\frac{\partial(\Delta P_{ram})}{\partial \dot{U}_{car}}\right|_{\dot{U}_{car}} \Delta\dot{U}_{car} - \Delta P_i(\dot{m}_i)}{\left.\frac{\partial(\Delta P_i)}{\partial \dot{m}_i}\right|_{\dot{m}_i}}\end{aligned} \tag{109}$$

Substitute equation (109) into equation (103), and rearrange terms by separating ΔP and derivatives. One can get below equation

$$\sum\left[\frac{\Delta P_{fan}(\dot{V}_{fan})+\Delta P_{ram}(\dot{U}_{car})-\Delta P_i(\dot{m}_i)}{\left.\frac{\partial(\Delta P_i)}{\partial \dot{m}_i}\right|_{\dot{m}_i}}+\frac{\left.\frac{\partial(\Delta P_{ram})}{\partial \dot{U}_{car}}\right|_{\dot{U}_{car}}\Delta\dot{U}_{car}}{\left.\frac{\partial(\Delta P_i)}{\partial \dot{m}_i}\right|_{\dot{m}_i}}\right.$$

$$\left.+\frac{\left.\frac{\partial(\Delta P_{fan})}{\partial \dot{V}_{fan}}\right|_{\dot{V}_{fan}}\Delta\dot{V}_{fan}}{\left.\frac{\partial(\Delta P_i)}{\partial \dot{m}_i}\right|_{\dot{m}_i}}\right]=\rho_{fan}\Delta\dot{V}_{fan} \tag{110}$$

Then, rearrange terms in the equation to put $\Delta\dot{V}_{fan}$ on one side

$$\Delta\dot{V}_{fan}\left\{\left.\frac{\partial(\Delta P_{fan})}{\partial \dot{V}_{fan}}\right|_{\dot{V}_{fan}}\left[\sum\frac{1}{\left.\frac{\partial(\Delta P_i)}{\partial \dot{m}_i}\right|_{\dot{m}_i}}\right]-\rho_{fan}\right\}$$

$$=\sum\frac{\Delta P_i(\dot{m}_i)}{\left.\frac{\partial(\Delta P_i)}{\partial \dot{m}_i}\right|_{\dot{m}_i}}-\Delta P_{fan}(\dot{V}_{fan})\sum\frac{1}{\left.\frac{\partial(\Delta P_i)}{\partial \dot{m}_i}\right|_{\dot{m}_i}} \tag{111}$$

$$-\Delta P_{ram}(\dot{U}_{car})\sum\frac{1}{\left.\frac{\partial(\Delta P_i)}{\partial \dot{m}_i}\right|_{\dot{m}_i}}-\sum\frac{\left.\frac{\partial(\Delta P_{ram})}{\partial \dot{U}_{car}}\right|_{\dot{U}_{car}}\Delta\dot{U}_{car}}{\left.\frac{\partial(\Delta P_i)}{\partial \dot{m}_i}\right|_{\dot{m}_i}}$$

To simplify the equation, define $\kappa=\sum\frac{1}{\left.\frac{\partial(\Delta P_i)}{\partial \dot{m}_i}\right|_{\dot{m}_i}}$, $\psi=\sum\frac{\Delta P_i(\dot{m}_i)}{\left.\frac{\partial(\Delta P_i)}{\partial \dot{m}_i}\right|_{\dot{m}_i}}$,$\phi=\left.\frac{\partial(\Delta P_{ram})}{\partial \dot{U}_{car}}\right|_{\dot{U}_{car}}\Delta\dot{U}_{car}$.

$$\Delta\dot{V}_{fan}=\frac{\psi-\left[\Delta P_{fan}(\dot{V}_{fan})+\Delta P_{ram}(\dot{U}_{car})+\phi\right]\kappa}{\left.\frac{\partial(\Delta P_{fan})}{\partial \dot{V}_{fan}}\right|_{\dot{V}_{fan}}\kappa-\rho_{fan}} \tag{112}$$

Once $\Delta\dot{V}_{fan}$ is calculated, its value can be used in equation (112) to calculate the air mass flow rate of each segment.

4.1.1.7 Lookup table for density

A significant calculation time was spent on thermodynamic properties calls when doing transient simulation. Replacing the Helmholtz model with a look-up table could significantly reduce the calculation time. For example, Modelon's Splined-Based-Table-Lookup (SBTL) model reports a 33% shorter calculation time when compared to the short Helmholtz model and has good accuracy [82].

In this model, most thermodynamic properties were calculated by Xprops [83]. When the refrigerant state inside the control volume passes through the saturation liquid line, the density partial derivative changes dramatically and the model is prone to have convergence problem, or simulation stiff. Because the function call was implemented in the form of external functions without derivative, the Dymola solver needed to calculate its derivative numerically and the model could be prolonged when phase change happened. To resolve this issue, a lookup table was adopted in the model to calculate the R1234yf's density and its derivative.

The R1234yf density data was generated from Refprop 9.1 [84]. The state variables were pressure and specific enthalpy. And density was calculated in a 100×100 mesh grid. The results were then imported into Dymola. The Modelica standard library CombiTable2D was used to create the lookup table. The interpolation method was Akima spline interpolation, which guaranteed a continuous first derivative. This approach allowed the solver to find the first derivative quickly and run the calculation smoothly.

Initially, the mesh grid was generated with equal spacing on both axes. The specific enthalpy ranges from 150 kJ/kg to 500 kJ/kg. And the pressure ranges from 32.5 kPa to 3,381.2 kPa. In addition to the fitting data, validation data was generated from a shifted mesh grid, where specific enthalpy and pressure were shifted by 5 kJ/kg and 0.5 kPa, respectively.

The results were then compared to the Refprop data. It was found that when the grid size was 100×100 and had equal spacing, though the average absolute error in density was 8.3%, the maximum error could be as high as 70%. The place with the highest absolute error happened near the saturation liquid line. One way to increase the accuracy in this region was to add more sample points in this region by transforming the grid.

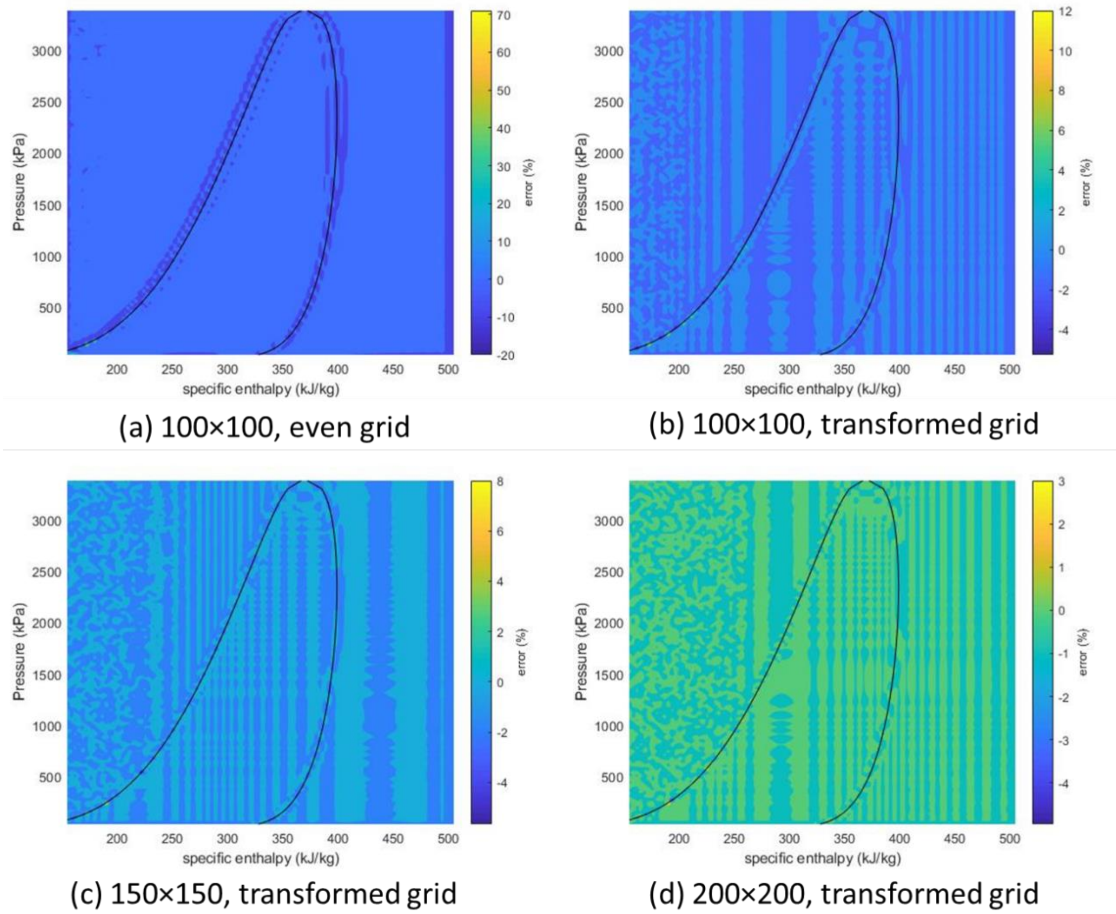

Figure 42: R1234yf density lookup table error (%) in P-h diagram

To transform the grid, an equidistance grid was first generated in the log10 space. Then the generated grid was transformed back into normal space. In that way, more data points were sampled in low-pressure and low-specific-enthalpy regions, as shown in Figure 43.

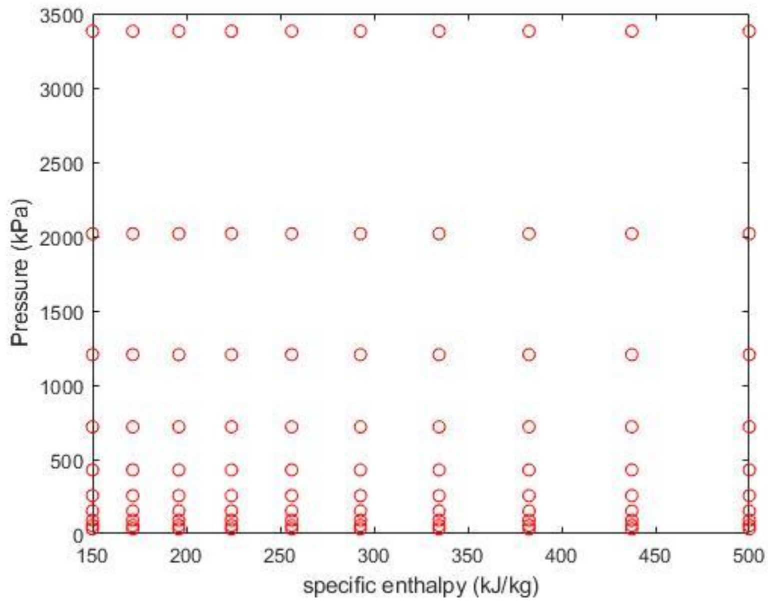

Figure 43: Grid example after transformation (10×10)

After grid transformation, the new lookup table has much better accuracy. The average and maximum absolute errors were 3.2% and 13.4%. To further improve the lookup table, more sample points were added. When the grid size was 150×150, the average and maximum absolute errors were 1.4% and 8.8%. And when the grid size was 200×200, the average and maximum absolute errors were 0.8% and 5.0%. Increasing the grid size further could exceed the array length limits. Therefore, the 200×200 grid was used in this study.

4.1.2 Cycle models

Once component models were developed and validated, they were used to build cycle models. Methods were applied to simplified models and speed up calculation:

- The expansion valve's arrangement is modified. In schematics, cooling and heating mode uses different valves, and a check valve bypasses the unused valve. However, modeling these details increases the complexity of the model and does not affect the actual system performance much. Therefore, only used expansion valves are included in the cycle model.

- Pipes are not included, which helps reduce the complexity of the model.
- Accumulator is removed from the model.
- Only the heating mode is modeled, and no mode switch is considered. Therefore, four-way valves are not included in the model.

Figure 44, Figure 45, and Figure 46 show the diagrams of the BC, FT-VIC, and KC models, respectively. Valves are controlled by PID controllers, whose signal comes from the sensor module. For the BC model, PID is controlled by the evaporator (outdoor heat exchanger in the heating mode) superheating. For the FT-VIC model, the evaporator superheating also controls the low-stage valve. The high-stage valve is more complicated. In practice, it can be controlled by the liquid level inside the flash tank. Or, if an economizer is added, it can also be controlled by a TXV. In this model, the high-stage valve is controlled by the condenser (indoor heat exchanger in the heating mode) subcooling. In addition, a simple PID control is added to control the main compressor's speed, with a cap of 8,600 RPM. And the input signal to the PID control is the difference between the cabin room temperature and the target cabin room temperature.

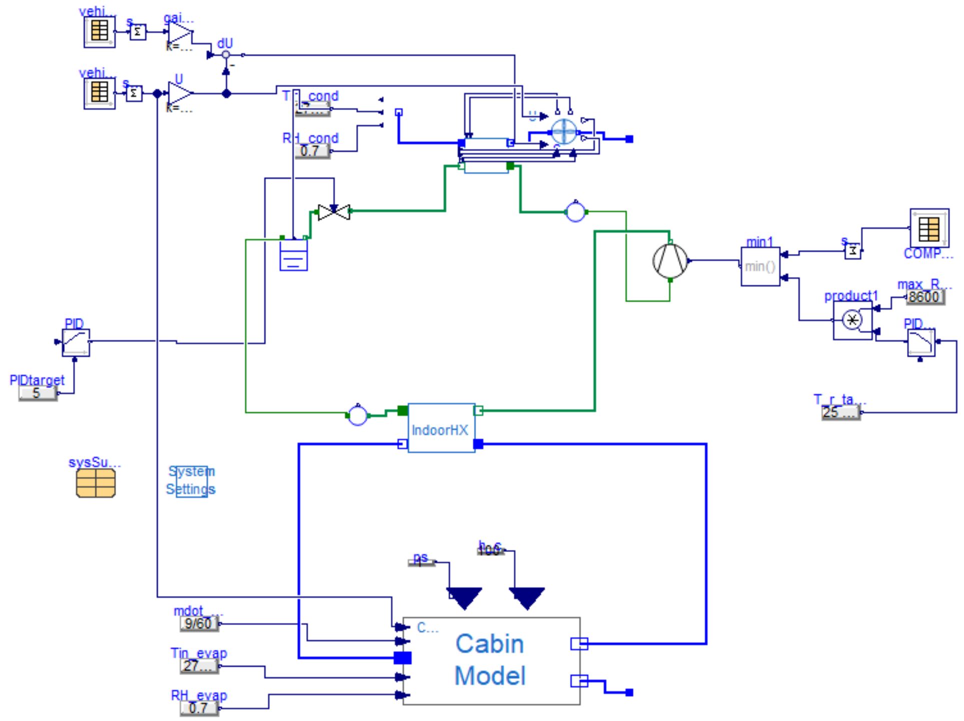

Figure 44: Diagram of BC model

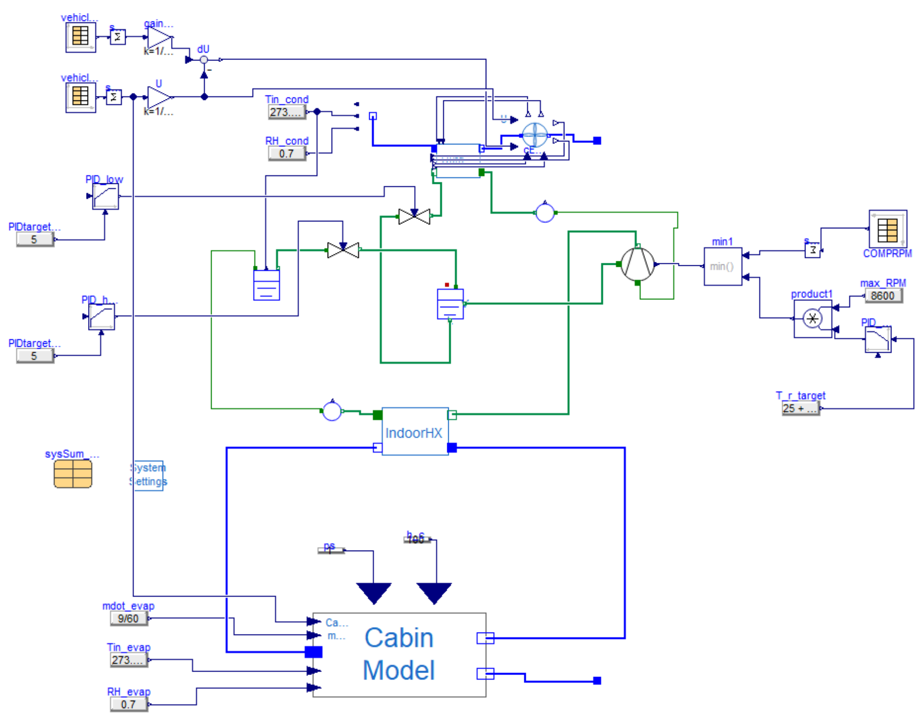

Figure 45: Diagram of FT-VIC model

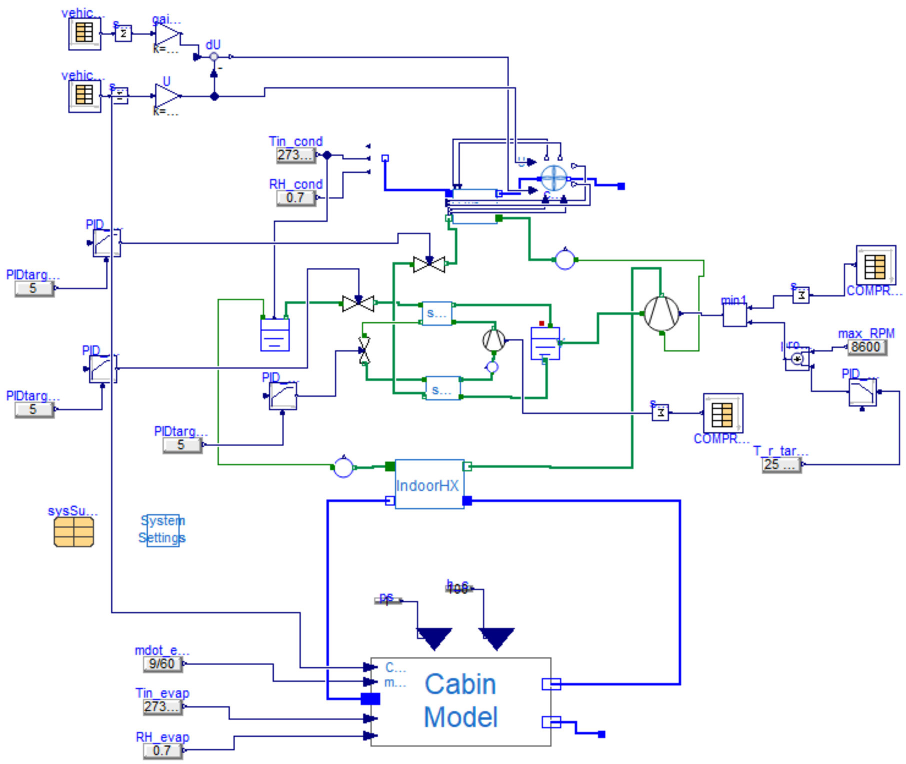

Figure 46: Diagram of KC model

4.2 Sub-cycle heat exchangers' design

4.2.1 Boundary conditions

To design the sub-cycle heat exchangers, it is necessary to calculate the appropriate design boundaries, including the inlet refrigerant pressure, specific enthalpy, and target capacity. This calculation can be done by using the KC thermodynamic model mentioned in the previous chapter. To increase the accuracy of the thermodynamic model, Dymola simulations of FT-VIC were first performed to correct the heat exchangers' approach temperature.

For the Dymola FT-VIC model, simulations were performed for T_{amb} = -15°C cases, which are simulations #41 to #44 from the simulation matrix. And instead of controlling the condenser outlet air temperature, the compressor speed is fixed at 5,000 RPM. And simulated time is 600 seconds, sufficient for the model to reach a steady state in all scenarios.

The simulation results are shown in Table 15. When the outdoor heat exchanger's air velocity increases, its air-side heat transfer coefficient, and air mass flow rate increase, which leads to a higher heating capacity.

Table 15: Simulation results of FT-VIC Dymola model

Parameter	Unit	Case 1	Case 2	Case 3	Case 4	Case 5
T	°C	-15	-15	-15	-15	-15
V_{oHX}	m/s	1.5	2	3	4	3
$\dot{m}_{air,i}$	kg/s	9	9	9	9	9
Comp. speed	RPM	5,000	5,000	5,000	5,000	8,600
Q_{oHX}	W	2,415	2,553	2,704	2,777	3,708
Q_{iHX}	W	3,033	3,191	3,364	3,450	4,805
W	W	671	695	721	734	1,573
COP	-	4.5	4.6	4.7	4.7	2.4
P_{suc}	kPa	110	117	125	129	102
P_{dis}	kPa	391	406	422	430	577
T_{suc}	°C	-20.6	-19.1	-17.5	-16.7	-20
T_{dis}	°C	31.3	31.7	32.3	32.6	38.1
$\dot{m}_{dis}$	kg/s	0.015	0.016	0.017	0.018	0.026
$T_{sup,oHX}$	K	5	5	5	5	5
Ref. charge	kg	0.74	0.74	0.74	0.74	0.74
$T_{oHX,in}$	°C	-20.2	-18.7	-17.1	-16.3	-19.2
$T_{oHX,out}$	°C	-25.4	-23.8	-22.1	-21.3	-24.2
$T_{iHX,in}$	°C	-4.4	-3.3	-2.2	-1.6	7.5
$T_{iHX,out}$	°C	20.7	21.4	22.3	22.7	29.5
$P_{oHX,in}$	kPa	121	129	139	143	127
$P_{oHX,out}$	kPa	121	129	139	143	127
$P_{iHX,in}$	kPa	380	394	408	416	550
$P_{iHX,out}$	kPa	391	406	422	430	577
P_{inj}	kPa	195	207	219	226	202
$\dot{m}_{suc}$	kg/s	0.0144	0.0153	0.0163	0.0168	0.0222
$\dot{m}_{inj}$	kg/s	0.001	0.001	0.001	0.001	0.0038
$T_{air,oHX,out}$	°C	-23.3	-21.6	-19.6	-18.6	-21.4
$T_{air,iHX,out}$	°C	5.2	6.2	7.3	7.9	16.9
$T_{sub,iHX}$	K	10	10	10	10	10
AT_{oHX}	K	2.1	2.2	2.4	2.7	2.9
AT_{iHX}	K	1.3	1.4	1.5	1.5	2.2

And since the increase of heating capacity is faster than the increase of compressor power, COP increases as the outdoor heat exchanger's air velocity increases, which is the same trend that was observed in the thermodynamic model.

The average approach temperature of the indoor and outdoor heat exchangers when the compressor speed is 5,000 RPM are 1.4 K and 2.4 K, respectively. And the result shows that when the condenser subcooling is fixed, changing the condenser air flow rate does not affect the approach temperature much. And an extra calculation was performed with an 8,600 RPM compressor speed to evaluate the effect of compressor speed on the approach temperature. The calculation shows a 0.7 K increase in the evaporator approach temperature, which is not very much. Therefore, the approach temperatures obtained at 5,000 RPM were used when designing sub-cycle heat exchangers.

A modified KC thermodynamic model is used to calculate sub-cycle boundary conditions. In the modified thermodynamic model, the same pressure drop calculation method as the Dymola model was added. And the average approach temperature calculated in Dymola was used.

The same changes were made to the FT-VIC thermodynamic model to test its performance and were compared with the Dymola model results. Figure 47 and Figure 48 show the comparison of heating capacity and compressor power, respectively. As you can see, the models' results match very well, with a deviation of less than 1%.

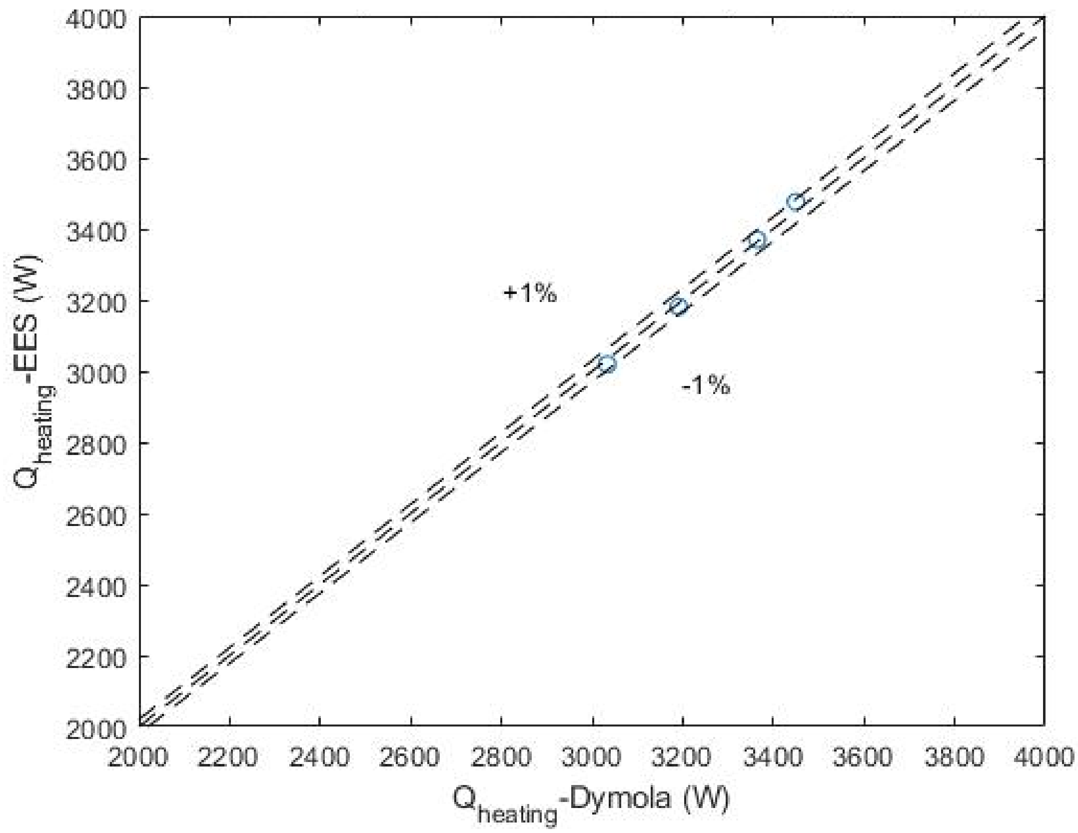

Figure 47: FT-VIC thermodynamic model and Dymola model comparison, heating capacity

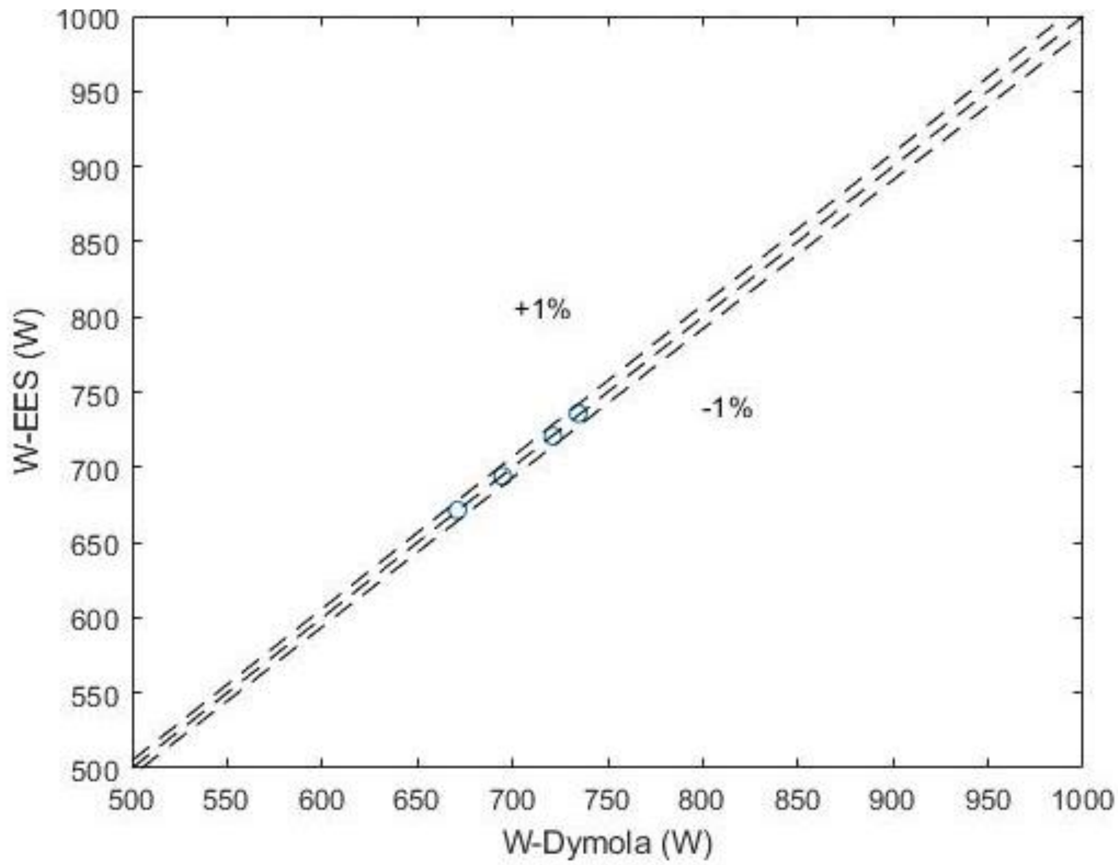

Figure 48: FT-VIC thermodynamic model and Dymola model comparison, compressor power

Because the idea of the KC is to increase heating capacity in extremely cold weather, the design is focused on -15°C. The boundary conditions for the cycle model are as follows:

- Sub-cycle condenser approach temperature ($AT_{sub,cond}$) is 10 K. And its subcooling is 5 K.
- Sub-cycle evaporator approach temperature ($AT_{sub,evap}$) is 5 K. And its superheating is 5 K.
- Outdoor heat exchanger approach temperature (AT_{oHX}) is 1.4 K. And its subcooling is 10 K.
- Indoor heat exchanger approach temperature (AT_{iHX}) is 2.4 K. And its superheating is 5 K.

- N_s = 3,000 RPM.
- N_m = 8,600 RPM.
- The ambient temperature and cabin temperature are -15°C.
- Relative humidity = 0%.
- Outdoor heat exchanger air velocity is 3 m/s.
- The indoor heat exchanger air mass flow rate is 9 kg$/s$.

The calculation results show that the heating capacity is 5.6 kW and the COP of the system without considering the PTC heater is 2.7. The target sub-cycle condenser capacity is 835 W. And the target sub-cycle evaporator capacity is 646 W. Details of design boundary are discussed in the following chapters.

4.2.2 Sub-cycle condenser design

The boundary conditions for the sub-cycle condenser are shown in Table 16.

Table 16: Sub-cycle condenser boundary conditions

Target Q		W	835
Main-cycle side	P_{in}	kPa	270
	h_{in}	kJ/kg	215
	x_{in}	-	0.127
	$\dot{m}$	kg/s	0.0321
Sub-cycle side	P_{in}	kPa	379
	h_{in}	kJ/kg	388
	T_{in}	°C	28.0
	$\dot{m}$	kg/s	0.0044

All sub-cycle heat exchangers are chevron plate heat exchangers as they are compact and are suitable for exchanging heat between two refrigerant flows. And the design was performed in PHEsim, which is a steady-state plate heat exchanger modeling tool developed by CEEE. The correlations used are shown in Table 17.

Table 17: Correlations used in the sub-cycle condenser model

Location	Variable	Calculation method
Main-cycle side	Single-phase HTC	Yan and Lin [85]
	Two-phase HTC	Kim et al. [86]
	Single-phase pressure drop	Modified Muley and Manglik [87]
	Two-phase pressure drop	Khan and Chyu [88]
Sub-cycle side	Single-phase HTC	Yan and Lin [85]
	Two-phase HTC	Yan et al.[89]
	Single-phase pressure drop	Modified Muley and Manglik [87]
	Two-phase pressure drop	Lockhart and Martineli [90]

The designed sub-cycle condenser has nine plates, and the flow path configuration of the designed sub-cycle condenser is shown in Figure 49. The blue line represents the main-cycle refrigerant flow, and the red line represents the sub-cycle refrigerant flow. Arrows at the end of lines indicate their flow direction. Because the main-cycle side has a more significant mass flow rate, in this design, the main-cycle side has one pass, and the sub-cycle side has two passes.

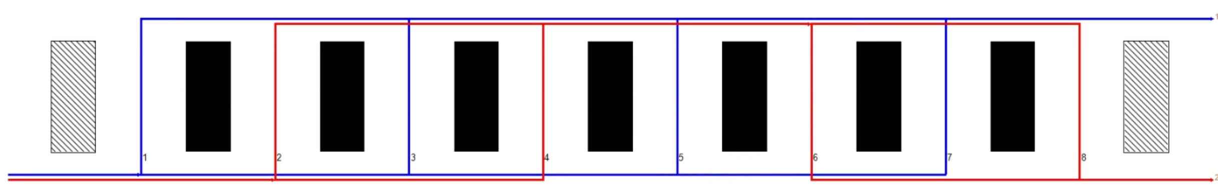

Figure 49: Sub-cycle condenser flow path configuration

Detailed geometric information of the designed sub-cycle condenser can be found in Table 18. It also includes the simulation results of the designed heat exchanger. The designed heat exchanger has 842 W heating capacity, which meets the design requirement. Also, its pressure drops on both sides are very small. Another finding is that the sub-cycle side has a much more significant pressure drop than the main-cycle side. One reason is that the main-cycle side only has a low-quality two-phase flow, but the sub-cycle side also has pure vapor flow in the condenser inlet, which has higher flow velocity and Reynold number. This could lead to a higher pressure drop on the sub-cycle side.

Table 18: Designed sub-cycle condenser geometry and simulation results

Parameter	Value	Unit
Number of plates	9	-
Main-cycle side passes	1	-
Sub-cycle side passes	2	-
Length	100	mm
Width	62.5	mm
Channel hydraulic diameter	2.6	mm
Plate thickness	0.5	mm
Chevron angle	60	degree
Corrugation depth	2.2	mm
Corrugation pitch	6.25	mm
Surface enlargement factor	1.22	-
Capacity	842	W
Main-cycle side pressure drop	0.17	kPa
Sub-cycle side pressure drop	0.54	kPa

4.2.3 Sub-cycle evaporator design

The boundary conditions for the sub-cycle evaporator are shown in Table 19.

Table 19: Sub-cycle evaporator boundary conditions

Target Q		W	646
Main-cycle side	P_{in}	kPa	244
	h_{in}	kJ/kg	194
	T_{in}	°C	-7.4
	$\dot{m}$	kg/s	0.0230
Sub-cycle side	P_{in}	kPa	89
	h_{in}	kJ/kg	201
	x_{in}	-	0.224
	$\dot{m}$	kg/s	0.0044

The correlations used in the sub-cycle evaporator model are listed in Table 20. The correlations of single-phase flow are identical to that of the sub-cycle condenser model. And correlations of two-phase flow switches. Because in the sub-cycle evaporator, the sub-cycle side is evaporating, while the main-cycle side is mainly liquid-phase heat transfer.

Table 20: Correlations used in the sub-cycle evaporator model

Location	Variable	Calculation method
Main-cycle side	Single-phase HTC	Yan and Lin [85]
	Two-phase HTC	Yan et al. [89]
	Single-phase pressure drop	Modified Muley and Manglik [87]
	Two-phase pressure drop	Lockhart and Martineli [90]
Sub-cycle side	Single-phase HTC	Yan and Lin [85]
	Two-phase HTC	Kim et al. [86]
	Single-phase pressure drop	Modified Muley and Manglik [87]
	Two-phase pressure drop	Khan and Chyu [88]

Figure 50 and Table 21 show the flow path configuration and simulation results. The designed heat exchanger is identical to the sub-cycle condenser. And the calculated cooling capacity is 678 W, which is 5% higher than the design requirement. And its pressure drop is also minimal. Like the sub-cycle condenser, its sub-cycle side has a higher pressure drop than the main-cycle side. This result is because the main-cycle side is mainly liquid flow, while the sub-cycle side has two-phase flow and vapor flow.

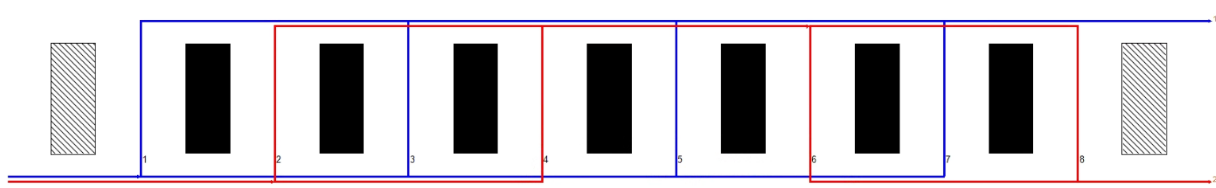

Figure 50: Sub-cycle evaporator flow path configuration

Table 21: Designed sub-cycle evaporator geometry and simulation results

Parameter	Value	Unit
Number of plates	9	-
Main-cycle side passes	1	-
Sub-cycle side passes	2	-
Length	100	mm
Width	62.5	mm
Channel hydraulic diameter	2.6	mm
Plate thickness	0.5	mm

Chevron angle	60	degree
Corrugation depth	2.2	mm
Corrugation pitch	6.25	mm
Surface enlargement factor	1.22	-
Capacity	678	W
Main-cycle side pressure drop	0.08	kPa
Sub-cycle side pressure drop	0.33	kPa

Since both sub-cycle heat exchangers share the same design, only one sub-cycle model is needed. Because the plate heat exchanger involves parallel flow in the model, running calculations with heat transfer correlation often leads to a solver stiff. Thus, the simple heat transfer coefficient model is used in the calculation. The input heat transfer coeffects are the average heat transfer coefficient calculated in the PHEsim. Table 22 shows the comparison between PHEsim and Dymola models.

Table 22: Dymola plate heat exchanger model VS. PHEsim model

HX	Parameter	PHEsim result	Dymola result
Sub-cycle condenser	Capacity	842 W	866 W (+2.9%)
	Main-cycle side pressure drop	0.17 kPa	0.17 kPa
	Sub-cycle side pressure drop	0.54 kPa	0.53 kPa
Sub-cycle evaporator	Capacity	678 W	655 W (-3.4%)
	Main-cycle side pressure drop	0.08 kPa	0.08 kPa
	Sub-cycle side pressure drop	0.33 kPa	0.33 kPa

For the sub-cycle condenser, the Dymola model shows a bit higher capacity, while for the sub-cycle evaporator, the Dymola model slightly underpredicts its capacity.

One thing to notice is that the pressure drops predicted by the model are very small, which is a bit unrealistic. In addition, this significantly slows down the model during the initialization. Therefore, when I used these models in the KC model, I set the pressure drop on both sides to 10 kPa.

4.3 Steady-state simulation in cold weather

Steady-state simulations were performed in cold weather to compare the performance of three cycles. In this simulation, the cabin model was removed. The boundary conditions of the simulation are:

- The ambient temperatures are set to be -5°C and -15°C.
- To ensure that the simulation can reach a steady state, the air inlet relative humidity is set to 0%.
- The indoor heat exchanger air mass flow rate is 9 kg/min.
- Ram air pressure drop compensation is ignored by setting the vehicle speed to 0 m/s.
- The target suction superheating is 5K. And the target condenser outlet subcooling is 5K when it is possible to control.
- For KC, the sub-cycle compressor speed is fixed at 3000 RPM.
- Because during the simulation, the compressor overall pressure ratio can be higher than the maximum pressure ratio I used when creating the compressor efficiency curves, to avoid unreasonable compressor efficiency output due to extrapolation, fixed compressor efficiency is applied in the simulation. The compressor volumetric and isentropic efficiency is set to 70%. And the mechanical and motor efficiency is set to 90%.

Results are shown in Table 23. It can be seen from the table that in terms of efficiency, BC is the best. And in terms of heating capacity, KC is the best. Compared to FT-VIC, when the ambient temperature is -15°C, KC increases heating capacity by 13.0% but increases power consumption by 31.4%. And the ratio of the heating capacity increase over the power consumption increase is

2.1. When the ambient temperature is -5°C, KC increases heating capacity and power consumption by 13.9% and 31.0%. And the ratio of the heating capacity increase over the power consumption increase is 1.8. Because this ratio is larger than 1, KC is more efficient than the electric heater. And the incremental heating capacity increases as the ambient temperature rises. However, the ratio of the heating capacity increase over the power consumption increase drops as the ambient temperature drops. Therefore, it is more efficient at lower ambient temperatures.

Table 23: Steady-state simulation results

Parameter	Unit	T_{amb} = -15°C			T_{amb} = -5°C		
-	-	BC	FT-VIC	KC	BC	FT-VIC	KC
$\dot{Q}_{outdoor}$	W	3647	3851	4202	4437	4903	5345
$\dot{W}$	W	834	908	1038	1322	1547	1796
$\dot{W}_{sub}$	W	0	0	155	0	0	230
COP	-	5.27	5.13	4.42	4.25	4.06	3.53
Comp speed	RPM	8600	8600	8600	8600	8600	8600
$\dot{Q}_{heating}$	W	4392	4661	5268	5618	6285	7156
$T_{indoor,air,out}$	°C	6.3	7.7	10.6	23.3	26.7	31.1
P_{suc}	kPa	130	128	124	183	176	169
P_{inj}	kPa	0	250	287	0	368	430
P_{dis}	kPa	425	445	490	704	779	881
PR	-	3.27	3.48	3.96	3.85	4.43	5.20
T_{sup}	°C	5.0	5.0	5.0	5.0	5.0	5.0
T_{sub}	°C	4.9	5.0	5.0	4.1	5.0	5.0
Fan flow rate	CFM	1103	1103	1102	1099	1099	1098

4.4 Transient simulation with UDDS driving cycle

Mobile air conditioners or heat pumps always operate in a transient condition. Thus, it is necessary to perform transient simulations to evaluate their performance in driving conditions.

4.4.1 Boundary conditions

In this study, transient simulation was performed for three cycles under the below driving pattern:

- 5 mins idle + Urban Dynamometer Driving Schedule (UDDS)

This driving cycle represents a typical driving pattern in the city. The duration is 1669 seconds, and the average vehicle speed (excluding the 5 minutes idle) is 19.69 mph (31.69 km/h), and the total distance is 7.45 miles (11.99 km).

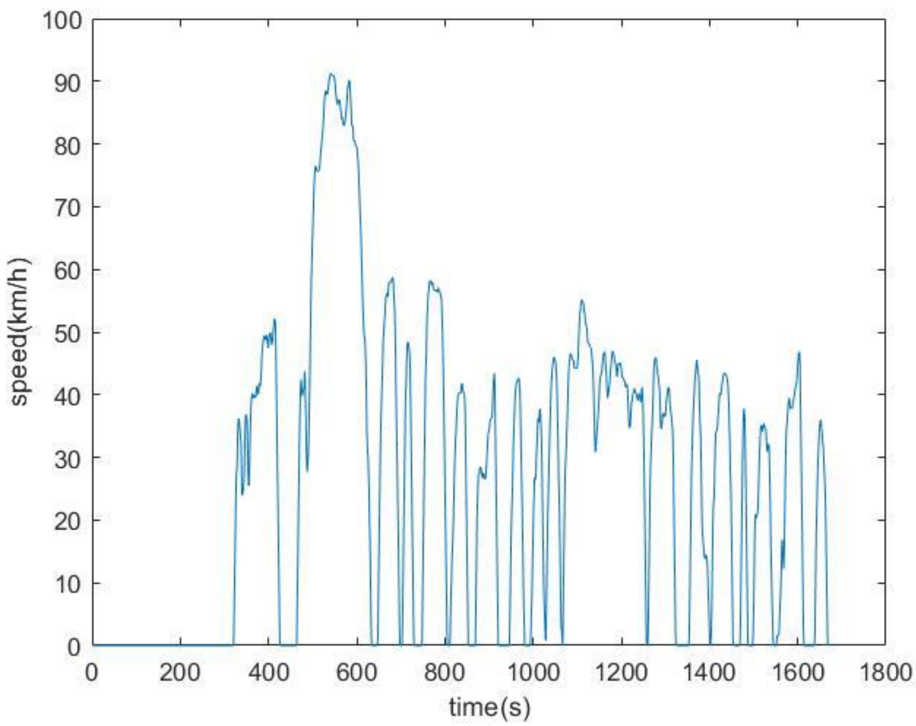

Figure 51: Driving cycle: 5 mins idle + UDDS

Since the focus of this study is on the heat pump in extreme conditions, simulation was performed in -15°C conditions. The ambient relative humidity is set to 70%, the sub-cycle compressor speed is fixed at 3,000 RPM, which is the same as the steady-state simulation, and all compressor models share fixed 70% volumetric and isentropic efficiency and 90% mechanical and motor efficiency.

Table 24 lists the parameters used in the cabin model. It is assumed that only one driver is inside the cabin without solar radiation. So, the soak temperature at the beginning of the simulation is also 0°C.

Table 24: Cabin parameters

Parameter	Value
Number of people (includes driver)	1
Sensible load per passenger	158 W
Latent load per passenger	35 W
Internal volume	2.4 m^3
Collective mass	150 kg
Internal HT area	8.77 m^2
Outer HT area	14.9 m^2
Solar radiation	0 W
Cabin initial temperature	-15°C
Soak temperature	0°C
Air recirculation	50%

4.4.2 Results

Figure 52 shows the heating capacity over time. It is clear that in terms of heating capacity, KC has the highest heating capacity, followed by VIC. And BC has the lowest heating capacity at any given time. Vehicle speed is also plotted in the same graph. In general, the heating capacity tends to increase when the vehicle speed is high. This is because when the vehicle speed increases, the airflow passing the outdoor heat exchanger increases, which leads to a rise in the suction pressure and density. As a result, the compressor discharge mass flow rate increases and causes the heating capacity to increase. Overall, the heating capacity is relatively stable compared to the vehicle speed change. Probably because the indoor heat exchanger air flow rate is stable, and its performance change is mainly induced by the change of refrigerant inlet states. The most significant increase in heating capacity can be observed between 500 seconds and 600 seconds. During this period, the vehicle runs at its peak speed of the driving cycle. And the ram air pressure rise dominates the air side pressure change and generates a much higher outdoor heat exchanger air flow rate.

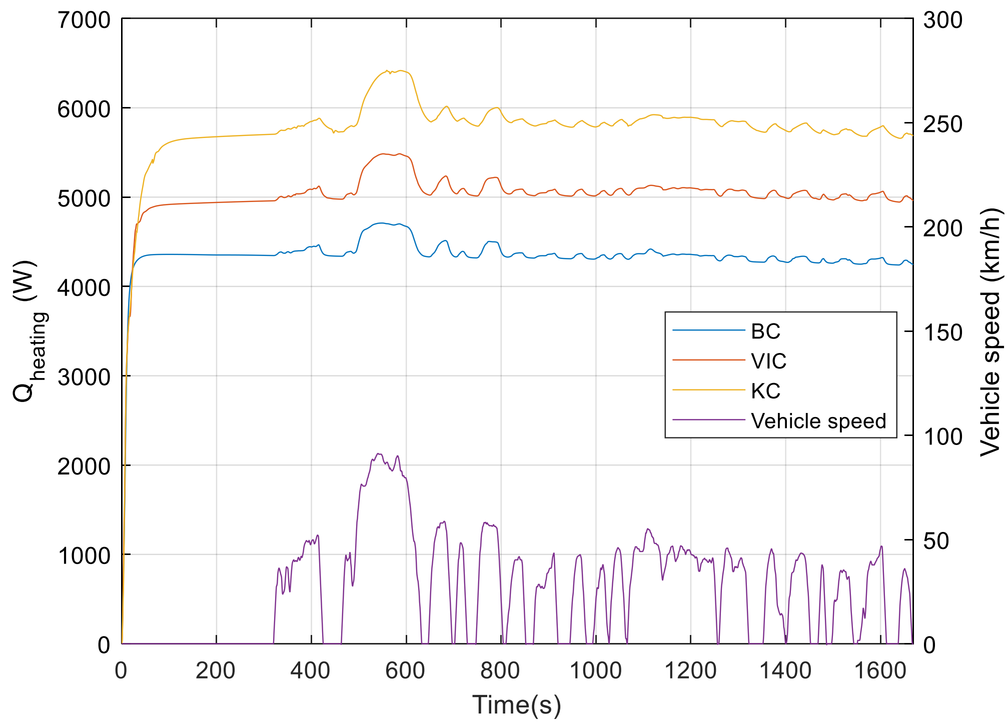

Figure 52: Heating capacity and vehicle speed over time

Figure 53 and Figure 54 show the accumulated heating capacity and compressor power consumption over time. Because KC has the highest heating capacity during the simulation at any given time, its accumulated heating capacity is also the highest. However, its accumulated power consumption is also the highest due to the addition of the sub-cycle compressor and the increased power consumption of the main-cycle compressor, which is caused by the high pressure ratio and mass flow rate. At the end of the simulation, the accumulated heating capacity of KC is 14.8% higher than VIC and 32.7% higher than BC. However, the accumulated power consumption of KC is 32.4% higher than VIC and 64.4% higher than BC. As expected, KC consumes more energy and generates more heating capacity. Figure 55 shows the cabin room temperature and system COP over time. Since the fluctuation in the heating capacity is small, the cabin room temperature rises smoothly over time. And because KC has the highest heating capacity, its cabin room temperature increases fastest. At the end of the driving cycle, the cabin room temperature of KC is 3.6°C and 7.0°C higher than that of VIC and BC, respectively. As for the system COP, the cycle that produces the least amount of heating capacity has the highest COP. And all COPs decrease over time. That is because as the frost is building up, the evaporating pressure drops, which leads to a rise in pressure ratio and a decrease in suction density.

Figure 56 shows the mass of all frost over time and the outdoor heat exchanger air-side pressure drop over time. It can be seen that the frost is built almost linearly over time, except roughly between 500 seconds and 600 seconds. In this period, the vehicle speed is high, and ram air dominates the air flow rate passing through the outdoor heat exchanger. The air flow rate is too high to maintain the latent load. Thus, the growth of the frost stops. It resumes until the air flow rate decreases. Another trend that can be observed in this graph is the relationship between air-side pressure drop and frost thickness. As the frost grows, the air side pressure drop rises over time, as expected.

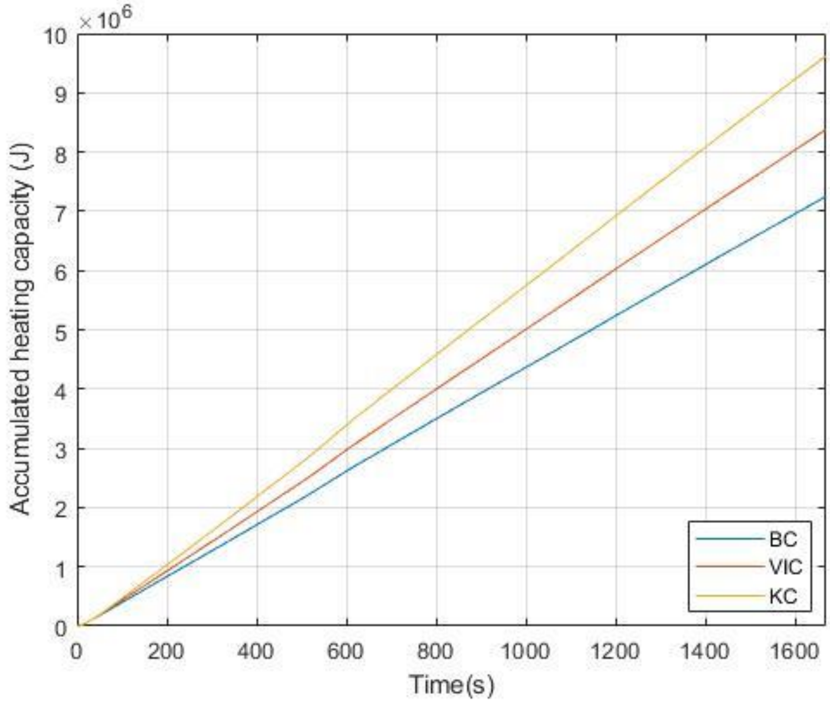

Figure 53: Accumulated heating capacity

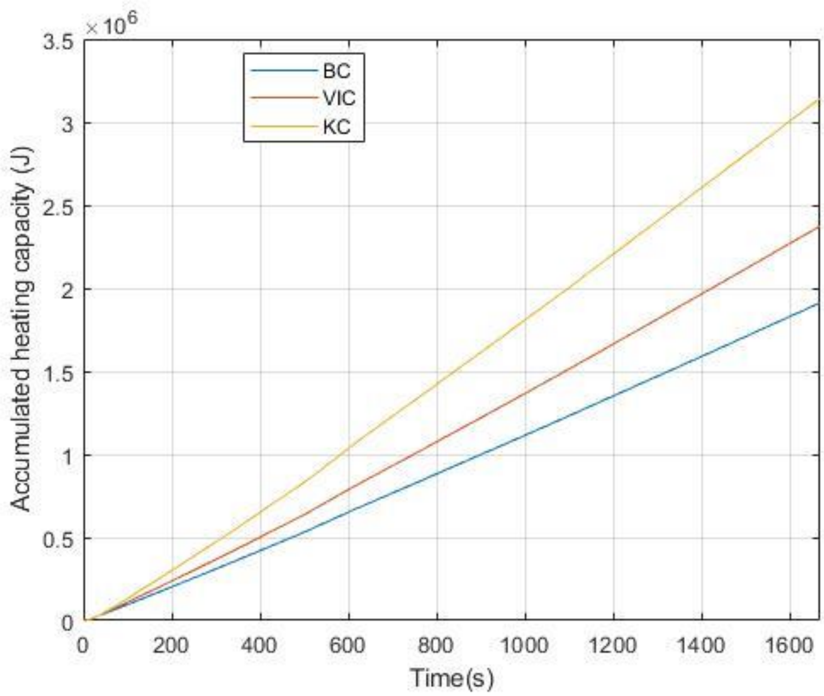

Figure 54: Accumulated power consumption

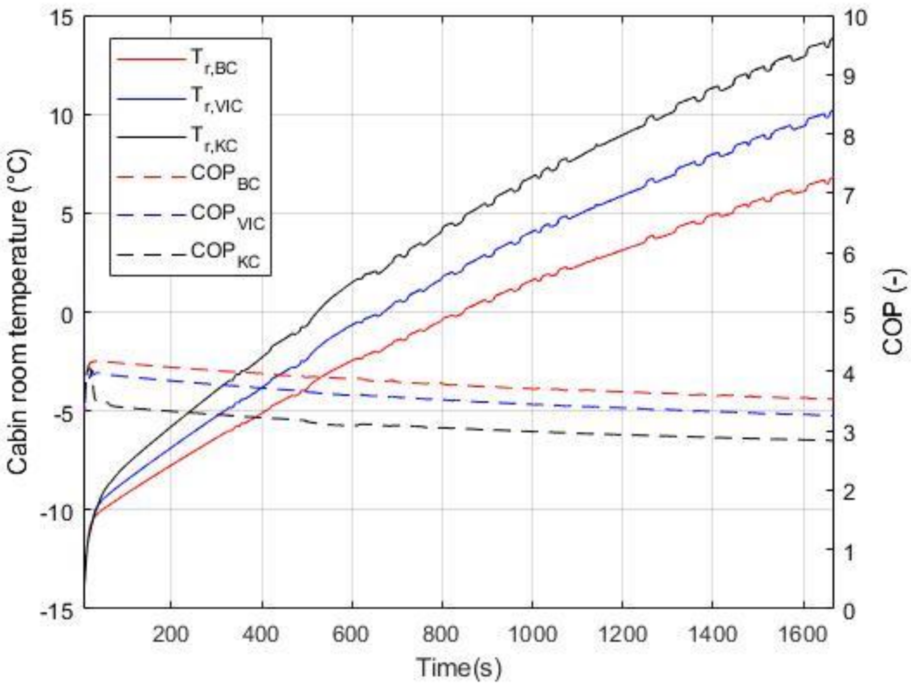

Figure 55: Cabin room temperature and COP over time

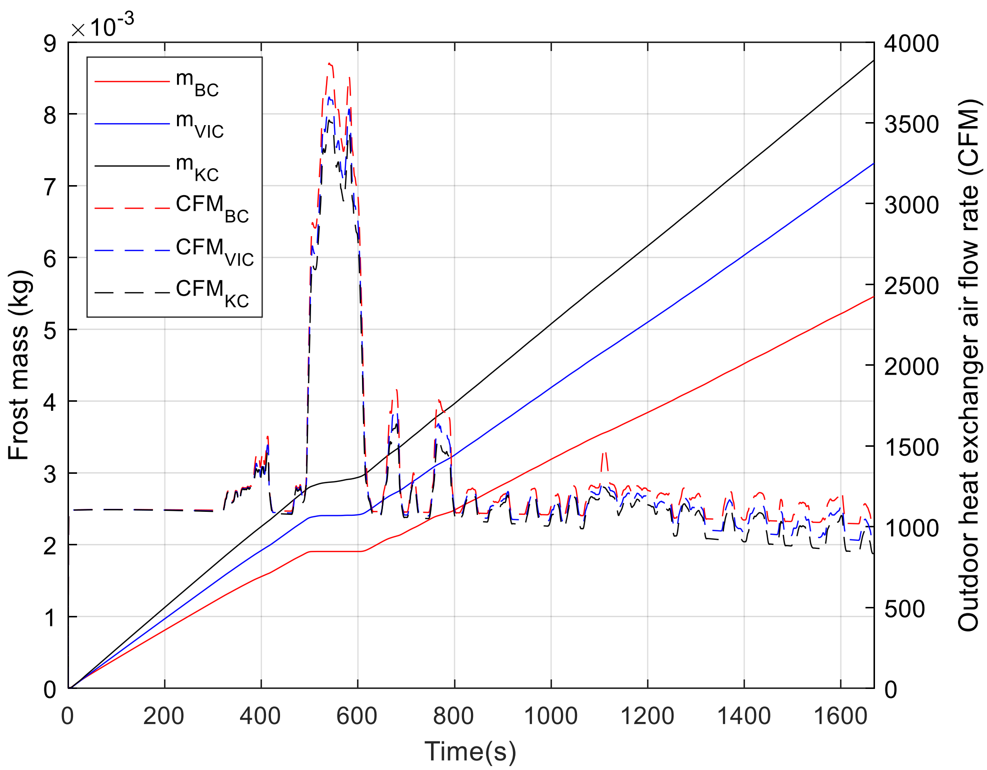

Figure 56: Frost mass increase and air flow rate over time

4.5 Chapter summary and conclusions

This chapter discusses the development of the transient model for BC/FT-VIC/ KC and the performance comparison between the three cycles. The summaries of this chapter are as follows:

- Basic heat pump cycle (BC), Flash tank-based vapor injection heat pump cycle (FT-VIC), kangaroo heat pump cycle (KC) models, and corresponding components models were developed based on CEEE Modelica Library (CML).
- Simulations were performed by using the FT-VIC model. The boundary conditions are the same as simulation #43, but instead of fixing the indoor heat exchanger air outlet temperature, the compressor speed is fixed at 5,000 RPM. Calculation results show that the approach temperature does not change much.
- The obtained approach temperature was used to update the thermodynamic model, which was used to obtain the boundary conditions for the sub-cycle heat exchanger design.
- Steady-state simulations were performed with the developed model. Results show that when compared to FT-VIC, at -15°C, KC increases heating capacity by 13.0%, but increases power consumption by 31.4% when compared to FT-VIC. And at -5°C, KC increases heating capacity by 13.9% but increases power consumption by 31.0%. Overall, KC is more efficient at lower ambient temperatures but can increase heating capacity more at higher ambient temperatures.
- Transient simulations were performed with Urban Dynamometer Driving Schedule (UDDS) driving cycles at -15°C. Results show that KC heats the cabin faster than FT-VIC and BC but consumes more energy. At the end of the driving cycle, the cabin room temperature of KC is 3.6°C and 7.0°C higher than that of VIC and BC, respectively. The

result also shows that when the vehicle speed is high, the ram air will dominate the outdoor heat exchanger air flow and increase heating capacity. In addition, the effect of frost at -15°C is small, probably due to the low humidity ratio at low temperatures.

5 Centrifugal compressor design and performance evaluation for future MACs with high cooling demand

Volume and weight are crucial for MACs. The space under the hood is always limited, and the weight of MACs directly impacts the driving distance of the electric vehicle. To reduce the system size and weight, one can replace the scroll compressor with a miniature centrifugal compressor. H. J. Van Gerner [32] built and tested a centrifugal compressor that was 10 times lighter than a traditional compressor for space applications. And Carré et al. [30] built a centrifugal compressor that was significantly smaller than the traditional scroll compressor for a heat pump application. Those examples show the feasibility of miniature centrifugal compressors. However, it is very difficult to design a centrifugal compressor for the kangaroo cycle. Because the main-cycle of the kangaroo cycle requires a compressor that has vapor injection capability, which is difficult for a centrifugal compressor. And the sub-cycle's refrigerant mass flow rate is too small for a centrifugal compressor. Thus, in this study, a centrifugal compressor was designed for a different cycle, which does not require vapor injection and has a high refrigerant mass flow rate requirement.

5.1 Cycle schematics and operating conditions

In this study, a centrifugal compressor was designed for an EV whose battery generates tremendous heat during fast charging. Three operating modes are involved in this study: fast charging mode, cabin cooling mode, and heating mode. Their details are discussed below.

5.1.1 Fast charging mode

The most important mode in this study is the Fast-charging mode. Its schematic is shown in Figure 57. On the low-pressure side, only the battery chiller is activated. And on the high-pressure side, there are three condensers: air condenser (COND), low-temperature water condenser (WCOND L), and high-temperature water condenser (WCOND H). They are called "water condenser" because instead of dumping heat directly into the air, they dump heat into a liquid. The actual working fluid is a 50% weighted ethylene glycol and water mixture, which is a common anti-freezer used in automobiles. The two water condensers are connected to two separate coolant loops. For WCOND L, it is connected with the Low-Temperature Radiator (LTR). For WCOND H, it connects to another radiator and a heat source. The heat source can be the vehicle's powertrain or the onboard electronics. Because those parts also generate heat and cause the coolant temperature to increase, the connected radiator is called High-Temperature Radiator (HTR). In the following section, the coolant loop connected with LTR is called the LTR loop, and the coolant loop connected with HTR is called the HTR loop. Note that COND, LTR, and HTR are arranged in series so that the outdoor air first passes COND, then LTR, and finally HTR. This arrangement allows maximum utilization of the air temperature.

During the operation, the refrigerant discharged from the compressor first goes into WCOND H and dumps heat into the high-temperature coolant. Then, it goes through the WCOND L and releases heat to the low-temperature coolant. Ideally, the refrigerant at this point should be in the two-phase region. So that when the refrigerant enters COND, it can maximize its efficiency and create as much sub-cool as possible. The leaving refrigerant then throttles to the evaporating pressure and enters the battery chiller, which cools the coolant to the target coolant temperature.

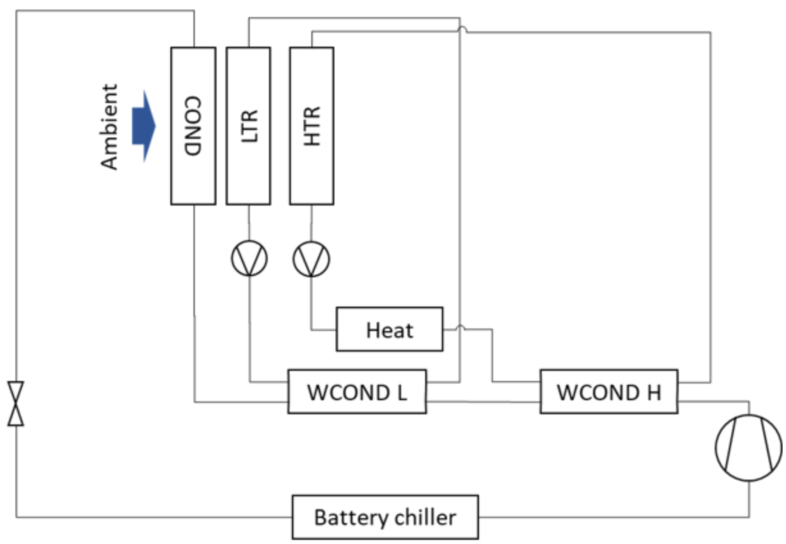

Figure 57: Schematics of the fast-charging mode

5.1.2 Cabin cooling mode

The schematic of the cabin cooling mode is shown in Figure 58. The high-pressure side is the same as the high-pressure side, but on the low-pressure side, the battery chiller is replaced with an evaporator. So that instead of creating cold coolant, the air conditioner now creates cold air in the cabin.

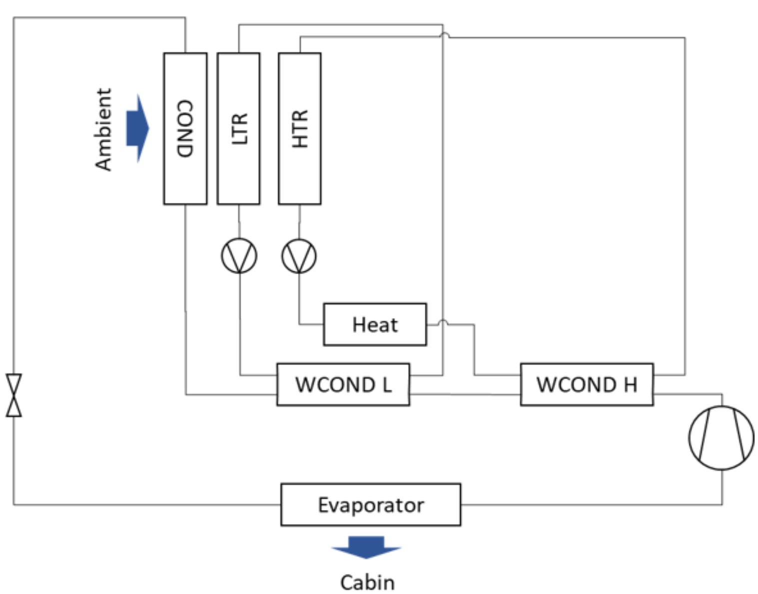

Figure 58: Schematics of the cabin cooling mode

5.1.3 Heating mode

The schematic of the heating mode is shown in Figure 59. In the heating mode, the cycle is reversed. On the high-pressure side, it is the cabin condenser, which provides hot air for the cabin. And on the low-pressure side, the HTR loop is used to recover the waste heat from the powertrain and the onboard electronics, while the LTR loop is used to absorb heat from the ambient.

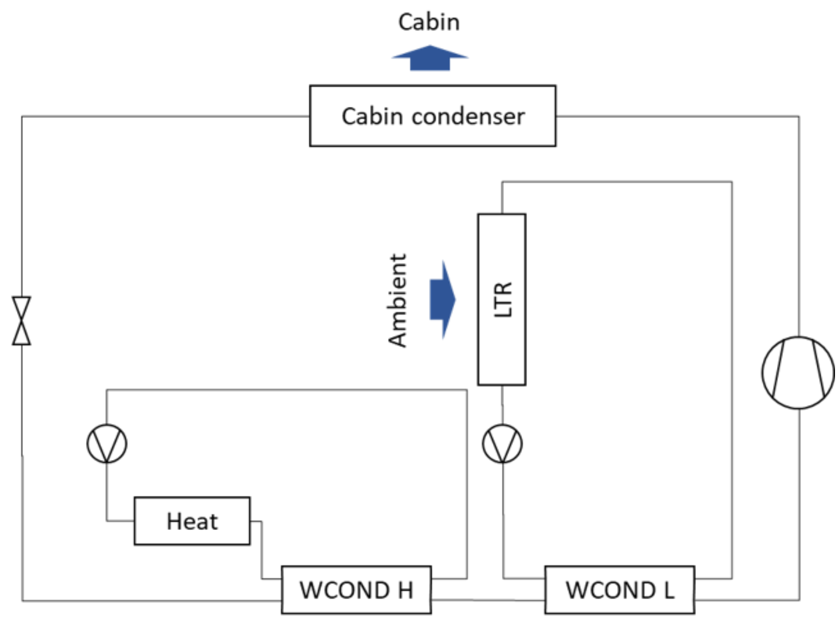

Figure 59: Schematic of the heating mode

The actual system has all the components involved in above mentioned modes. And the switching of modes can be realized by using valve controls. In this study, to simplify the model, separate models were developed for these three modes.

5.2 Thermodynamic model and simple analysis

Before designing the compressor, it is necessary to know the boundary conditions first. To do that, thermodynamic models of the three operating modes were developed. Similar to the thermodynamic models discussed in Chapter 3, heat exchangers were modeled based on approach temperature. The previous model was developed in EES. However, it becomes challenging to manage unknowns when the program becomes more complicated. Therefore, in this chapter, the thermodynamic models were developed in Dymola. I first built the component models and then constructed the cycle model by connecting the refrigerant ports of the required component models. This approach allows me to build complex cycle models without worrying about the solving procedure. The solver in Dymola also runs faster for complex problems.

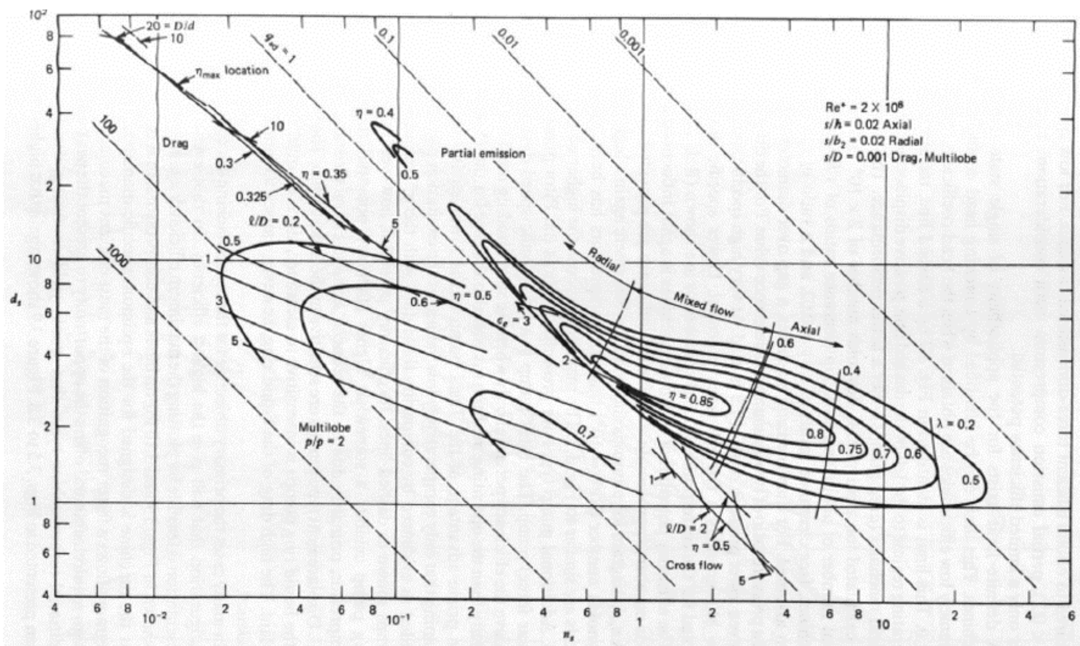

Figure 60: $n_s d_s$ diagram [91]

To roughly estimate the centrifugal compressor's size and speed, a simple centrifugal compressor model based on the $n_s d_s$ diagram from Balje [91] was developed in Dymola. The definition of specific speed (n_s) and specific diameter (d_s) are as follows:

$$n_s = \frac{\omega\sqrt{\dot{Q}_{in}}}{\Delta h^{0.75}} \tag{113}$$

$$d_s = \frac{D\Delta h^{0.25}}{\sqrt{\dot{Q}_{in}}} \tag{114}$$

Where ω is the impeller rotational speed, $\dot{Q}_{in}$ is the inlet volumetric flow rate, Δh is the adiabatic head, and D is the impeller diameter. As shown in Figure 60, the $n_s d_s$ diagram consists of multiple efficiency contours. The left-most point of each contour represents the minimum compressor speed needed to achieve that compressor efficiency. Then the minimum compressor speed required to reach any target efficiency (50%-85%) can be easily calculated by using linear interpolation between those data points. Note that the $n_s d_s$ diagram is valid when Re = 2,000,000, which may not be true in the actual compressor design. Therefore, the actual efficiency at the selected specific speed and diameter may not be the same. Since this compressor model is also efficiency-based, its governing equations are the same as all the other compressor models discussed in the previous chapters.

Table 25 lists the boundary conditions for cycle simulation. Due to the non-disclosure agreement, the exact value cannot be shared. Instead, the percentage of changes is displayed. In this table, the fast charging mode (Datum) is the baseline, which is already mass-produced. Cells in other columns show the percentage difference between those conditions and the Datum condition. The target cooling capacity in the fast charging mode for the new system is five times the current capacity. The target cabin cooling capacity is the same as the fast-charging cooling capacity but at a much higher ambient temperature. As for the heat pump, since additional electric heaters can provide heating, there is no strict requirement for the heating capacity.

Since the main focus of this study is the fast charging mode, the calculation was performed under this boundary condition. The first calculation assumes that the compressor has only one compression stage, and the results are shown in Table 26. In the table, D_2 is the impeller outlet diameter, and PR is the pressure ratio. It can be seen that the higher the rotational speed, the smaller the impeller diameter needed.

Table 25: Boundary condition of different modes

Mode	Fast charging mode (Datum)	Fast charging mode	Cabin cooling mode	Heat pump mode
Target capacity	DATUM	500%	500%	-
Ambient temperature		25°C	45°C	-7°C
Radiator air flow rate		+37%/+17%	+37%/+17%	+17%
Cabin HX air flow rate		-	826%	+826%
LTR coolant flow rate		same	same	+7%
HTR coolant flow rate		same	same	-71%
Power element heat		same	same	300%
Battery coolant inlet Temperature		25°C	-	-
Battery coolant flow rate		same	-	-

At the peak speed, the estimated impeller diameter is only 31 mm, even smaller than a wristwatch. However, reaching such a high speed with a high-power output is almost impossible. At the lowest acceptable speed, the impeller diameter increases to 129 mm, which is still small. In addition, because the impeller size is very small, adding many blades to it is impossible. Thus, reaching a high pressure ratio could be challenging. A two-stage compressor should be a more appropriate design so that the required pressure ratio of each compression stage can be smaller and easier to achieve.

Table 26: Rough compressor performance estimation (single-stage)

Parameter	d_s	n_s	η	speed	D_2	PR	$\dot{m}$	COP
units	-	-	-	kRPM	m	-	kg/s	-
R1234yf	4.0	0.64	0.85	141.1	0.031	5.7	0.2	2
	5.4	0.47	0.80	104.2	0.041	5.7	0.2	2
	6.4	0.39	0.75	86.5	0.049	5.8	0.2	2
	7.6	0.32	0.70	71.0	0.058	5.9	0.2	2
	11.5	0.22	0.60	48.8	0.089	6.1	0.2	2
	16.3	0.16	0.50	35.3	0.129	6.5	0.2	1

The results of the two-stage compressor calculation are shown in Table 27. In the table, subscript 1 stands for the first compression stage, and subscript 2 stands for the second compression stage. And PR_{ratio} is the ratio of PR_1 over PR_2. During the simulation, it was assumed that both compression stages share the same speed. And the calculation was performed by varying the specific speed of the first compression stage. Because the second compression stage's suction pressure is much higher than the first stage's suction pressure, its volume flow rate was lower than the first compression stage. As a result, its specific speed is usually slower than the first compression stage, which leads to lower compression efficiency in the second compression stage.

Table 27: Rough compressor performance estimation (two-stage)

	$n_{s,1}$	η_1	$n_{s,2}$	η_2	seed	PR_1	PR_2	PR_{ratio}	$\dot{m}$	COP
	-	-	-	-	kRPM	-	-	-	kg/s	-
R1234yf	0.64	0.85	0.67	0.86	109.6	3.4	1.7	0.5	0.2	2.43
	0.64	0.85	0.59	0.83	103.5	3.1	1.8	0.6	0.2	2.4
	0.64	0.85	0.53	0.82	98.3	2.9	2	0.7	0.2	2.38
	0.64	0.85	0.49	0.8	93.7	2.7	2.1	0.8	0.2	2.35
	0.64	0.85	0.45	0.79	89.5	2.5	2.3	0.9	0.2	2.32
	0.64	0.85	0.42	0.77	85.7	2.4	2.4	1	0.2	2.28
	0.64	0.85	0.4	0.76	82.2	2.3	2.5	1.1	0.2	2.24
	0.64	0.85	0.38	0.74	79	2.2	2.6	1.2	0.2	2.2
	0.64	0.85	0.36	0.73	76	2.1	2.7	1.3	0.2	2.17
	0.64	0.85	0.34	0.72	73.2	2	2.8	1.4	0.2	2.13
	0.64	0.85	0.33	0.71	70.6	2	3	1.5	0.2	2.1
	0.47	0.8	0.49	0.81	80.7	3.4	1.7	0.5	0.2	2.25
	0.47	0.8	0.43	0.77	76.2	3.1	1.9	0.6	0.2	2.21
	0.47	0.8	0.39	0.75	72.4	2.9	2	0.7	0.2	2.16
	0.47	0.8	0.35	0.72	69	2.7	2.2	0.8	0.2	2.12
	0.47	0.8	0.33	0.71	65.9	2.5	2.3	0.9	0.2	2.08
	0.47	0.8	0.31	0.69	63.1	2.4	2.4	1	0.2	2.03
	0.47	0.8	0.29	0.67	60.6	2.3	2.5	1.1	0.2	1.98
	0.47	0.8	0.28	0.66	58.2	2.2	2.7	1.2	0.2	1.94
	0.47	0.8	0.26	0.64	56.1	2.1	2.8	1.3	0.2	1.9
	0.47	0.8	0.25	0.63	54	2.1	2.9	1.4	0.2	1.86
	0.47	0.8	0.24	0.62	52.1	2	3	1.5	0.2	1.82

In addition, the calculation also shows that as the PR_{ratio} increases, the required compressor speed decreases due to the reduction of the first-stage pressure ratio. And the drawback is a lower overall compression efficiency. Of course, this is just a rough estimation. To design the compressor, a more detailed one-dimensional analysis is needed.

5.3 1D compressor design and optimization

The 1D compressor design was performed by using the two-zone model in COMPAL [92], a commercial centrifugal compressor design software. The two-zone model [93] models the flow passage as the primary and secondary zones. The flow inside the primary zone is considered an isentropic flow, and the secondary zone contains all the losses. The fluid properties of each zone are calculated separately, and they eventually mix at the impeller exit where mixing loss is applied. The design mode in COMPAL requires a small number of inputs, and its internal solver calculates other geometric parameters to match the target total-to-static pressure ratio.

To find the optimum design with the 1D model, it is coupled with Pymoo [94], an open-source Genetic Algorithm (GA) [95] solver. Their communication was realized by a python script, which calls COMPAL in the background every time the solver evaluates the objective function. The problem formulation is as follows:

$$\begin{gathered} f = -\eta_{tot} \\ s.t. \\ \mathrm{r}_{\mathrm{h,1}} - r_{\mathrm{h,1,min}} \leq 0 \\ \mathrm{r}_{\mathrm{h,2}} - r_{\mathrm{h,2,min}} \leq 0 \\ P_{07,2} - P_{7,2} \leq 50\ kPa \\ no\ stall\ or\ choke \end{gathered} \tag{115}$$

Where r_h is the hub radius, P_{07} and P_7 are total pressure and static pressure at the volute throat, and η_{tot} is the overall compressor efficiency. Because Pymoo only solves a minimizing problem, a minus sign was added in front of the η_{tot} to convert it from maximizing to minimizing. As for the constraints, because the impeller inlet hub is not an input to the model, the first constraint is added to avoid an unmanufactured impeller hub radius. And the second constraint is added to ensure that the diffuser and volute can help the refrigerant recover enough kinetic energy and helps reduce the length of the exit pipe.

Design variables in this optimization include:

- Impeller inlet hub-to-tip ratio
    - The hub-to-tip ratio at the impeller inlet determines the impeller inlet size. It typically ranges from 0.3 to 0.5 [31].
- Impeller exit inclination angle (with respect to the rotating axis)
    - The impeller exit inclination angle is a number between 0° and 90°. Typically, for a centrifugal compressor, it is 90°. A small inclination allows the compressor to compress more refrigerant but loses a little pressure ratio.
- Impeller exit blade angle (with respect to the meridional plane)
    - The impeller exit blade angle determines the velocity triangle at the impeller exit, which strongly affects the amount of work the compressor does. A forward blade angle can deliver a high pressure rise but consumes a lot of work, while a backswept blade usually gives the best overall performance. Typically, most backswept angles range from -40° to -50° (minus sign means it is backswept and toward the counter-rotating direction).
- Rotational speed
    - The minimum RPM was selected based on the previous 1D calculation done with the Balje map. And the maximum RPM achievable was used as the maximum RPM.

- The ratio of impeller exit radius over diffuser radius
    - This value determines the vaneless diffuser length. A more extended diffuser can recover more kinetic energy. However, it is also likely to cause compressor stall and has more losses.
- The ratio of diffuser height over impeller exit height
    - In this study, a vaneless diffuser is used. Typically, the diffuser and impeller exit have the same height, so this value is 1. Because of the peripheral speed at the impeller exit, if the diffuser cross-section area is too large, the flow is trapped inside the diffuser. "Pinch" the vaneless diffuser (reduce diffuser height) can increase flow velocity and helps enlarge the compressor's operating range.
- PR_{ratio}
    - As discussed in the simple analysis section, PR_{ratio} strongly impacts compressor efficiency. It is crucial to run optimization with both PR_{ratio} and rotational speed to find the optimum design.

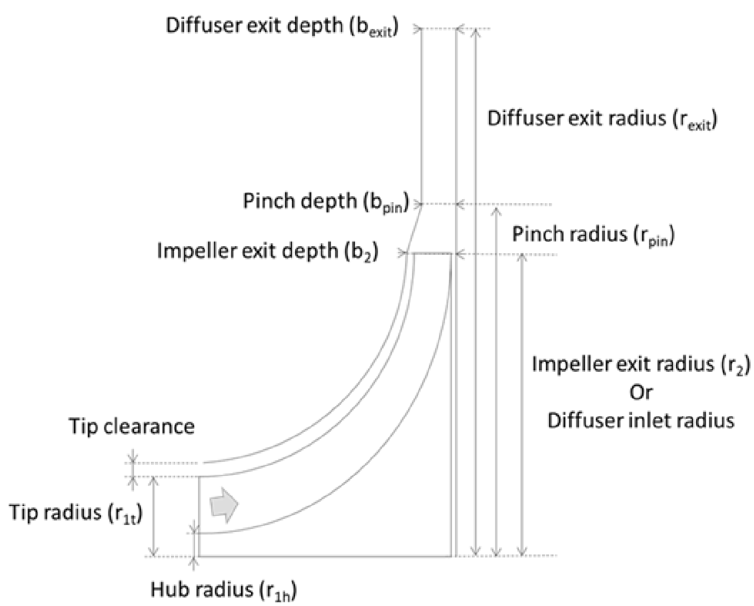

Figure 61: Centrifugal compressor meridional plane

Two separate optimization runs were performed. The population size is 200 and the maximum number of generations is 200. The other termination criterion is that the change in the objective space in the last 30 generations is less than 0.0001, which was evaluated every 20 generations. The selection method used is the tournament method, and the crossover method is simulated binary crossover. The mutation is realized by polynomial mutation. Figure 62 shows the optimization convergence history. After 50 generations, the objective function barely changes, and they are both terminated before reaching the maximum number of generations. And their design variables are the same after rounding. The optimum design's $PR_{ratio} = 0.43$ and has 73.3% overall isentropic efficiency.

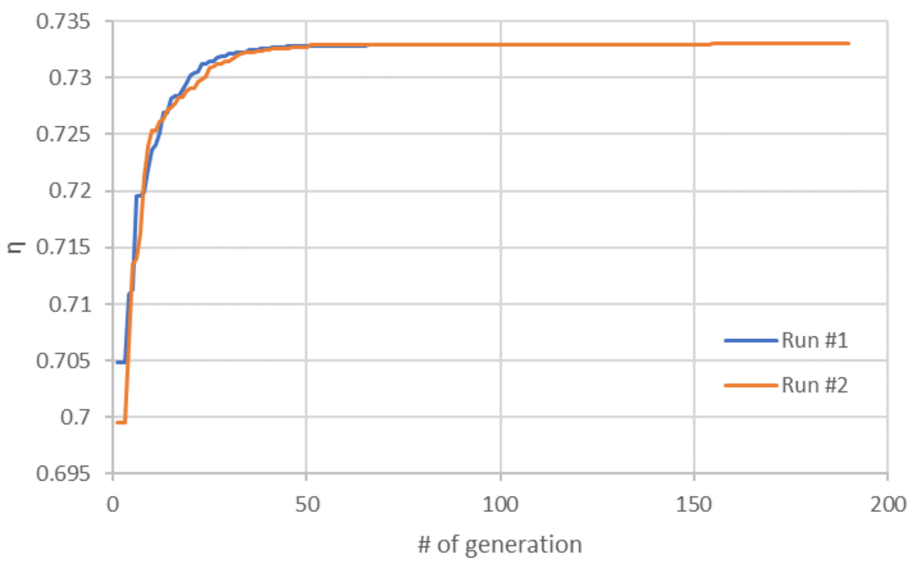

Figure 62: Compressor 1D optimization history

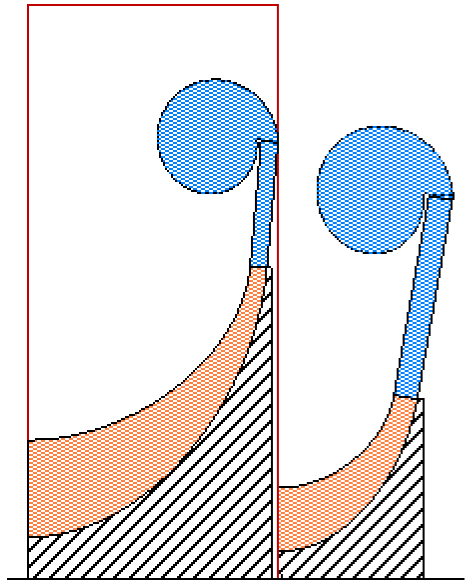

Figure 63: Meridional plane of the 1D optimum design

5.4 CFD analysis and 1D model correction

After the 1D design, a 3D design was performed. The basic procedure is as follows:

1. The initial 3D design was generated in AxCent[92], a 3D centrifugal compressor design software. The blade angle profile along the flow direction was slightly adjusted so that the blade loading calculated by its built-in solver is within the acceptable range. Then three files containing the hub, shroud, and blade profiles were exported.
2. The impeller geometry profiles were imported to the ANSYS 2021R2 BladeGen[96], where the 3D model was reconstructed there.
3. The 3D model was transferred to ANSYS 2021R2 TurboGrid[97], where meshes were generated.
4. ANSYS 2021R2 CFX[98] is used to perform the actual analysis.

5. Once the calculation is done, evaluate the compressor performance. If it does not meet the requirement, adjust the design and redo this procedure from the beginning.

Since this 3D design procedure involves a lot of redesigns of the geometry, only the last impeller CFD analysis is discussed here.

As mentioned before, the fluid domain mesh was created in TurboGrid. The imported geometry from BladeGen is separated into three domains: inlet domain, impeller domain, and outlet domain. Among them, the outlet domain is considered the diffuser domain. In this study, the starting point of the outlet domain is moved half the impeller exit width away from the impeller blade's trailing edge. This makes the model easier to converge. For mesh setup, boundary layer refinement is used. Y+ value is used to improve the grid quality near the boundary. The suggested y+ value for the shear stress turbulence model is 1. The Reynold number at the impeller exit is assumed to be 1×10^6. Some basic mesh setups are listed in Table 28.

Table 28: Fluid domain mesh setup

Parameter	Setup
Tip clearance	Based on the upstream profile
Impeller exit	Extended by half the exit width
Boundary layer	$y^+ = 1.0$
Estimated Re	1.0×10^6
Hub boundary layer y^+	1
Shroud boundary layer offset	0.1
Limit of outlet domain aspect ratio	900
Expansion rate for inlet and outlet domains	1.2

Figure 64 shows the generated mesh for the first compression stage. One advantage of using TurboGrid is that I can do calculations with one slice (blade set) of the impeller instead of doing calculations with the entire compressor, which saves a lot of calculation time.

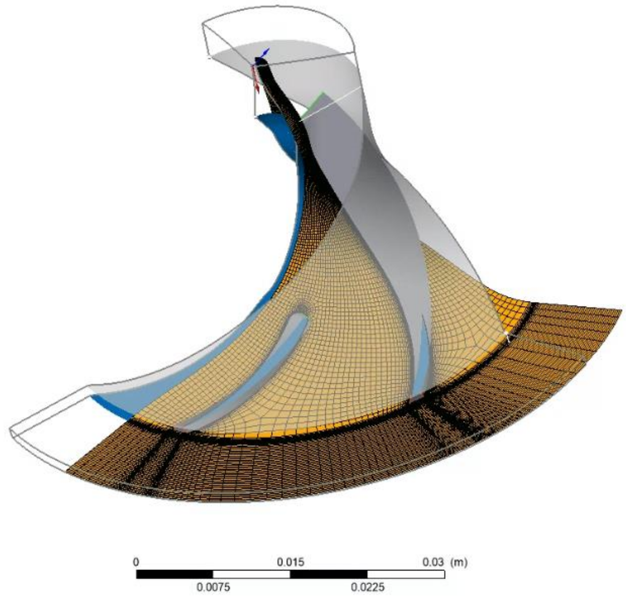

Figure 64: Fluid domain mesh

Once the mesh was generated in TurboGrid, the CFD calculation was set up in CFX through the “Turbo Mode”. The entire fluid domain is separated into two domains during the setup process. A rotating passage domain and a stationary diffuser domain. Shroud tip clearance is only added in the impeller domain. And the interface between the two domains is the stage (mixing plane). Cylindrical coordinates define the inlet flow direction and are perpendicular to the inlet cross-section. And the calculation uses a pressure inlet and a mass flow rate outlet. Table 29 lists the solver setup in CFX. In addition to these settings, a user-defined interrupt condition was implemented:

$$\left(\frac{\sigma(\eta)}{\overline{\boldsymbol{\eta}}}\right)_{50} < 0.05 \;\&\; \left(\frac{\sigma(PR)}{\overline{PR}}\right)_{50} < 0.0005 \tag{116}$$

Where $\left(\frac{\sigma(\eta)}{\overline{\boldsymbol{\eta}}}\right)_{50}$ is the ratio of the standard deviation of compressor efficiency (in %) over the average compressor efficiency over the last 50 steps, and $\left(\frac{\sigma(PR)}{\overline{PR}}\right)_{50}$ is the ratio of the standard deviation of compressor efficiency over the average compressor efficiency over the last 50 steps. If this condition were met, the calculation was considered converged.

Table 29: CFX Solver Setup

Parameter	Setup
Advanced scheme	High resolution
Turbulence numerics	First order
Timescale	Auto (conservative)
Convergence criteria	Max
Residual target	1e-4
Global dynamic model control	On
Compressibility control	On
High speed numerics	On

The CFD calculation results of both compression stages are shown in Table 30. As you can see, the compressor efficiency calculated in the CFD is significantly lower than that of the 1D model. This indicates that the 1D model underpredicts the impeller losses. Multiple reasons could cause this large discrepancy. First, the 1D model is one-dimensional and only considers the main geometry information. For example, it considers the impeller inlet and outlet back angle but does not consider the blade angle profile in between. However, this profile for sure will affect the compressor's performance. Second, the compressor designed in this study has a very small dimension and its tip clearance is relatively large, which could be out of the range of the built-in loss model. It was tuned to improve the 1D model accuracy by adjusting the efficiency of the primary and secondary flows. And the mass fraction of the secondary flow is also increased to bring down the efficiency. After correction, the 1D model shows a similar pressure ratio to the CFD results, while still overpredicting the compressor efficiency.

Table 30: CFD results and 1D model correction

Parameter	CFD	Previous 1D model	Updated 1D model
1st stage η_{tt}	69.4%	75.7%	72.0%
1st stage PR_{tt}	3.56	4.18	3.49

2nd stage η_{ts}	64.7%	74.1%	66.3%
2nd stage PR_{ts}	1.64	1.72	1.63

5.5 Cycle performance evaluation

Once the compressor design is obtained, the next step is to evaluate its performance in the cycle. To do this, I must first resize the existing heat exchangers to a suitable size for the new condition.

5.5.1 Redesign heat exchanger models

There are only two types of heat exchangers of interest: plate heat exchangers and microchannel heat exchangers. Models for these two types of heat exchangers were developed in Dymola. The basic component is the same as the heat exchanger models mentioned in Chapter 4. Therefore, it is not discussed here for brevity. Table 31 lists the correlations used in those models.

Table 31: Correlations used in heat exchanger models

Heat exchanger	Side	Type	Correlation name
HTR/LTR/COND	Air	SP HTC	Chang and Wang [72]
HTR/LTR/WCOND	Coolant	SP HTC	Fixed Nu based on the aspect ratio of the cross-section [99]
HTR/LTR/WCOND	Coolant	SP DP	Laminar DP equation. If turbulence then Blasius
COND/WCOND/Chiller	Refrigerant	SP HTC	Dittus Boelter [100]
COND/WCOND/Chiller	Refrigerant	SP DP	Blasius [99]
COND/WCOND	Refrigerant	TP HTC	Shah [101]
COND/WCOND	Refrigerant	TP DP	Homogeneous pressure drop equation [102]
Chiller	Refrigerant	TP HTC	Gungor and Winterton et al [103]
Chiller	Refrigerant	TP DP	Jung et al. [104]

Figure 65 shows the validation results of the HTR model. A 2.5 correction factor was applied on the coolant side heat transfer coefficient, and the maximum deviation is around 12%. And a 4.0 correction factor is applied to the coolant pressure drop calculation. Though the maximum deviation is 47%, it happens at a low flow rate, and the absolute value is relatively small. Figure 66 shows the validation results of the LTR model. Because they are similar heat exchangers, the same correction factor was applied to the LTR model. The maximum deviation of capacity and pressure drop are 9% and 68%, respectively.

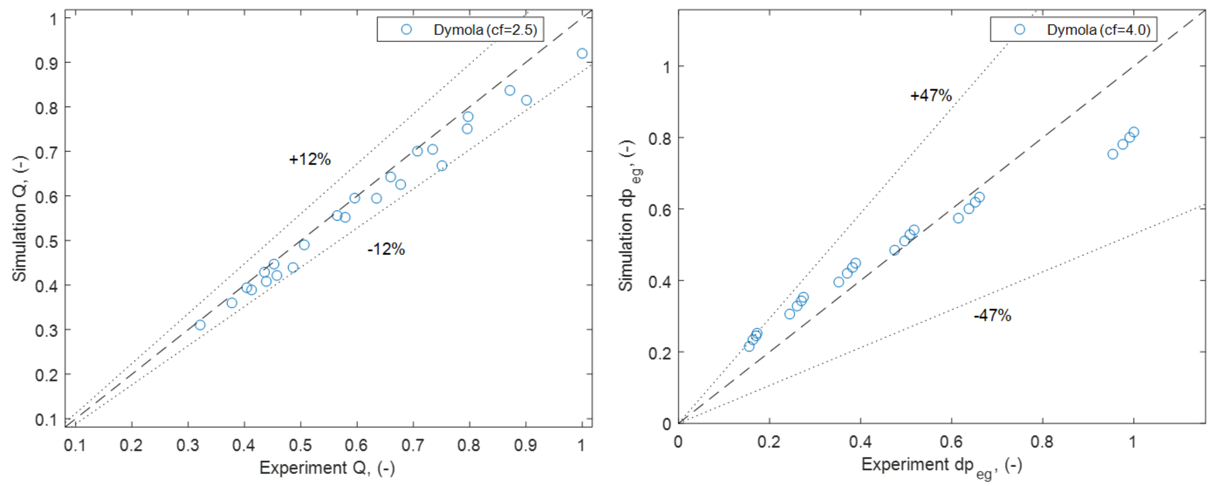

Figure 65: HTR validation (non-dimensionalized)

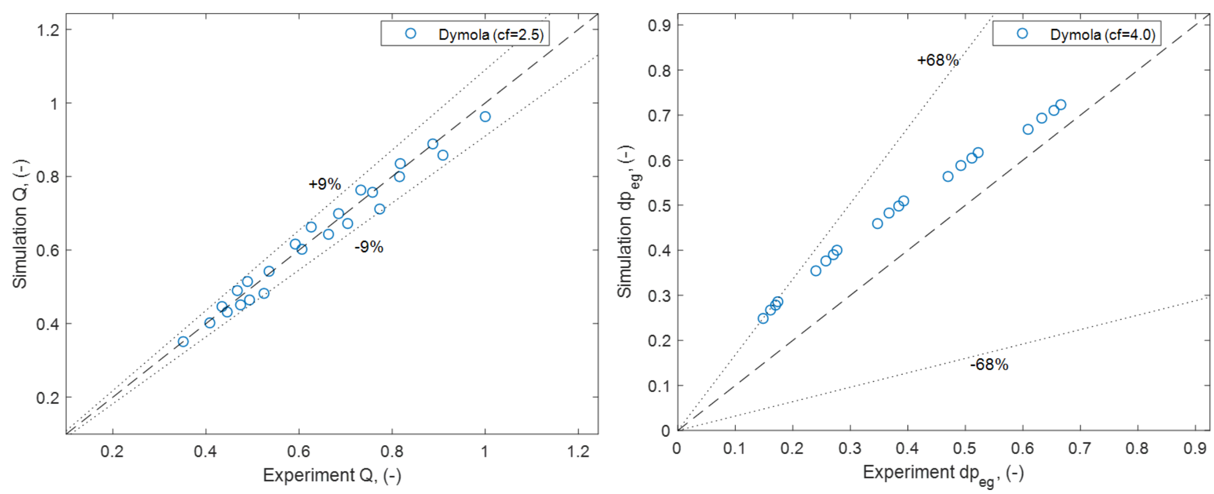

Figure 66: LTR validation (non-dimensionalized)

Figure 67 shows the validation results of the air condenser model. A 1.4 correction factor was applied on the air side, and its maximum capacity deviation is 10%. In addition, a 2.0 correction factor was added to the refrigerant coolant pressure drop calculation.

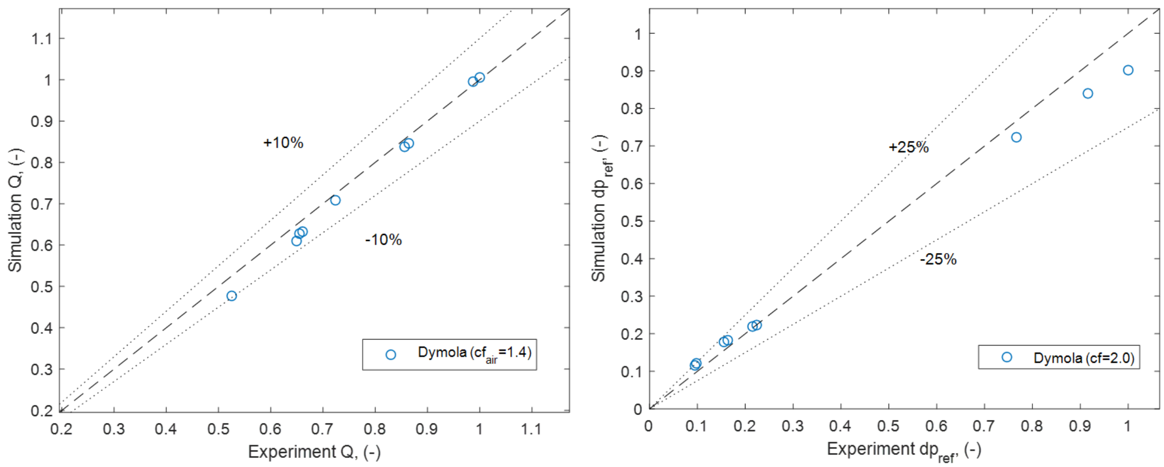

Figure 67: Air condenser validation (non-dimensionalized)

Figure 68 and Figure 69 show the validation of the battery chiller model. A 2.3 correction factor was applied on both sides of the heat exchanger. And the maximum deviation of cooling capacity is 3%. As for the pressure drop, much larger correction factors were applied. These large correction factors are used because the heat exchanger is modeled as smooth plates. However, the actual chiller has enhancement techniques inside the flow channel. So, the high correction factor reflects the increase in heat transfer area and heat transfer coefficient.

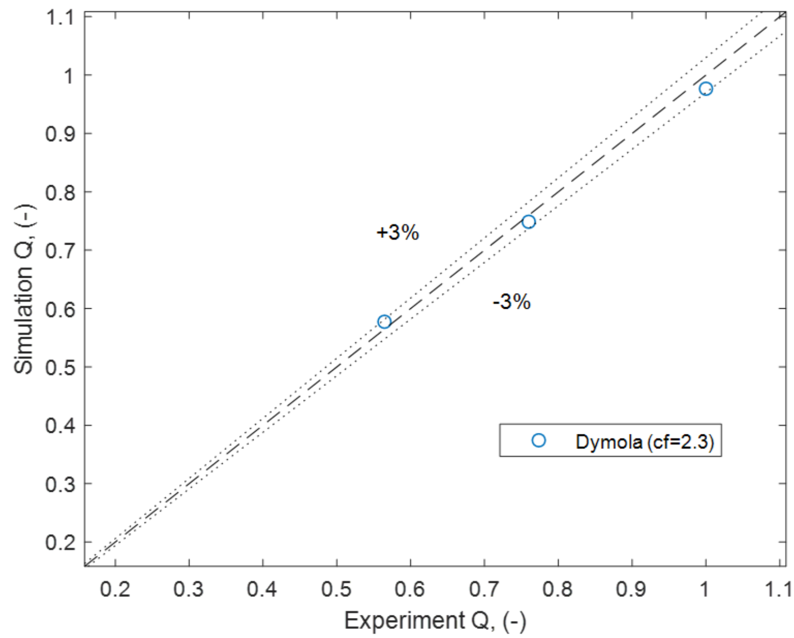

Figure 68: Battery chiller validation - capacity (non-dimensionalized)

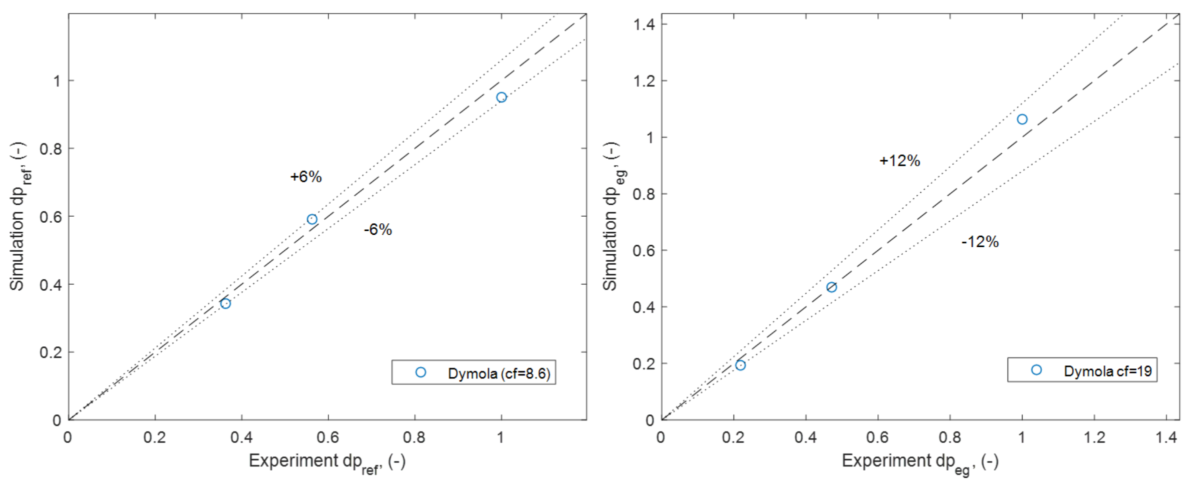

Figure 69: Battery chiller validation – pressure drop (non-dimensionalized)

The water condenser model is similar to the battery chiller model. As shown in Figure 70, a correction factor of 10 is applied on both sides' heat transfer coefficient, bringing the maximum deviation in capacity to 14%. In addition, the correction factor of the refrigerant pressure drop is 27.

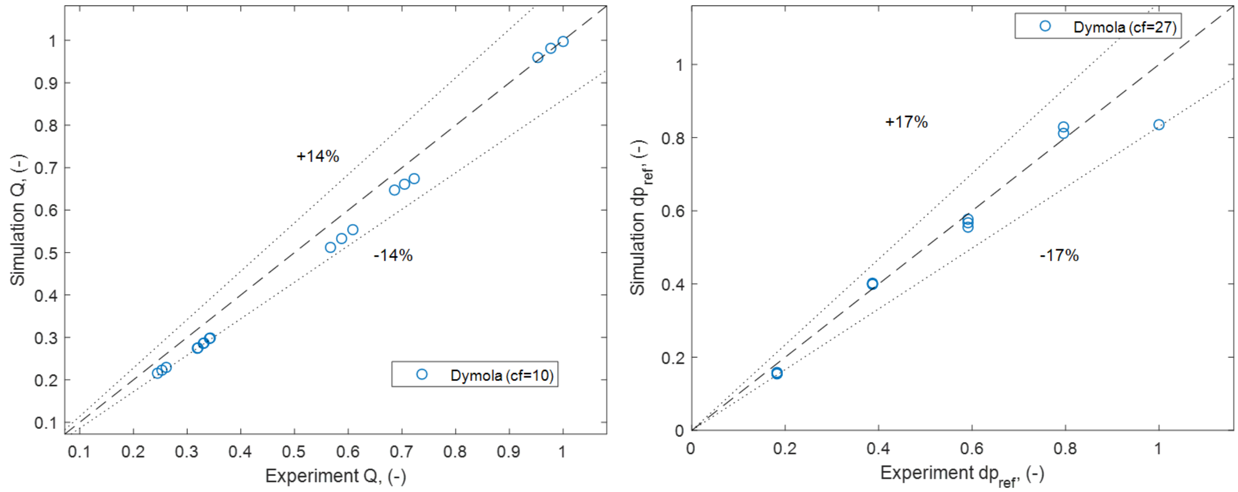

Figure 70: Water condenser validation (non-dimensionalized)

The thermodynamic model mentioned in the previous section was used to generate the design boundary for each heat exchanger. Then, the validated heat exchanger model was used to find the new size that would meet the requirement. Table 32 shows the heat exchanger's size change compared to its original design. Because the target cooling capacity is five times the original value, the battery chiller is increased significantly. On the high-pressure side, radiators remain the same, but the air condenser area is increased a lot to dump the extra heat. The water condenser is also enlarged to deliver heat to the radiators better.

Table 32: Resize heat exchangers

COND	# of tubes of the first pass	+475%
	# of tubes of the second pass	+343%
	# of ports per tube	-67%
	port width	+387%
WCOND H	# of channel	+25%
WCOND L	# of channels for per pass	+171%
Battery chiller	# of channels for per pass	+400%

5.5.2 Results and discussions

Once all the component models were developed and the new heat exchanger models were designed, they were connected to create the detailed cycle models. Like the transient model mentioned in chapter 4, in cycle simulation, simple heat transfer coefficient and pressure drop model were used instead of empirical correlations. In addition, due to the lack of detailed compressor models in Dymola, in this study, the standard efficiency-based compressor model was used. Unlike positive displacement compressors, centrifugal compressor map was usually generated at a fixed suction state. A new map is needed if the suction state changes. This makes it challenging to create a regression model for the centrifugal compressor. This study first solved the cycle model with a fixed compressor efficiency. Then, the boundary conditions of the compressor could be obtained. And they were used to run the 1D compressor model to find the compressor efficiency at that condition. The calculated number was then manually input into the cycle model. This process was repeated multiple times until the compressor efficiency calculated from the 1D model became stable and could match the target pressure ratio.

Table 33 shows the cycle simulation results. The centrifugal compressor was compared to an 80 cc scroll compressor. In the fast-charging mode, when both compressors deliver the same cooling capacity, the centrifugal compressor has a 6.6% higher COP than the scroll compressor. However, in the cabin cooling mode, the scroll compressor has 11.0% higher COP than the centrifugal compressor. And the centrifugal compressor also stalls in the heating mode, while the scroll compressor works without any problem.

Table 33: Cycle simulation results

Mode	Parameter	Centrifugal	80 cc scroll compressor
Fast charging	Cooling capacity (W)	Target + 2.5%	Target + 2%
	COP	1.61 (+6.6%)	1.51
Cabin cooling	Cooling capacity (W)	Target - 2%	Target - 1%
	COP	1.64 (-9.9%)	1.82
Heating	Heating capacity (W)	Stall	33% of the cooling capacity
	COP		2.65

After this calculation, compressor maps can be calculated under three conditions. Figure 71 shows the compressor map at the fast-charging condition. The top figure is the map of the first compression stage. And the bottom figure is the map of the second compression stage. The blue dash line is the compressor stall line. And the component names next to the data point indicates where the compressor is stalled. And the black circle in the map indicates the design point performance. Figure 72 shows the compressor map in the cabin cooling mode. It can be seen that though the compressor still works in this condition, the operating point is very close to the stall limit and can be dangerous to operate. Figure 73 shows the compressor map in the heating mode. The compressor is stalled in the first compression stage. In addition, the overall pressure ratio is way too low for the centrifugal compressor due to the small refrigerant mass flow rate. It is infeasible to run this centrifugal compressor at this condition.

From these results, the centrifugal compressor can have high efficiency at peak load, such as the fasting charging mode. However, its operating range is very limited and may not be a good candidate for future mobile air conditioner systems. The current design can't operate in the heating mode due to a significantly changed suction state. Approaches that can increase the operating range, such as the inlet guide vane or movable vaned diffuser, might help and can be the direction of future research.

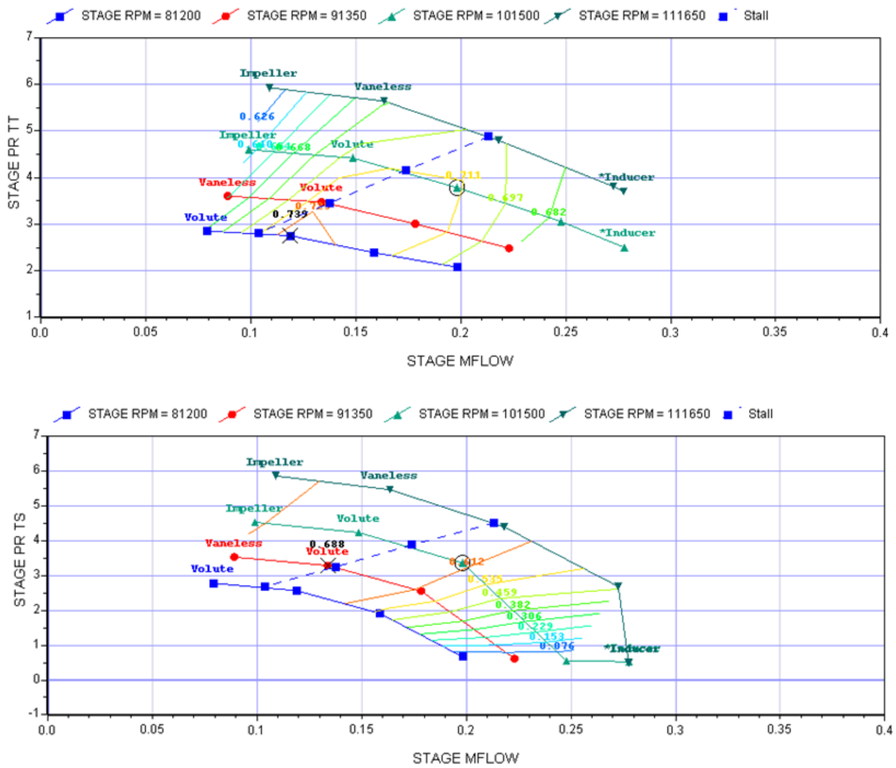

Figure 71: Compressor map (fast charging)

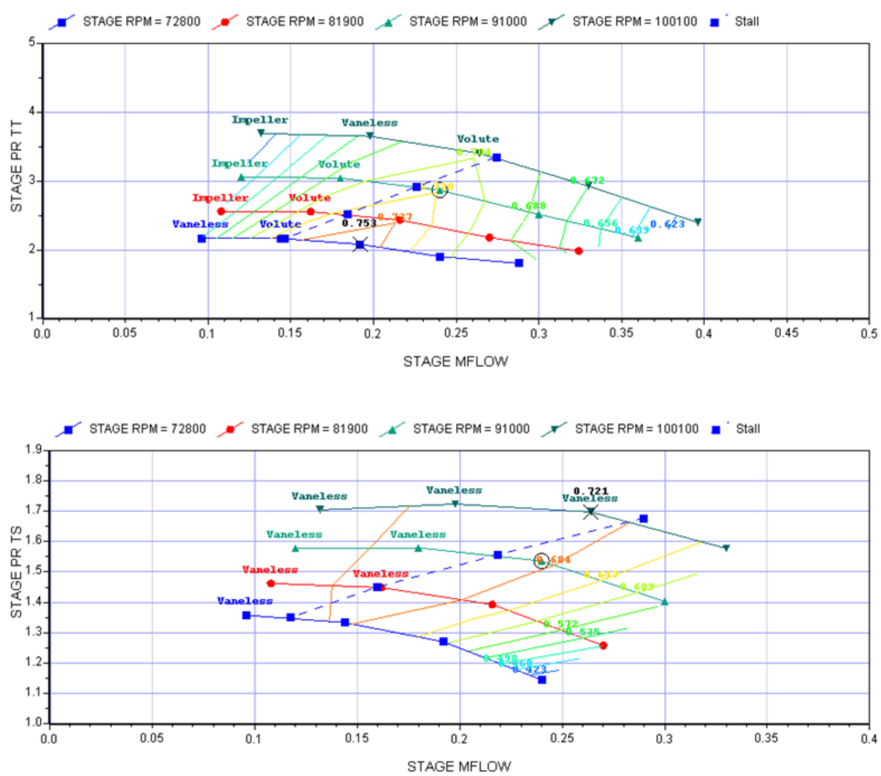

Figure 72: Compressor map (cabin cooling)

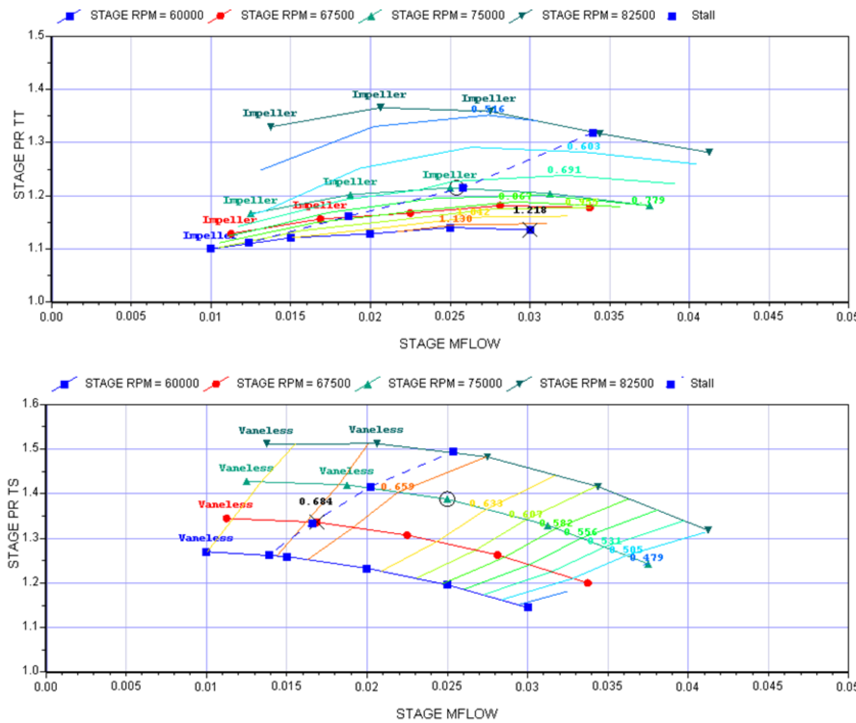

Figure 73: Compressor map (heating)

5.6 Chapter summary and conclusions

In this chapter, an aerodynamic design of a centrifugal compressor was performed. Summaries are as follows:

- Thermodynamic models for three modes: fast charging, cabin cooling, and heating, were developed. In addition, a simple centrifugal compressor model was developed to roughly estimate centrifugal compressor speed and size. The results show that a two-stage centrifugal compressor is more reasonable for the fast charging mode and can deliver higher efficiency.
- 1D optimization was performed to obtain the initial compressor design. The optimum solution has 0.43 PR_{ratio} and 73.3% overall isentropic efficiency.

- 3D design and CFD analysis were performed. The final CFD results show 69.4% first-stage efficiency and 64.7% second-stage efficiency. And the 1D model was adjusted and updated based on the 3D design results.
- Heat exchangers were modeled and resized for the new requirement of the fast charging mode.
- Cycle simulations were performed. Results show that in the fast charging mode, the centrifugal compressor has 1.61 COP, while the COP of the scroll compressor is 1.51. In the cabin cooling mode, the COP of the centrifugal compressor and scroll compressor are 1.64 and 1.82, respectively. As for the heating mode, the centrifugal compressor may stall, while the scroll compressor still works and has a COP of 2.65. These results indicate that though the centrifugal compressor has better efficiency in the fast charging mode, its operating range is minimal, and techniques that can widen its operating range are needed.

6 Conclusions

For fast steady-state analysis, thermodynamic models were developed for BC, FT-VIC, and KC. Since the sub-cycle consumes extra energy to increase the injection mass flow rate, when the compressor speed is the same, KC has a higher heating capacity and lower COP. At T_{amb}=-15°C, compared to FT-VIC, KC, on average, increases heating capacity and decreases COP by 20.1% and 18.9%. To evaluate their performance under various temperature bins, the simulation matrix from SAE standard J2765 was expanded to cover heating mode. And calculations were performed to calculate their annual energy consumption. Results show that FT-VIC has a higher COP than BC. And KC has the higher heating capacity and $COP_{overall}$ (including PTC heater) only when T_{amb}=-15°C. In other simulations, the increased power consumption of the sub-cycle compressor is higher than the reduced power consumption of the main-cycle compressor. In addition to the annual energy consumption, LCCP was also evaluated. Results show that the annual energy consumption of M3 is on average 1.3% higher than that of M1 and 3.0% higher than that of M2. And LCCP of M3 is on average 3.0% higher than that of M1 and 4.6% higher than that of M2.

Since vehicles are moving at various speeds, a transient model is necessary to evaluate real-time cycles' performance. Thus, Dymola models were developed for BC, FT-VIC, and KC. A modified fan model with ram air compensation was developed to estimate the outdoor air velocity. Transient simulation at -15°C under the UDDS driving cycle was performed. Results show the heating capacity is stable despite the highly fluctuating vehicle speed. And at the end of the simulation, the accumulated heating capacity of KC is 14.8% higher than VIC and 32.7% higher than BC. However, the accumulated power consumption of KC is 32.4% higher than VIC and 64.4% higher than BC.

In addition, a centrifugal compressor was designed for a future EV with high fast-charging cooling demand. The results show that at the design point (fast charging mode), the centrifugal compressor's COP is 1.61, which is 6.6% higher than the scroll compressor. However, at the off-design point, its performance is worse. In the cabin cooling mode, its COP is 1.64, while the COP of the scroll compressor is 1.82. And the centrifugal compressor cannot operate in heat pump mode. To resolve this issue, efforts should be made on things that could expand its operating range, such as the inlet guide vane.

Contributions made in this research are:

- Thermodynamic analysis and LCCP evaluation of advanced heat pump cycles for EV:
    - Built the KC thermodynamic model for quick cycle performance analysis. Calculated and compared heat pump cycles' performance under various conditions.
    - Proposed a new method for evaluating electric vehicle heat pumps' LCCP. Calculated and compared their LCCP across the U.S.
- Transient modeling of advanced heat pump cycles for EV:
    - Built the transient model for KC.
    - Added ram air compensation to the air maldistribution calculation.
    - Performed steady-state and transient calculations and compared cycle performance.
- Centrifugal compressor design and performance evaluation for future MACs with high cooling demand:
    - Designed a two-stage centrifugal compressor for the fast charging mode with high cooling demand.
    - Simulated the centrifugal compressor's cycle performance.

Bibliography

[1] Global EV Outlook 2020 2020:276.
[2] Yang Z, Wang B, Jiao K. Life cycle assessment of fuel cell, electric and internal combustion engine vehicles under different fuel scenarios and driving mileages in China. Energy 2020;198:117365. https://doi.org/10.1016/j.energy.2020.117365.
[3] Umezu K, Noyama H. Air-Conditioning system For Electric Vehicles (i-MiEV) n.d.
[4] Li W, Liu Y, Liu R, Wang D, Shi J, Yu Z, et al. Performance evaluation of secondary loop low-temperature heat pump system for frost prevention in electric vehicles. Applied Thermal Engineering 2021;182:115615. https://doi.org/10.1016/j.applthermaleng.2020.115615.
[5] Ahn JH, Kang H, Lee HS, Jung HW, Baek C, Kim Y. Heating performance characteristics of a dual source heat pump using air and waste heat in electric vehicles. Applied Energy 2014;119:1–9. https://doi.org/10.1016/j.apenergy.2013.12.065.
[6] Liu C, Zhang Y, Gao T, Shi J, Chen J, Wang T, et al. Performance evaluation of propane heat pump system for electric vehicle in cold climate. International Journal of Refrigeration 2018;95:51–60. https://doi.org/10.1016/j.ijrefrig.2018.08.020.
[7] Li W, Liu R, Liu Q, Liu Y, Wang D, Xia S, et al. Upstream and downstream injection effects on R134a economized vapor injection heat pump system at low temperatures for electric vehicles. International Journal of Refrigeration 2020;120:1–11. https://doi.org/10.1016/j.ijrefrig.2020.04.003.
[8] Zhang Z, Wang J, Feng X, Chang L, Chen Y, Wang X. The solutions to electric vehicle air conditioning systems: A review. Renewable and Sustainable Energy Reviews 2018;91:443–63. https://doi.org/10.1016/j.rser.2018.04.005.
[9] Qin F, Shao S, Tian C, Yang H. Experimental Investigation on Heating Performance of Heat Pump for Electric Vehicles in Low Ambient Temperature. Energy Procedia 2014;61:726–9. https://doi.org/10.1016/j.egypro.2014.11.952.
[10] Jung J, Jeon Y, Lee H, Kim Y. Numerical study of the effects of injection-port design on the heating performance of an R134a heat pump with vapor injection used in electric vehicles. Applied Thermal Engineering 2017;127:800–11. https://doi.org/10.1016/j.applthermaleng.2017.08.098.
[11] Qin F, Xue Q, Zhang G, Zou H, Tian C. Experimental Investigation on Heat Pump for Electric Vehicles with different Refrigerant Injection Compressors. Energy Procedia 2015;75:1490–5. https://doi.org/10.1016/j.egypro.2015.07.281.
[12] Okuma T, Radermacher R, Hwang Y. A Novel Application of Thermoelectric Modules in an HVAC System Under Cold Climate Operation. Journal of Elec Materi 2012;41:1749–58. https://doi.org/10.1007/s11664-012-2066-x.
[13] Ghodbane M. An Investigation of R152a and Hydrocarbon Refrigerants in Mobile Air Conditioning. SAE Transactions 1999;108:1658–73.
[14] Lee H, Troch S, Hwang Y, Radermacher R. LCCP evaluation on various vapor compression cycle options and low GWP refrigerants. International Journal of Refrigeration 2016;70:128–37. https://doi.org/10.1016/j.ijrefrig.2016.07.003.
[15] Troch S. HARMONIZATION OF LIFE CYCLE CLIMATE PERFORMANCE AND ITS IMPROVEMENT FOR HEAT PUMP APPLICATIONS. 2016.

[16] SAE International. Life Cycle Analysis to Estimate the CO2-Equivalent Emissions from MAC Operation. SAE Standard J2766. SAE International; 2019. https://doi.org/10.4271/J2766_201908.
[17] Papasavva S, Hill WR, Andersen SO. GREEN-MAC-LCCP: A Tool for Assessing the Life Cycle Climate Performance of MAC Systems. Environmental Science & Technology 2010;44:7666–72. https://doi.org/10.1021/es100849g.
[18] Papasavva S, Luecken DJ, Waterland RL, Taddonio KN, Andersen SO. Estimated 2017 Refrigerant Emissions of 2,3,3,3-tetrafluoropropene (HFC-1234yf) in the United States Resulting from Automobile Air Conditioning. Environmental Science & Technology 2009;43:9252–9. https://doi.org/10.1021/es902124u.
[19] SAE International. Procedure for Measuring System COP [Coefficient of Performance] of a Mobile Air Conditioning System on a Test Bench. SAE Standard J2765. SAE International; 2017. https://doi.org/10.4271/J2765_201707.
[20] US EPA O. Dynamometer Drive Schedules. US EPA 2015. https://www.epa.gov/vehicle-and-fuel-emissions-testing/dynamometer-drive-schedules (accessed July 11, 2017).
[21] Rhoads A, Hill W. Development of a Tool for Estimating the Life Cycle Climate Performance of MAC Systems, 2019, p. 2019-01–0611. https://doi.org/10.4271/2019-01-0611.
[22] Zhang Z, Chen X, Liu C, Li W, Shi J, Chen J. LCCP Analysis of Energy-Saving Effect of Defaulting to Recirculated Cabin Air in EV Mobile Air Conditioning System, West Lafayette: 2016.
[23] Arpagaus C, Bless F, Bertsch S, Javed A, Schiffmann JA. Heat Pump driven by a Small-Scale Oil-Free Turbocompressor–System Design and Simulation. 12th IEA Heat Pump Conference 2017, 2017.
[24] Casey MV, Krähenbuhl D, Zwyssig C. The Design of Ultra-High-Speed Miniature Centrifugal Compressors. European Conference on Turbomachinery Fluid Dynamics and Thermodynamics ETC, vol. 10, 2013, p. 1–13.
[25] Schiffmann J, Favrat D. Experimental investigation of a direct driven radial compressor for domestic heat pumps. International Journal of Refrigeration 2009;32:1918–28. https://doi.org/10.1016/j.ijrefrig.2009.07.006.
[26] Brondum DC, Materne JE, Biancardi FR, Pandy DR. High-speed, direct-drive centrifugal compressors for commercial HVAC systems, 1998.
[27] Schiffmann J, Favrat D. Design, experimental investigation and multi-objective optimization of a small-scale radial compressor for heat pump applications. Energy 2010;35:436–50. https://doi.org/10.1016/j.energy.2009.10.010.
[28] Schiffmann J. Integrated design and multi-objective optimization of a single stage heat-pump turbocompressor. Journal of Turbomachinery 2015;137:071002.
[29] Schiffmanna J, Carréa JB, Arpagausb C, Bertschb S. Turbocompressors for Domestic Heat Pumps–A Critical Review. 12th IEA Heat Pump Conference 2017, 2017.
[30] Carré J-B, Favrat D, Schiffmann J. Experimental investigation of a two-stage oil-free domestic Air/Water heat pump prototype powered by an oil-free high-speed twin-stage radial compressor rotating on gas bearings 2016.
[31] Javed A, Arpagaus C, Bertsch S, Schiffmann J. Small-scale turbocompressors for wide-range operation with large tip-clearances for a two-stage heat pump concept. International Journal of Refrigeration 2016;69:285–302. https://doi.org/10.1016/j.ijrefrig.2016.06.015.
[32] H. J. Van Gerner, G. Van Donk. A Heat Pump for Space Applications 2015.

[33] Laveau A, Kapat JS, Chow LC, Enikov E, Sundaram KB. Design analysis and fabrication of a meso-scale centrifugal compressor. ASME Advanced Energy System s D Ivision 2000;40:1292137.
[34] Schiffmann J. Enhanced groove geometry for herringbone grooved journal bearings. Journal of Engineering for Gas Turbines and Power 2013;135:102501.
[35] Xu S, Niu J, Ma G. Experimental study on R1234Yf heat pump at low ambient temperature and comparison with other refrigerants. Thermal Science 2018;2018:201–201. https://doi.org/10.2298/TSCI171019201X.
[36] Ma G, Li X. Exergetic optimization of a key design parameter in heat pump systems with economizer coupled with scroll compressor. Energy Conversion and Management 2007;48:1150–9. https://doi.org/10.1016/j.enconman.2006.10.007.
[37] Jain S, Bullard CW. Capacity and Efficiency in Variable Speed, Vapor Injection and Multi-Compressor Systems n.d.:51.
[38] Mei Z, Hwang Y, Kim J. Thermodynamic analysis and LCCP evaluation of kangaroo heat pump cycle for electric vehicles. Energy 2022;259:124995. https://doi.org/10.1016/j.energy.2022.124995.
[39] Jiang H. Development of a Simulation and Optimization Tool for Heat Exchanger Design. University of Maryland, College Park, 2003.
[40] EES: Engineering Equation Solver | F-Chart Software : Engineering Software n.d. http://fchartsoftware.com/ees/ (accessed February 17, 2021).
[41] Yunho Hwang. Comprehensive investigation of carbon dioxide refrigeration cycle. Ph.D. University of Maryland, College Park, 1997.
[42] Standard A. Performance Rating Of Positive Displacement Refrigerant Compressors and Compressor Units 2004.
[43] Dabiri AE, Rice CK. Compressor-simulation model with corrections for the level of suction gas superheat, 1981.
[44] Tello-Oquendo FM, Navarro-Peris E, Gonzálvez-Maciá J. New characterization methodology for vapor-injection scroll compressors. International Journal of Refrigeration 2017;74:528–39. https://doi.org/10.1016/j.ijrefrig.2016.11.019.
[45] Erickson LJ. Rating Equations for Positive Displacement Compressors with Auxiliary Suction Ports n.d.:6.
[46] Cambio, M. Representation of a Positive Displacement Compressor Map with Vapor Injection n.d.
[47] Sjoholm L, Ma YC. A Study of Low GWP Refrigerants for Transport Refrigeration based on Hermetic Scroll Compressors with an Economizer n.d.:10.
[48] Lumpkin D, Spielbauer N, Groll E. Performance Measurements and Mapping of a R-407C Vapor Injection Scroll Compressor. IOP Conf Ser: Mater Sci Eng 2017;232:012049. https://doi.org/10.1088/1757-899X/232/1/012049.
[49] Winandy EL, Lebrun J. Scroll compressors using gas and liquid injection: experimental analysis and modelling. International Journal of Refrigeration 2002;25:1143–56. https://doi.org/10.1016/S0140-7007(02)00003-8.
[50] Dardenne L, Fraccari E, Maggioni A, Molinaroli L, Proserpio L, Winandy E. Semi-empirical modelling of a variable speed scroll compressor with vapour injection. International Journal of Refrigeration 2015;54:76–87. https://doi.org/10.1016/j.ijrefrig.2015.03.004.

[51] Qiao H, Aute V, Radermacher R. Transient modeling of a flash tank vapor injection heat pump system – Part I: Model development. International Journal of Refrigeration 2015;49:169–82. https://doi.org/10.1016/j.ijrefrig.2014.06.019.
[52] Wang X. PERFORMANCE INVESTIGATION OF TWO- STAGE HEAT PUMP SYSTEM WITH VAPOR- INJECTED SCROLL COMPRESSOR. n.d.
[53] Xu X. INVESTIGATION OF VAPOR INJECTION HEAT PUMP SYSTEM WITH A FLASH TANK UTILIZING R410A AND LOW-GWP REFRIGERANT R32. n.d.
[54] Dechesne B, Bertagnolio S, Lemort V. Development of an empirical model of a variable speed vapor injection compressor used in a Modelica-based dynamic model of a residential air source heat pump. IOP Conf Ser: Mater Sci Eng 2015;90:012031. https://doi.org/10.1088/1757-899X/90/1/012031.
[55] US EPA O. Refrigerant Transition & Environmental Impacts. US EPA 2015. https://www.epa.gov/mvac/refrigerant-transition-environmental-impacts (accessed February 14, 2021).
[56] Wilcox S, Marion W. Users Manual for TMY3 Data Sets 2008.
[57] Johnson VH. Fuel Used for Vehicle Air Conditioning: A State-by-State Thermal Comfort-Based Approach. Warrendale, PA: SAE International; 2002. https://doi.org/10.4271/2002-01-1957.
[58] American Society of Heating, Refrigerating and Air-Conditioning Engineers. 2017 ASHRAE handbook: Fundamentals : SI edition. Atlanta, GA: ASHRAE, 2017, ©2017; 2017.
[59] Fanger PO. Thermal comfort. Analysis and applications in environmental engineering. New York: McGraw-Hill; 1970.
[60] Buck. Buck Research CR-1A User's Manual, Appendix 1 1996.
[61] Weiss M, Cloos KC, Helmers E. Energy efficiency trade-offs in small to large electric vehicles. Environmental Sciences Europe 2020;32:46. https://doi.org/10.1186/s12302-020-00307-8.
[62] Frequently Asked Questions (FAQs) - U.S. Energy Information Administration (EIA) n.d. https://www.eia.gov/tools/faqs/faq.php (accessed February 3, 2021).
[63] Valøen LO, Shoesmith MI. The effect of PHEV and HEV duty cycles on battery and battery pack performance. PHEV 2007 Conference, 2007, p. 4–5.
[64] Apostolaki-Iosifidou E, Codani P, Kempton W. Measurement of power loss during electric vehicle charging and discharging. Energy 2017;127:730–42. https://doi.org/10.1016/j.energy.2017.03.015.
[65] Emission Factors for Greenhouse Gas Inventories. U.S. EPA; 2020.
[66] Pachauri RK, Mayer L, Intergovernmental Panel on Climate Change, editors. Climate change 2014: synthesis report. Geneva, Switzerland: Intergovernmental Panel on Climate Change; 2015.
[67] Qiao H. Transient modeling of two-stage and variable refrigerant flow vapor compression systems with frosting and defrosting. PhD Dissertation. University of Maryland, College Park, 2014.
[68] Eisele M. Transient performance evaluation of automotive secondary loop systems. PhD Dissertation. University of Maryland, College Park, 2012.
[69] Lee H, Hwang Y, Song I, Jang K. Transient thermal model of passenger car's cabin and implementation to saturation cycle with alternative working fluids. Energy 2015;90:1859–68. https://doi.org/10.1016/j.energy.2015.07.016.

[70] Huang C-CD. A dynamic computer simulation model for automobile passenger compartment climate control and evaluation. PhD Dissertation. Michigan Technological University, 1998.
[71] Shah RK, Sekulić DP. Fundamentals of heat exchanger design. Hoboken, NJ: John Wiley & Sons; 2003.
[72] Chang Y-J, Wang C-C. A generalized heat transfer correlation for louver fin geometry. Int J Heat Mass Transfer 1997;40:533–44.
[73] Qiao H, Aute V, Radermacher R. Dynamic modeling and characteristic analysis of a two-stage vapor injection heat pump system under frosting conditions. International Journal of Refrigeration 2017;84:181–97. https://doi.org/10.1016/j.ijrefrig.2017.08.020.
[74] Brèque F, Nemer M. Frosting modeling on a cold flat plate: Comparison of the different assumptions and impacts on frost growth predictions. International Journal of Refrigeration 2016;69:340–60. https://doi.org/10.1016/j.ijrefrig.2016.06.010.
[75] Brian PLT, Reid RC, Shah YT. Frost Deposition on Cold Surfaces. Ind Eng Chem Fund 1970;9:375–80. https://doi.org/10.1021/i160035a013.
[76] Lee K-S, Kim W-S, Lee T-H. A one-dimensional model for frost formation on a cold flat surface. International Journal of Heat and Mass Transfer 1997;40:4359–65. https://doi.org/10.1016/S0017-9310(97)00074-4.
[77] Breque F, Nemer M. Modeling of a fan-supplied flat-tube heat exchanger exposed to non-uniform frost growth. International Journal of Refrigeration 2017;75:129–40. https://doi.org/10.1016/j.ijrefrig.2016.12.012.
[78] Shah MM. A correlation for heat transfer during condensation in horizontal mini/micro channels. International Journal of Refrigeration 2016;64:187–202. https://doi.org/10.1016/j.ijrefrig.2015.12.008.
[79] Brushed Axial Fans - SPAL n.d. https://www.spalautomotive.it/axial-fans/VA10-AP70/LL-61S/32179 (accessed February 17, 2023).
[80] Ap N-S, Guerrero P, Jouanny P. Influence of Fan System Electric Power on the Heat Performance of Engine Cooling Module. Warrendale, PA: SAE International; 2003. https://doi.org/10.4271/2003-01-0275.
[81] Kim M-H, Bullard CW. Air-side thermal hydraulic performance of multi-louvered fin aluminum heat exchangers. International Journal of Refrigeration 2002;25:390–400. https://doi.org/10.1016/S0140-7007(01)00025-1.
[82] Li L, Gohl J, Batteh J, Greiner C, Wang K. Fast Calculation of Refrigerant Properties in Vapor Compression Cycles Using Spline-Based Table Look-Up Method (SBTL), 2019, p. 77–84. https://doi.org/10.3384/ecp1815477.
[83] XProps® n.d. https://www.optimizedthermalsystems.com/index.php/products/xprops (accessed March 13, 2023).
[84] Lemmon E. NIST Reference Fluid Thermodynamic and Transport Properties Database: Version 9.0, NIST Standard Reference Database 23 1989. https://doi.org/10.18434/T4JS3C.
[85] Y.Y. Yan, T.F. Lin. Evaporation heat transfer and pressure drop of refrigerant r-134a in a plate heat exchanger. Journal of Heat Transfer 1999;121:118–27.
[86] Kim I-K, Park J-H, Kwon Y-H, Kim Y-S. Experimental Study on R-410a Evaporation Heat Transfer Characteristics in Oblong Shell and Plate Heat Exchanger. Heat Transfer Engineering 2007;28:633–9. https://doi.org/10.1080/01457630701266454.

[87] Muley A, Manglik RM. Experimental study of turbulent flow heat transfer and pressure drop in a plate heat exchanger with chevron plates 1999.
[88] Khan M, Chyu M. Evaporation in Flooded Corrugated Plate Heat Exchangers with Ammonia and Ammonia/Miscible Oil, RP-1352. American Society of Heating, Refrigerating and Air-Conditioning Engineers, Inc, Atlanta, GA, USA 2010.
[89] Yi-Yie Yan, Hsiang-Chao Lio, Tsing-Fa Li. Condensation heat transfer and pressure drop of refrigerantR134aa in a plate heat exchanger.pdf. International Journal of Heat and Mass Transfer 1998;42:993–1006.
[90] Lockhart RW, Martinelli RC. Proposed correlation of data for isothermal two-phase, two-component flow in pipes. Chem Eng Prog 1949;45:39–48.
[91] Balje OE. Turbomachines-A guide to design, selection, and theory. John Wiley & Sons; 1981.
[92] NREC C. Computer Aided Engineering | Software Solutions n.d. https://www.conceptsnrec.com/solutions/software/computer-aided-engineering (accessed July 16, 2019).
[93] Japikse D, Baines NC. Introduction to Turbomachinery. Oxford: Oxford University Press; 1994.
[94] pymoo n.d. http://pymoo.org/algorithms/genetic_algorithm.html (accessed October 9, 2019).
[95] Deb K, Kalyanmoy D. Multi-Objective Optimization Using Evolutionary Algorithms. New York, NY, USA: John Wiley & Sons, Inc.; 2001.
[96] Ansys BladeModeler | 3D Blade Design Software n.d. https://www.ansys.com/products/fluids/ansys-blademodeler (accessed March 8, 2023).
[97] Ansys TurboGrid | Turbine Blade Meshing Software n.d. https://www.ansys.com/products/fluids/ansys-turbogrid (accessed March 8, 2023).
[98] Ansys CFX | Industry-Leading CFD Software n.d. https://www.ansys.com/products/fluids/ansys-cfx (accessed March 8, 2023).
[99] Bergman TL, Incropera FP, editors. Fundamentals of heat and mass transfer. 7th ed. Hoboken, NJ: Wiley; 2011.
[100] Winterton RHS. Where did the Dittus and Boelter equation come from? International Journal of Heat and Mass Transfer 1998;41:809–10. https://doi.org/10.1016/S0017-9310(97)00177-4.
[101] Shah MM. A general correlation for heat transfer during film condensation inside pipes. International Journal of Heat and Mass Transfer 1979;22:547–56.
[102] Ould Didi MB, Kattan N, Thome JR. Prediction of two-phase pressure gradients of refrigerants in horizontal tubes. International Journal of Refrigeration 2002;25:935–47. https://doi.org/10.1016/S0140-7007(01)00099-8.
[103] Kandlikar SG. A General Correlation for Saturated Two-Phase Flow Boiling Heat Transfer Inside Horizontal and Vertical Tubes. Journal of Heat Transfer 1990;112:219–28. https://doi.org/10.1115/1.2910348.
[104] Jung D-S, McLinden M, Radermacher R, Didion D. A study of flow boiling heat transfer with refrigerant mixtures. International Journal of Heat and Mass Transfer 1989;32:1751–64.